

NASA/CR-2015-218691



Multiscale and Multiphysics Modeling of Additive Manufacturing of Advanced Materials

Frank Liou, Joseph Newkirk, Zhiqiang Fan, Todd Sparks, Xueyang Chen, Kenneth Fletcher, Jingwei Zhang, Yunlu Zhang, Kannan Suresh Kumar, and Sreekar Karnati
Missouri University of Science and Technology, Rolla, Missouri

February 2015

NASA STI Program . . . in Profile

Since its founding, NASA has been dedicated to the advancement of aeronautics and space science. The NASA scientific and technical information (STI) program plays a key part in helping NASA maintain this important role.

The NASA STI program operates under the auspices of the Agency Chief Information Officer. It collects, organizes, provides for archiving, and disseminates NASA's STI. The NASA STI program provides access to the NTRS Registered and its public interface, the NASA Technical Reports Server, thus providing one of the largest collections of aeronautical and space science STI in the world. Results are published in both non-NASA channels and by NASA in the NASA STI Report Series, which includes the following report types:

- **TECHNICAL PUBLICATION.** Reports of completed research or a major significant phase of research that present the results of NASA Programs and include extensive data or theoretical analysis. Includes compilations of significant scientific and technical data and information deemed to be of continuing reference value. NASA counter-part of peer-reviewed formal professional papers but has less stringent limitations on manuscript length and extent of graphic presentations.
- **TECHNICAL MEMORANDUM.** Scientific and technical findings that are preliminary or of specialized interest, e.g., quick release reports, working papers, and bibliographies that contain minimal annotation. Does not contain extensive analysis.
- **CONTRACTOR REPORT.** Scientific and technical findings by NASA-sponsored contractors and grantees.

- **CONFERENCE PUBLICATION.** Collected papers from scientific and technical conferences, symposia, seminars, or other meetings sponsored or co-sponsored by NASA.
- **SPECIAL PUBLICATION.** Scientific, technical, or historical information from NASA programs, projects, and missions, often concerned with subjects having substantial public interest.
- **TECHNICAL TRANSLATION.** English-language translations of foreign scientific and technical material pertinent to NASA's mission.

Specialized services also include organizing and publishing research results, distributing specialized research announcements and feeds, providing information desk and personal search support, and enabling data exchange services.

For more information about the NASA STI program, see the following:

- Access the NASA STI program home page at <http://www.sti.nasa.gov>
- E-mail your question to help@sti.nasa.gov
- Phone the NASA STI Information Desk at 757-864-9658
- Write to:
NASA STI Information Desk
Mail Stop 148
NASA Langley Research Center
Hampton, VA 23681-2199

NASA/CR-2015-218691



Multiscale and Multiphysics Modeling of Additive Manufacturing of Advanced Materials

*Frank Liou, Joseph Newkirk, Zhiqiang Fan, Todd Sparks, Xueyang Chen, Kenneth Fletcher,
Jingwei Zhang, Yunlu Zhang, Kannan Suresh Kumar, and Sreekar Karnati
Missouri University of Science and Technology, Rolla, Missouri*

National Aeronautics and
Space Administration

Langley Research Center
Hampton, Virginia 23681-2199

Prepared for Langley Research Center
under Cooperative Agreement NNX11AI73A

February 2015

Available from:

NASA STI Program / Mail Stop 148
NASA Langley Research Center
Hampton, VA 23681-2199
Fax: 757-864-6500

ABSTRACT

The objective of this proposed project is to research and develop a prediction tool for advanced additive manufacturing (AAM) processes for advanced materials and develop experimental methods to provide fundamental properties and establish validation data. Aircraft structures and engines demand materials that are stronger, useable at much higher temperatures, provide less acoustic transmission, and enable more aeroelastic tailoring than those currently used. Significant improvements in properties can only be achieved by processing the materials under non-equilibrium conditions, such as AAM processes. AAM processes encompass a class of processes that use a focused heat source to create a melt pool on a substrate. Examples include Electron Beam Freeform Fabrication and Direct Metal Deposition. These types of additive processes enable fabrication of parts directly from CAD drawings.

To achieve the desired material properties and geometries of the final structure, assessing the impact of process parameters and predicting optimized conditions with numerical modeling as an effective prediction tool is necessary. The targets for the processing are multiple and at different spatial scales, and the physical phenomena associated occur in multiphysics and multiscale.

In this project, the research work has been developed to model AAM processes in a multiscale and multiphysics approach. A macroscale model was developed to investigate the residual stresses and distortion in AAM processes. A sequentially coupled, thermomechanical, finite element model was developed and validated experimentally. The results showed the temperature distribution, residual stress, and deformation within the formed deposits and substrates.

A mesoscale model was developed to include heat transfer, phase change with mushy zone, incompressible free surface flow, solute redistribution, and surface tension. Because of excessive computing time needed, a parallel computing approach was also tested. In addition, after investigating various methods, a Smoothed Particle Hydrodynamics Model (SPH Model) was developed to model wire feeding process. Its computational efficiency and simple architecture makes it more robust and flexible than other models. More research on material properties may be needed to realistically model the AAM processes.

A microscale model was developed to investigate heterogeneous nucleation, dendritic grain growth, epitaxial growth of columnar grains, columnar-to-equiaxed transition, grain transport in melt, and other properties. The orientations of the columnar grains were almost perpendicular to the laser motion's direction. Compared to the similar studies in the literature, the multiple grain morphology modeling result is in the same order of magnitude as optical morphologies in the experiment.

Experimental work was conducted to validate different models. An infrared camera was incorporated as a process monitoring and validating tool to identify the solidus and mushy zones during deposition. The images were successfully processed to identify these regions. This research project has investigated multiscale and multiphysics of the complex AAM processes thus leading to advanced understanding of these processes. The project has also developed several modeling tools and experimental validation tools that will be very critical in the future of AAM process qualification and certification.

Table of Contents

1.	Introduction.....	4
2.	Thermo-Fluid Model.....	6
3.	Wire Model Introduction	10
	3.1. Introduction	10
	3.2. Analysis.....	11
	3.3. Future Work	16
4.	Parallel Computing	17
5.	Smoothed Particle Hydrodynamics Model	24
	5.1. Abstract	24
	5.2. Theory	24
	5.3. Comparison with VOF Technique	26
	5.4. Program Flow	28
6.	SPH Model Implementation	29
	6.1. Initialization.....	29
	6.2. Creating Solids and Applying Material Properties.....	30
	6.3. Iterative Calculations.....	30
	6.3.1. Laser Projection.....	31
	6.3.2. Heat Conduction	31
	6.3.3. Radiation Losses.....	31
	6.3.4. Temperature Calculation	31
	6.3.5. Phase-change Calculation.....	31
	6.3.6. Updating Smoothing Length	32
	6.3.7. Calculating Fluid Forces.....	32
	6.3.8. Solid-Fluid Interaction Calculation	33
	6.3.9. Movement.....	33
	6.3.10. Increment Time and Save Data	34
	6.4. Results	34
	6.4.1. Temperature Plots Using Matplot.....	37
	6.4.2. Phase Plots Using Mayavi	38
	6.5. Conclusion.....	39
7.	Numerical Analysis of Thermal Stress and Deformation in Multilayer Laser Metal Deposition Processes	40
	7.1. Introduction	40
	7.2. Thermal Analysis	40
	7.2.1. Initial and Boundary Conditions and Energy Distribution.....	40
	7.2.2. Powder Addition.....	41
	7.2.3. FEA Model	41
	7.2.4. Numerical Temperature Field.....	42
	7.3. Residual Stress	44
	7.4. Deformation.....	48
	7.4.1. Experimental Setup.....	48
	7.5. Conclusion.....	50
8.	Solidification Microstructure	51
	8.1. Cellular Automaton (CA) - Finite Element (FE) Model Introduction	51

8.2.	Thermal History and Grain Morphology Model Result During Laser Remelting Process.....	53
8.3.	Solidification Grain Morphology Modeling Under Laser Deposition.....	54
8.4.	Comparison with Experimental Results in the Related Literature	59
8.5.	Summary	59
9.	Microstructure Observation and Simulation of Ti6Al4V Single-Wall Deposition ..	61
9.1.	Introduction	61
9.2.	Experiment	62
9.3.	Simulation	63
9.4.	Result and Analysis	63
9.5.	Conclusion.....	67
10.	Incorporation of Infrared Camera to Monitor Laser Metal Deposition Process.	68
10.1.	Introduction	68
10.2.	Setup and Calibration	69
10.3.	Experimentation and Results.....	69
10.3.1.	Energy Management System.....	69
10.3.2.	High-Temperature Region.....	71
10.3.3.	Deposition Visualization	71
10.4.	Image Processing.....	73
10.4.1.	Laplace Edge Detection.....	73
10.4.2.	Methodology.....	74
10.5.	Conclusions	75
10.6.	Future Work	75
11.	Related Works.....	76
11.1.	Related Publications:.....	76
11.2.	Related Presentations:	76
11.3.	To Be Published/Presented:.....	77
11.4.	Related Theses and Dissertations:.....	77
11.5.	News Articles:	77
12.	References.....	78

1. Introduction

Table 1.1 lists the tasks completed for the entire project. In the main body, chapter 2 describes the three-dimensional model used to simulate the thermal and velocity field of the laser deposited melt pool. Chapter 3 introduces the idea for the wire model, which solves the solid-liquid interaction and shows preliminary simulation results for the wire and molten pool. Chapter 4 describes the use of parallel computing in order to optimize the thermofluid simulation previously mentioned in chapter 2. Chapters 5 and 6 introduce the Smoothed Particle Hydrodynamics Model (SPH Model), a comparison with the Volume of Fluid (VOF) technique, and the SPH Model implementation. Chapter 7 describes the numerical analysis of thermal stress and deformation in multilayer Laser Metal Deposition Processes (LMDP) and the experimental validation. Chapter 8 covers the Finite Element-Cellular Automaton (FE-CA) model and predicts equiaxed and columnar grain growth based on the thermal history obtained with the computations described in Chapter 7. The grain growth prediction was validated by comparing similar experimental results from the literature. Chapter 9 introduces the microstructural observation and simulation of Ti6Al4V single-wall deposition. Chapter 10 is about the use of an infrared camera to monitor the laser metal deposition process and the concomitant image processing.

Table 1.1 Tasks of the project

Task 1. macroscopic model	
Task 1a. Thermal/fluid dynamics	Code completed/Python version developed to improve code efficiency and numerical convergence issues
Task 1b. Residual stress model	Completed using Abaqus commercial software
Task 2. Microscopic model	
Task 2a. As-received microstructure	Completed using open source MMSP code
Task 2b. Solidification microstructure	2D code completed. Columnar model completed; 3D model is in progress.
Task 2c. Solid-state phase transformations	Being implemented
Task 3. Data collection and model validation	
Task 3a. Temperature measurement	Technique developed (IR camera) and thermal couple to be used for validation
Task 3b. Clad and melt pool geometry measurement	Technique developed; used for validation
Task 3c. Residual stress measurement	Completed using a simple example to demonstrate
Task 3d. Validation of microstructures	LAMP experiments completed.
Task 3e. Validation using NASA's EBF ³ apparatus	In progress; wire is being modeled in the code, initial result has been shown

2. Thermo-Fluid Model

A 3D numerical model for laser deposition by powder injection was developed, and simulation codes were run for different process parameters. In this model, the Piecewise Linear Interface Calculation (PLIC) scheme [1][2][3], which approximates the interface as a plane within a computational cell, was used to track the free surface. Compared to earlier versions of the Volume Of Fluid (VOF) methods [4][5][6][7], PLIC-VOF is more accurate and avoids the numerical instability[8]. It also can handle large interface deformation. Surface tension was modeled as a volume force using the Continuum Surface Force (CSF) model [9], combined with a force-balance flow algorithm [10]. The basic idea underlying the CSF model is the representation of surface tension as a continuous force per unit volume that acts in a finite transition region between the liquid and gas phases. The interface curvature was calculated using the height function (HF) technique.

The spatial concentration profile of the converged coaxial powder flow was considered as a Gaussian distribution [11], as defined in the following equation:

$$C(r, l) = C_{peak}(l) \exp\left(-\frac{2r^2}{R_p^2}\right)$$

(2-1)

where C is the powder concentration (the number of powder particles per unit volume), which is a function of the radial r and axial l distances in an axial-symmetrical coordinate, C_{peak} is the powder concentration at the center of powder flow ($r = 0$), and R_p is the effective radius of the powder stream at position l .

The governing equations were discretized in the physical space using the finite volume method. A forward-staggered, fixed grid was used, in which scalar quantities were located at the geometric center of the cell, while velocity components were situated at the cell face centers. To discretize the advection terms, the flux limiter scheme MUSCL (Monotone Upstream-centered Schemes for Conservation Laws) [12] were applied to improve the accuracy of the upstream approximation and enforce the weak monotonicity in the advected quantity. The computational cycle can be described through the following iterative steps:

- 1) Mass/momentum conservation equations and the related boundary conditions are solved iteratively using a two-step projection method [13] to obtain velocities and pressures. The

second step of the two-step projection method requires a Poisson equation to be solved for the pressure field:

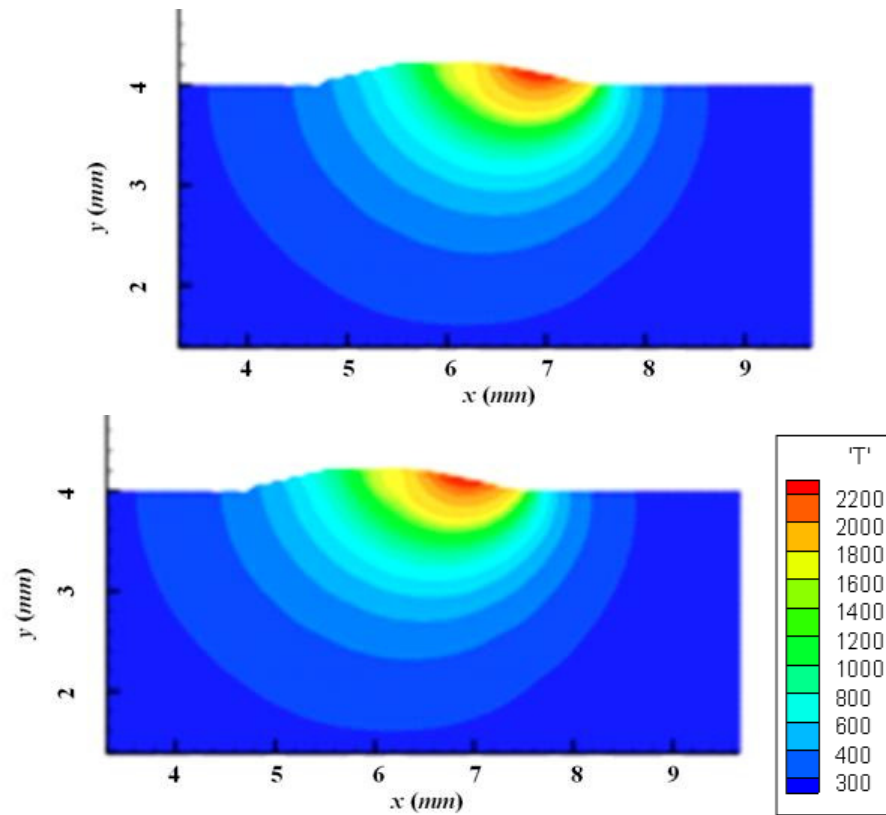
$$\nabla \cdot \left[\frac{1}{\rho^n} \nabla p^{n+1} \right] = \frac{\nabla \cdot \tilde{\mathbf{V}}}{\delta t}$$

(2-2)

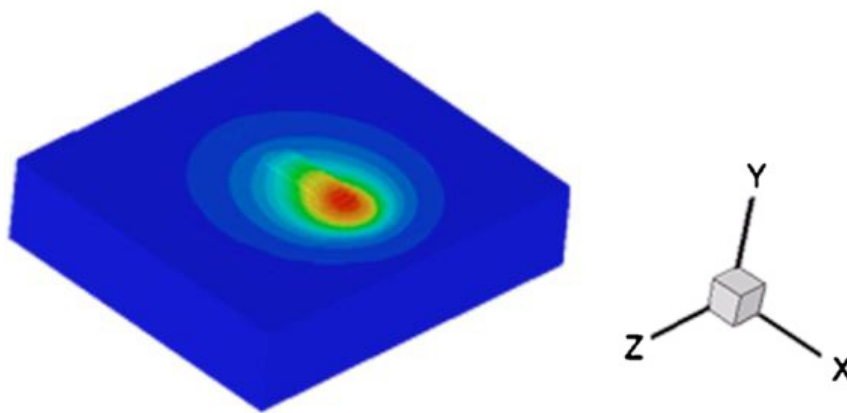
where ρ_n is the density from the old time step, p_{n+1} is the pressure to be solved at the new time step, and $\tilde{\mathbf{V}}$ is the temporary velocity field computed from the first step. The density retained inside the divergence operator in Eq. (2-2) results in an extra term proportional to $\nabla \rho$, which contributes to the pressure solution within the free surface transition region where $\nabla \rho \neq 0$. The system of linear equations formulated from the finite volume approximation of Eq. (2-2) was solved with an ICCG (Incomplete Cholesky Conjugate Gradient) solution technique[14]. Thermo-physical properties used in this step are computed from the old temperature field.

- 2) The energy conservation equation is solved by a method [15] based on a finite volume discretization of the enthalpy formulation. Once the new temperature field is obtained, the thermo-physical properties are updated.
- 3) Eq. (15) is solved using the PLIC-VOF [1,2,3] to obtain the updated free surface geometry of the melt pool and thermal field.
- 4) Advance to the next time step and back to step 1 until the desired process time is reached.

A predicted 3D track of the process is illustrated in Figure 2.1. A melt pool is generated at the front of the track with the moving laser beam. The melt solidifies very quickly due to the very high attendant cooling rate and forms a solid track shortly after the laser moves away. The heat absorbed by the molten pool dissipates into the track layer and substrate quickly. The laser energy affects a small zone and does not degrade the material elsewhere. Corresponding cross sections along the scanning direction are also displayed. As can be seen, the intense heat causes substrate melting, which generates a good bond between the track and base material. To better examine the fluid motion in the melt pool and mushy zone, sequential velocity fields in cross sections along the scanning direction are separately shown in Figure 2.2. The melt flows from the laser center area toward the periphery of the melt pool due to the Marangoni force. The fluid velocity decreases when the melt flows through the mushy zone where a damping effect in a porous media occurs.



(a) Cross sectional view



(b) 3D view

Figure 2.1 3D Deposition Profile and Temperature Distribution with Cross Section at $t = 0.11$ s. Laser moves along +X direction in cross sectional and 3D view. (Beam diameter: 2.5 mm, laser power: 416 W, travel speed: 375 mm/min, and powder mass flow rate: 6.25 g/min.)

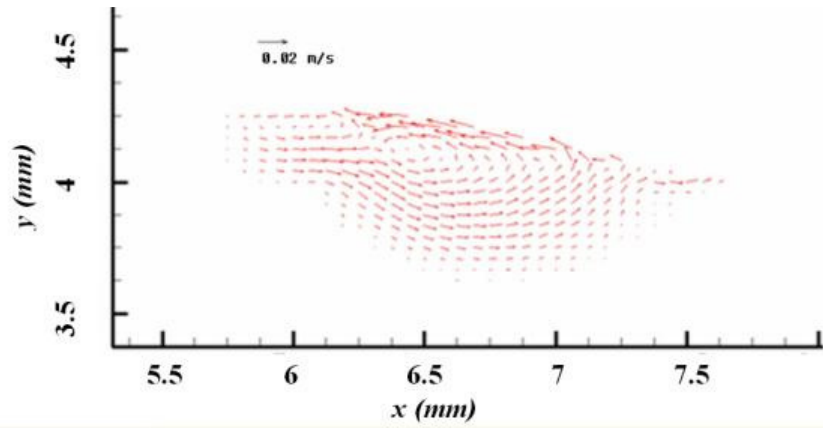


Figure 2.2 Fluid Velocity Fields in the Melt Pool in Cross Section along the Laser Scanning Direction at $t = 0.11$ s. (Beam diameter: 2.5 mm, laser power: 416 W, travel speed: 375 mm/min, and powder mass flow rate: 6.25 g/min.)

3. Wire Model Introduction

3.1. Introduction

Based on the previous cladding code, a wire feeding model was added to this code. In the first step, it was necessary to construct the wire to clear the wire position. When feeding a solid wire, as depicted in Figure 3.1, the rectangle was assumed to be a wire. Half of the known rectangular width was set as r . M_0 was the midpoint of the rectangular width, and M_1 was the intersection point of the extension of the long side and the horizontal line. The length of M_0M_1 was set as d . The height to feed y and the distance to feed x also were known. As Figure 8.1 illustrates,

$\theta_1 = \theta_2$ can be achieved; therefore, according to $\cos\theta_1 = \cos\theta_2$, the equation $r/d = y/\sqrt{x^2 + y^2}$ can be achieved. Then, d can be expressed with r , x , and y . If $MM_0 < d$, then point M can be assumed to be inside the wire position; if not, it does not belong to the wire. Finally, the wire position can be assumed.

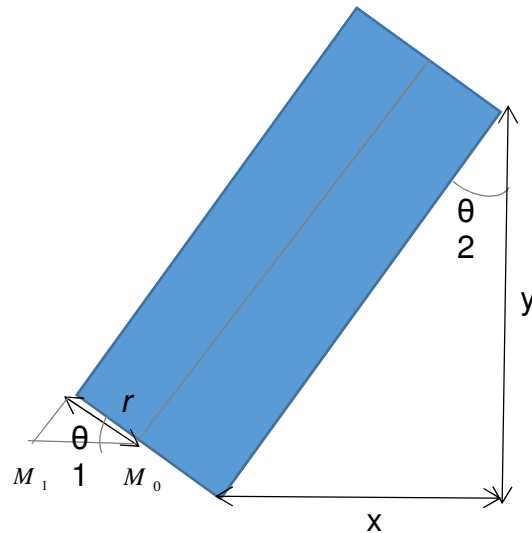


Figure 3.1 Wire position scheme

The simulation result shown in Figure 3.2 was achieved by adding this part to the cladding 3D code.

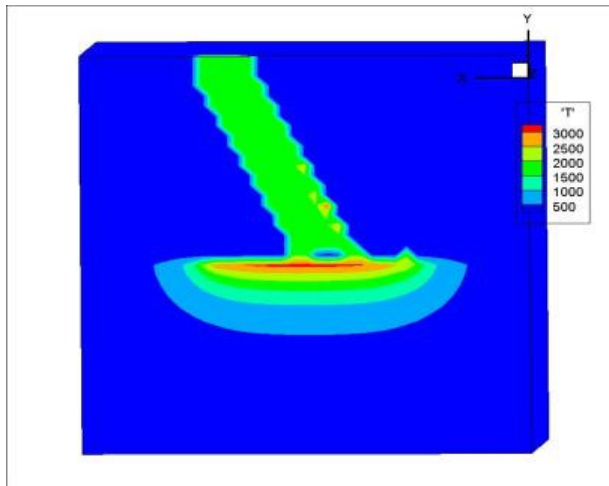


Figure 3.2 Simulation result of wire and molten pool

The wire shape can be seen from the simulation results.

3.2. Analysis

For the next step, some solver methods needed to be considered in the wire model to make the results more reasonable and to simulate the fluid-solid interaction. Many effects need to be considered when simulating this model. According to how mesh changes within a deforming body, three kinds of methods can be used, the Lagrangian, Eulerian, and ALE methods.

The most important issue is to solve the solid-liquid interaction problem for the wire model,. The ALE (Arbitrary Lagrangian Eulerian) method can be used to handle the moving solid boundary. In the ALE method, the material moves in some arbitrarily specified way to enable continuous rezoning. Freedom in moving the computational mesh enables greater distortions of the continuum and more resolution than that allowed by the Lagrangian or Eulerian methods. Thus, the ALE formulation combines the advantages of the Lagrangian and Eulerian methods. The principle of an ALE code is based on the independence of the finite element mesh movement with respect to the material motion.

The method aims to achieve as "Lagrange-like" behavior as possible, while simultaneously keeping the mesh distortions at an acceptable level. When using the ALE technique in engineering simulations, the computational mesh inside the domains can move arbitrarily to optimize the shapes of elements, while the mesh on the boundaries and interfaces of the domains can move along with materials to precisely track the boundaries and interfaces of a multi-material system. ALE-based finite element formulations can reduce to either Lagrangian-based finite

element formulations by equating the mesh motion to the material motion, or Eulerian-based finite element formulations by fixing the mesh in space.

The sales code [16] that includes the ALE algorithm follows the general flow chart in Figure 3.3. The key parameter, velocity, was determined from many functions when tracing.



Figure 3.3 General flow chart of the sales code

Depending on the type of calculation (Lagrangian, Eulerian, or other), the shape of the mesh first must be modified. In the purely Lagrangian case, this allows the computing grid to follow the fluid motion exactly. The new set of grid vertex velocities over the entire mesh are computed using this equation everywhere:

$$u_G = u_L \quad v_G = v_L$$

However, large fluid motions would create devastating effects such as contorting cells to extreme aspect ratios or even turning cells inside out. It is often possible to ameliorate these effects by moving the mesh vertices with respect to the fluid so as to maintain a reasonable mesh structure.

For a purely Eulerian calculation, the following equation can be used:

$$u_G = 0 \quad v_G = 0$$

Whenever a vertex is moved relative to the fluid, however, the cells surrounding the vertex must exchange material. SALE allows a broad spectrum of rezoning possibilities by treating this material exchange as an advective flux. The simplest case is that of a purely Eulerian flow, in which the vertices are moved back to their original positions every cycle. Between this extreme and the Lagrangian extreme lies whatever form of continuous or discrete rezoning the user wishes.

For a continuous re-zoning, grid velocities are chosen to lie somewhere between these two extremes. In particular, the vertices are moved according to some relaxation rate to place vertices at the average position of the neighboring vertices. This usually maintains cells of reasonable size and proportion throughout a run. Once a set of grid velocities U_G and V_G have been defined, it is a simple matter to construct the new grid and perform whatever advective flux calculations may be required.

In the *regrid* function, the vertices are moved to new locations as specified by (U_G, V_G) . Then, a set of relative velocities (U_{rel}, V_{rel}) is formed to simplify the later task of calculating advective fluxes. For this purpose, the vertex velocities with respect to the fluid are:

$$\bar{u}_{REL} = \bar{u}_G - \bar{u}_L$$

Then, the vertices are moved to new locations. The new grid coordinates can be computed:

$$\bar{x}_i^{n+1} = \bar{x}_i^n + \delta t \cdot \bar{u}_G$$

In all cases except for the purely Lagrangian calculation, the relative velocities are not zero, and the advective flux of mass, energy, and momentum between cells must be calculated. The flux calculation is performed on a cell-by-cell basis. For every cell, the volume swept out by each of the four faces relative to their Lagrangian positions is calculated.

Using the concept of a cell-centered momentum flux, the average cell-centered momenta is based on the vertex velocities:

$$umom_{ij} = \frac{1}{4} * rol_{ij} * (ul_{ij} + ul_{i+1,j} + ul_{i,j+1} + ul_{i+1,j+1})$$

$$vmom_{ij} = \frac{1}{4} * rol_{ij} * (vl_{ij} + vl_{i+1,j} + vl_{i,j+1} + vl_{i+1,j+1})$$

Then, advection changes the cell momenta as a function of the cell-centered quantities. The net advection changes in cell-centered momentum components are given by:

$$umomp_{ij} = f(umom, s)$$

$$vmomp_{ij} = f(vmom, s)$$

These changes are then apportioned back to the vertices and converted to vertex velocity changes in the next step. Then, the vertex quantities can be updated.

First, the new vertex masses must be calculated from the averages of the new cell masses, and a mass must be assigned to each vertex to obtain the time advanced velocities. In SALE, it is assumed that the mass in each cell is shared equally between its four corner vertices:

$$M_{ij} = \frac{1}{4} (M_{i+1/2, j+1/2} + M_{i-1/2, j+1/2} + M_{i-1/2, j-1/2} + M_{i+1/2, j-1/2})$$

Secondly, to adjust the velocities, the initial values set at all vertices are replaced by new time step values:

$$(u_{ij})^{n+1} = (u_L)_{ij} \frac{M_{ij}^n}{M_{ij}^{n+1}}$$

Finally, the cell-centered momentum changes are distributed to each vertex of the cell:

$$(u_{ij})^{n+1} = (u_{ij})^{n+1} + \frac{1}{4} * \frac{umomp_{ij}}{M_{ij}^{n+1}}$$

After this section, the code returns to the beginning to start another time step using the new values.

The fluid–structure interaction problems involving a free surface can be classified as follows:

- 1) Rigid containers carrying a fluid with a free surface
- 2) Rigid floating bodies
- 3) Submerged rigid bodies moving close to a free surface

When modeling the wire feed process, the first step is to find the equations of motion for the structure as functions of the interaction pressure. The second step is building a boundary-value problem for the pressure as a function of the acceleration of the structure. The third step deals with coupling the pressure solution with the equations of motion of the structure.

When implementing the ALE method in the wire feed, the general method was simplified. For the case of fluid-rigid body interaction, the wire was modeled as a rigid body. For it to be classified as merged solid and non-merged solid, in the proposed wire model, the nonmerged solid and free surface modeling need to be taken into account. A numerical method that can simulate this interaction requires coupling between the fluid solver and a code for the structural dynamics. Just like the original code, the fluid is modeled with the Navier-Stokes equations. The mass and momentum conservation equations are as follows:

$$\nabla \vec{V} = 0$$

$$\frac{\partial}{\partial t} (\rho \vec{V}) + \nabla \cdot (\rho (\vec{V} - \vec{V}_s) \vec{V}) = \nabla \cdot (\mu_t \frac{\rho}{\rho_l} \nabla \vec{V}) - \nabla p - \frac{\mu_t}{K} \frac{\rho}{\rho_l} (\vec{V} - \vec{V}_s) + \rho \vec{g} + S_1$$

The free-surface dynamics are tracked using the Volume of Fluid (VOF) method. The VOF-type interface-capturing method is used to compute the deformation of the free surface:

$$\frac{\partial F}{\partial t} + (\vec{V} - \vec{V}_s) \cdot \nabla F = 0$$

The motion of the rigid body in the six degrees of freedom is described by the equations of linear and angular momentum, set in the inertial reference frame, and given by the following two equations:

$$M\ddot{X} = \bar{F}$$

$$RIR^{-1}\dot{\bar{\Omega}} + \bar{\Omega} \times RIR^{-1}\bar{\Omega} = M_G$$

Here, M is the boat mass, \ddot{X} is the linear acceleration of the center of mass, \bar{F} represents the force acting on the boat, $\dot{\bar{\Omega}}$ and $\bar{\Omega}$ are the angular acceleration and velocity, respectively, M_G is the moment with respect to G acting on the boat, I is the tensor of inertia of the boat about the body-fixed reference system axes, and R is the transformation matrix between the body-fixed and the inertial reference systems.

The equation of variation of angular momentum in the form referred to as the center of gravity is:

$$\bar{T}\bar{T}_G^{-1}\dot{\bar{\Omega}} + \bar{\Omega} \times \bar{T}\bar{T}_G^{-1}\bar{\Omega} = \bar{M}_G$$

where $\dot{\bar{\Omega}}$ and $\bar{\Omega}$ are the absolute angular acceleration and angular velocity, respectively, \bar{M}_G is the total moment with respect to G , and \bar{T}_G is the tensor of inertia of the body about the (G, x, y, z) axes.

To simulate the motion of bodies floating freely at the free surface, the equations of motion of the rigid body can be solved together with the flow solver. In the coupling with the flow solver, the 6DoF dynamical system receives, at each time step, the value of the forces and moments acting on the rigid body, and it returns the values of the new position, as well as linear and angular velocity. In the flow solver, these data are used to update the computational grid by a mesh motion strategy based on elastic analogy. The flow equations in ALE form are solved in the new domain.

The general idea is to decouple the problem in the following way. The flow solver computes the flow around the body as usual. Taking into account the fluid viscosity, flow turbulence, and deformation of the free surface, the forces and moments acting on the body are then calculated by integrating the normal (pressure) and tangential (friction) stresses over the body surface.

Following this, the rigid body equations can be solved using these forces and moments as input data at each time step, and the motion accelerations, velocities, and displacements (translations and rotations) are obtained by integrating in time. The position of the body is then updated, and the fluid flow is computed again for the new position. In the flow solver, these data are used to update the computational grid, and the flow equations in ALE form are solved in the new domain. By iterating this procedure over time, the body trajectory is obtained.

However, many problems still need to be solved. For example, the ALE differential form of the conservation equations for mass, momentum, and energy need to be rewritten in another form.

All one must do to obtain the ALE form of the conservation equations is to substitute in the various convective terms, such as the material velocity with the convective velocity. The ALE differential and integral forms of the conservation equations will be reset and used as a basis for the spatial discretization of problems in the fluid dynamics and solid mechanics.

In addition, the computer implementation of the ALE technique requires the formulation of a mesh-update procedure that assigns mesh-node velocities or displacements at each time step of a calculation. The remesh algorithm strongly influences the success of the ALE technique.

Also, mesh regularization is necessary to keep the computational mesh as regular as possible during the entire calculation in order to avoid excessive distortions, squeezing of the computing zones, and to prevent mesh entanglement to decrease the numerical errors caused by mesh distortion.

The boundary conditions are of utmost concern in the discussion of the specificities of the ALE formulation in fluid dynamics. The same boundary conditions employed in Eulerian or Lagrangian descriptions are implemented in the ALE formulation. Along the boundary of the domain, kinematical and dynamical conditions must be defined. Along solid-wall boundaries, the particle velocity is coupled to the rigid structure. Due to the coupling between the fluid and structure, specific conditions are needed to ensure that the fluid and structural domains will not detach or overlap during the motion. These coupling conditions depend on the fluid. For a viscous fluid, the coupling between the fluid and structure requires that velocities coincide along the interface. In practice, two nodes, one fluid node and one structural node, are placed at each point of the interface. The fluid is treated in the ALE formulation; the movement of the fluid mesh may be chosen completely independently of the movement of the fluid itself. The equations for a Newtonian fluid in terms of stress and the strain rate need to be solved, and in three dimensions, the strain rate in each cell should be calculated from the velocity gradient, taking other equations into account.

3.3. Future Work

The condition where the wire is implemented just above the melt pool, instead of feeding a solid wire into contact with the liquid based on previous cladding code, will need to be simulated. The complete wire feeding model needs to be done in the future work.

4. Parallel Computing

A Message Passing Interface (MPI) was designed for high performance on both massively parallel machines and workstation clusters. MPI, now being used for parallel computing, is a specification for the developers and users of message-passing libraries. The goal of MPI is to provide a widely used standard for writing message-passing programs. The interface attempts to be practical, portable, efficient, and flexible. MPI specifications have been defined for C/C++ and Fortran programs [17].

To parallelize the ICCG solver, using the parallelize version of the PCR solver [18] as a guide, the ICCG code was divided and then grouped into the following 14 different files: surf10.cpp, mpi_slice_moves.cpp, init_funcs.cpp, iccg.cpp, functions.h, functions.cpp, function_prototypes.h, extern_globals.h, convection.cpp, constants.h, comp_cal.cpp, cladding3Dmpi.cpp, bc_funcs.cpp, makefile. Each file consists of related function(s)/variables. For instance, the integer variables are saved in the “constants.h” file, while float variables are saved in the “extern_global.h” file. The 3D arrays F, FN, and FP were identified as those that require two slices, so they were indexed with the “fbi” variable. Similarly, the 1D arrays DX, RXD, and XI were indexed with the “gi” variable, indicating that each node must have its own copy of each of these arrays.

In cases in which the for() loop was once for (i=0; i<IMAX; i++), the loop has been changed to for (i=imaxBeg; i<imaxEnd;i++)^[18]. Similarly, in cases in which the for() loop was once for (i=1; i<IM1; i++), the loop has been changed to for (i=im1Beg; i<im1End;i++)^[18].

The complexity of indexing in the ICCG solver also was reduced by categorizing nodes into three different natural types: node_0, mid-nodes, and the end node.

```
if (myRank == 0) {
    nodePos = NODE_0;
    imaxBeg=0; imaxEnd=sliceN;
    im1Beg=1; im1End=sliceN;
}
else if (myRank < numMPINodes-1) {
    nodePos = NODE_i;
    imaxBeg=1; imaxEnd=sliceN+1;
    im1Beg=1; im1End=sliceN+1;
}
else if (myRank == numMPINodes-1) {
    nodePos = NODE_N;
    imaxBeg=1; imaxEnd=sliceN+1;
    im1Beg=1; im1End=sliceN;
} [18]
```

Finally, at the end of each for() loop, the sliceMove() function was used to update the ghost slices for those arrays whose values had changed.

The results from the temperature files retrieved from the current paralleled version are as follows:

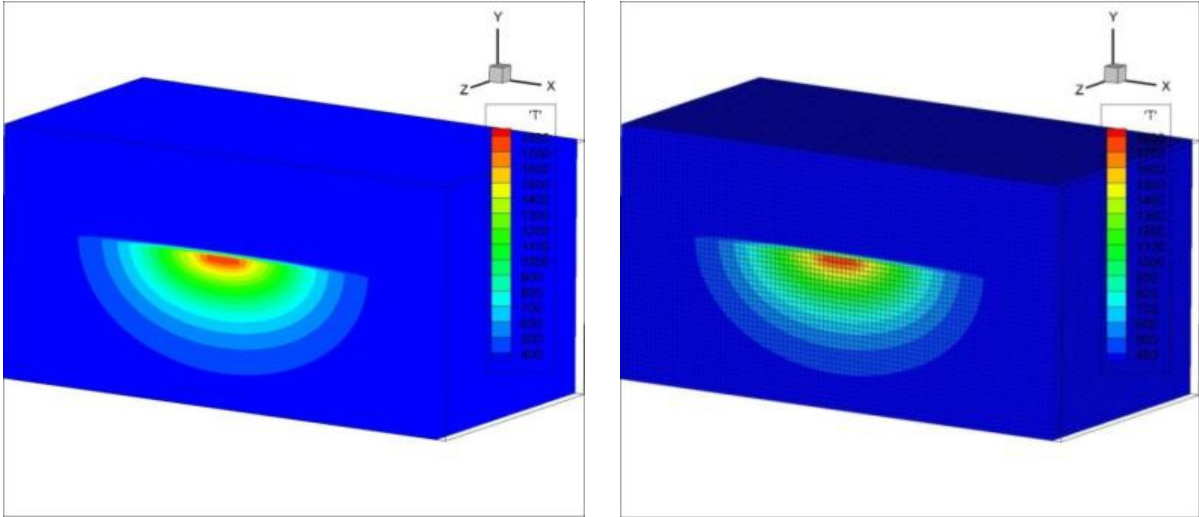


Figure 4.1 Results from the serial code

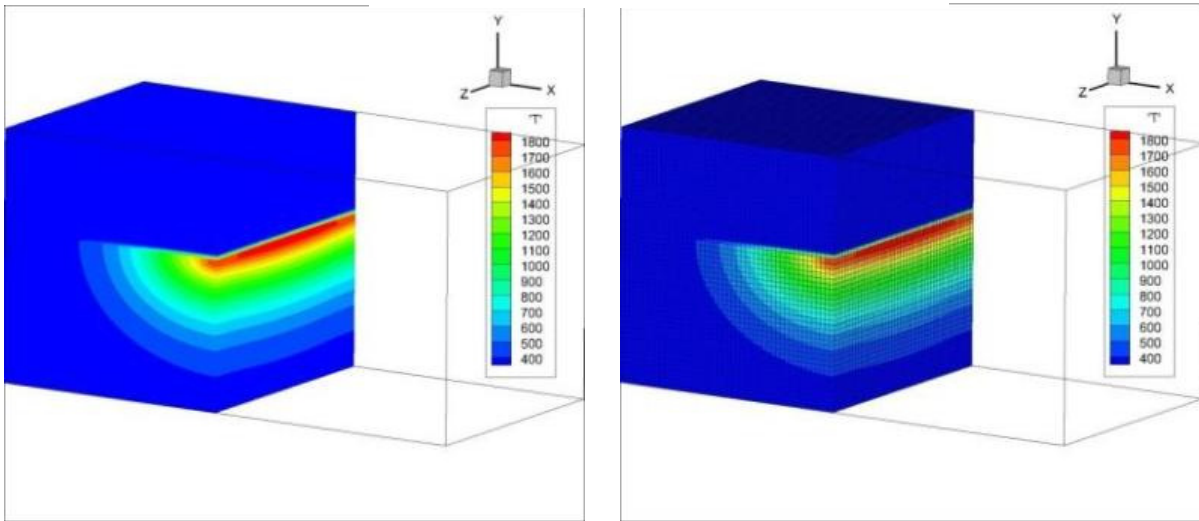


Figure 4.2 Picture of dividing model for the serial code

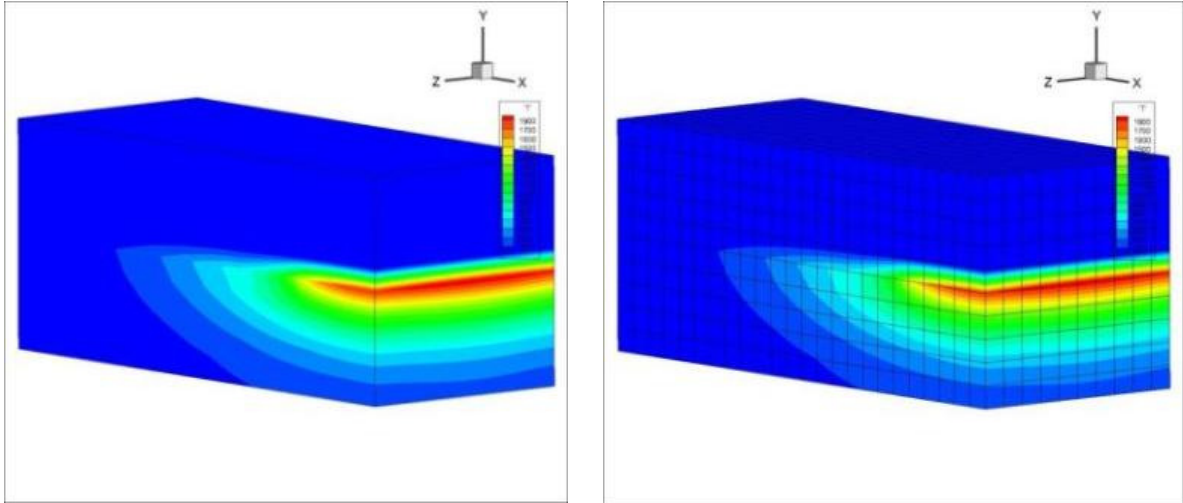


Figure 4.3 Results of the left half model for the parallel code

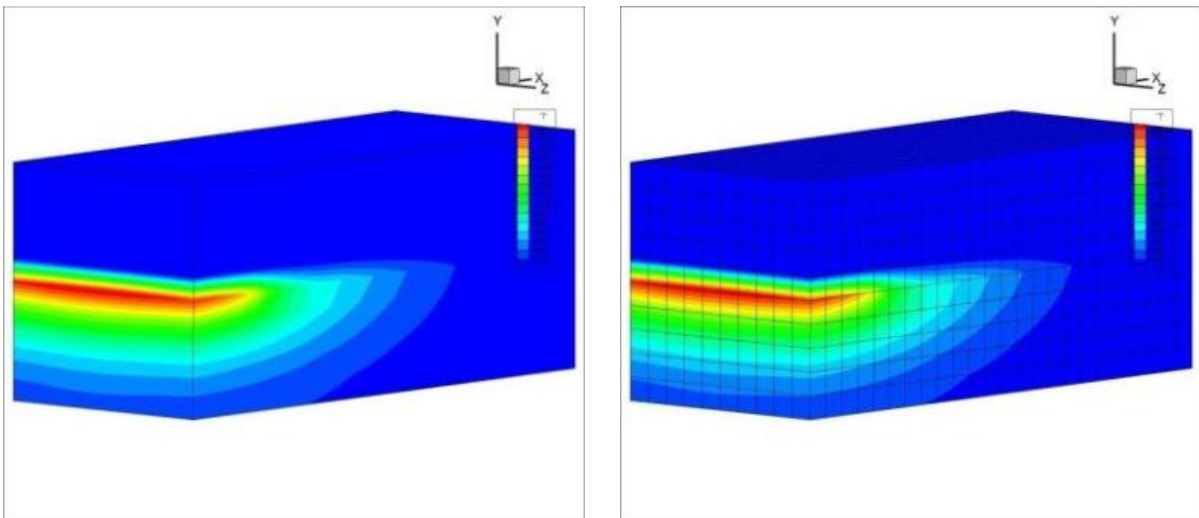


Figure 4.4 Results of the right half model for the parallel code

The meshing grid pictures show that there was one layer above the hottest grid that was within one grid. The interpolation method was used to calculate the temperature across the melt pool, so the extra layer was derived using the mean value of room temperature (blue part in the figures) and the highest temperature (red part in the figures).

The code appears as follows:

```

F_SUM3 = F_SUM3 + F[fbi+3][M][N];
F_SUM3 = F_SUM3 + F[fbi-3][M][N];
if (FP[fbi+3][M][N]>=EMF1 && F[fbi+3][j][k] < EMF)
    FOFPPP = 0.0;

```

```
if (FP[fbi-3][M][N]>=EMF1 && F[fbi-3][j][k] < EMF)
    FOFMMM = 0.0;
```

The variables “F” and “FP” both require three slices. In the allocation section, TotSlices3 was added for processes that require one or two ghost slices.

```
if (nodePos == NODE_0 || nodePos == NODE_N)
    {
        // end procs need 1 ghost slice
        TotSlices=sliceN+1;
        TotSlices2=sliceN+2;
        TotSlices3 = sliceN+3;
    }
else
    {
        // all others need to keep 2 ghost slices
        TotSlices=sliceN+2;
        TotSlices2=sliceN+4;
        TotSlices3=sliceN+6;
    }
```

For cases in which nodePos does not equal NODE_0, fbi=i+1 has been changed to fbi=i+2, as follows:

```
if (nodePos == NODE_0 )
    {
        fbi=i; gi=i+slice0_G;
    }
else
    {
        fbi=i+2; gi=i+slice0_G-1;
    }
```

The MPI functions were compiled on the cluster successfully. Some C++ needs to be included in directives to the header of the makefile to complete the successful compilation of the code.

However, some “subscript out of range” issues still remain that cause the solver to crash. These issues existed in the sequential version of the ICCG solver and transferred to the parallel version.

Some functions need to be synchronized across the different cores. We wrote the following function to achieve this functionality:

```
void synchronizeFlag(int &flag, int syncStyle) {
    MPI_Barrier(MPI_COMM_WORLD);
    bool IsSame = true;
    int *tempFlag = (int *)malloc(sizeof(int)*I);
    tempFlag[0] = flag;
    int *flagsVector = NULL;

    if (myRank == 0) {
        flagsVector = (int *)malloc(sizeof(int) * numMPINodes);}
}
```



```

MPI_Barrier(MPI_COMM_WORLD);
MPI_Gather(&tempFlag[0], 1, MPI_INT, flagsVector, 1, MPI_INT, 0,
MPI_COMM_WORLD);
MPI_Barrier(MPI_COMM_WORLD);

if(myRank == 0){
    for(int i=1; i<numMPINodes; i++){
        if(flagsVector[0] != flagsVector[i])
            IsSame = false;}
    if(IsSame != true){
        switch(syncStyle){
            case 0:
                tempFlag[0] = computeMinimumFlag(flagsVector);
                break;
            case 1:
                tempFlag[0] = computeMaximumFlag(flagsVector);
                break;}}
    MPI_Barrier(MPI_COMM_WORLD);
    MPI_Bcast(tempFlag, 1, MPI_INT, 0, MPI_COMM_WORLD);
    flag = tempFlag[0];

    // free stuff
    free(tempFlag);
    free(flagsVector);
}

```

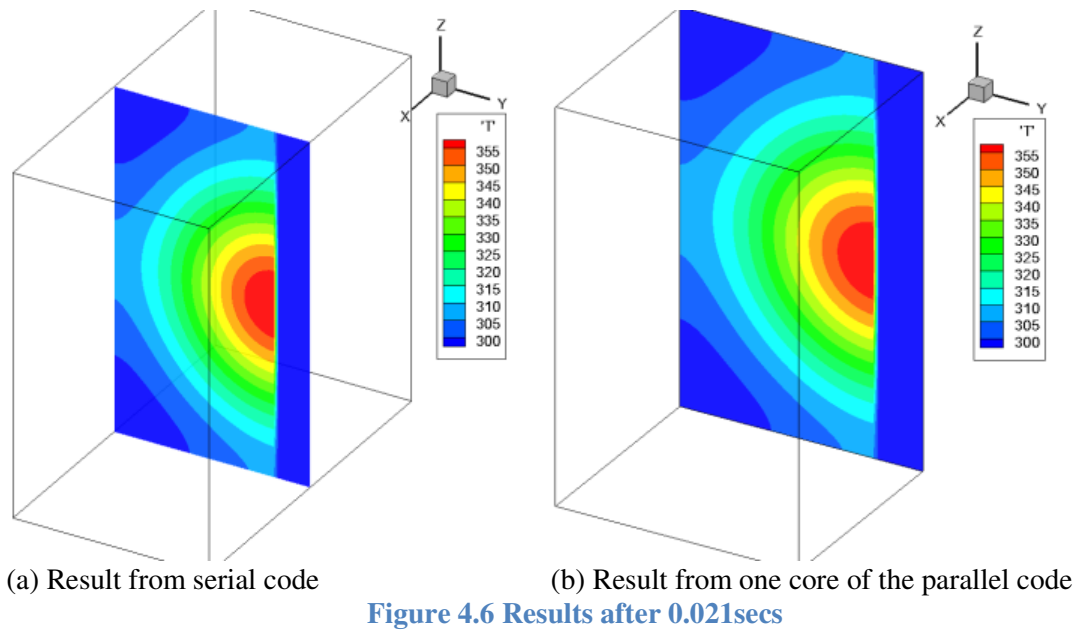
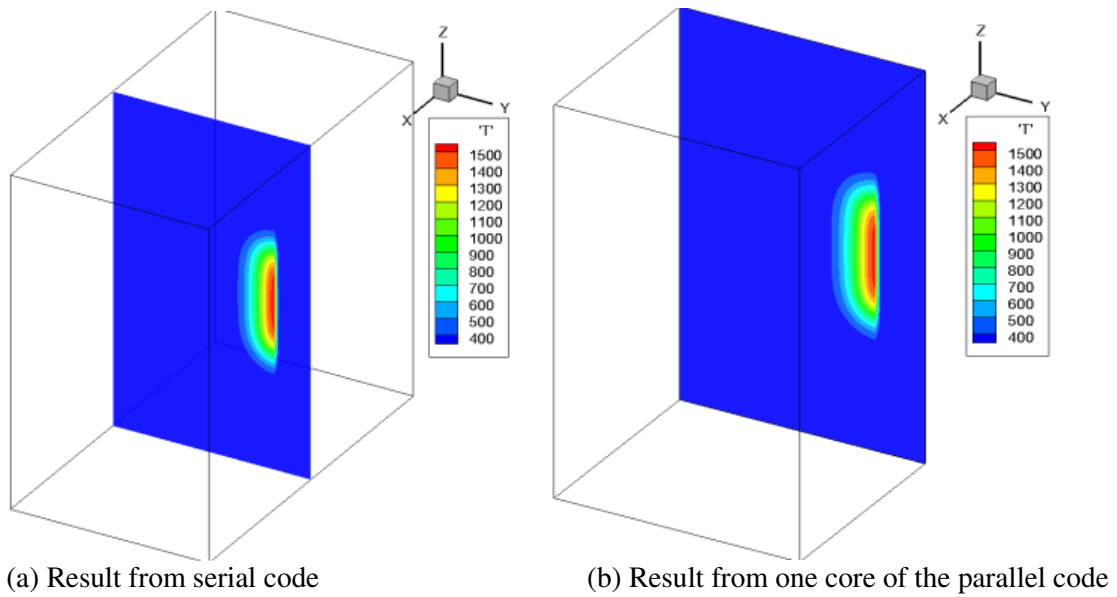
Using the above function, the following flags were synchronized: FLGMELT, FLGVLCT, DELT, FLGC, NFLGC, and NOCON.

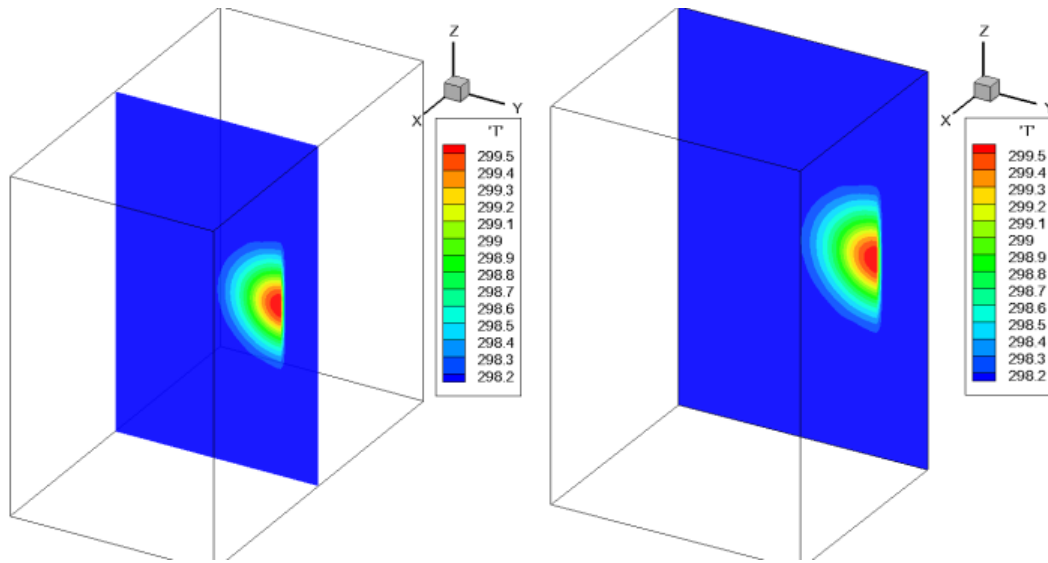
We tested heat conduction in both the serial and parallel codes under the following parameters:

Table 4.1 Simulating parameters

Parameter	Value
Domain Length (mm)	3.2
Domain Height (mm)	1.84
Domain Width (mm)	3.2
Substrate Height (mm)	1.47 (80% of Domain Height)
Element Size (μm)	40
Laser Power (watts)	1000
Pulse Width (secs)	0.001

The results were as follows:





(a) Result from serial code

(b) Result from one core of the parallel code

Figure 4.7 Results after 0.0013secs

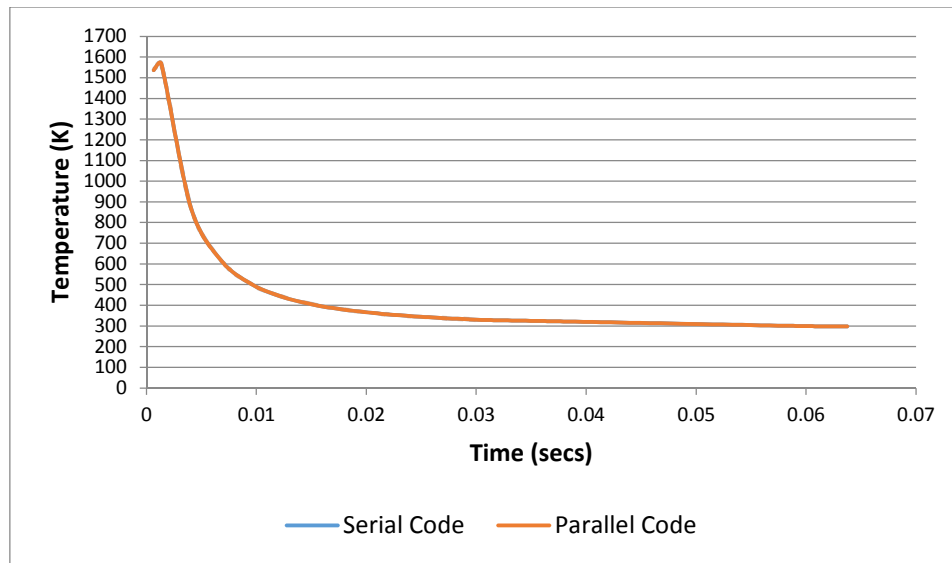


Figure 4.8 Cooling curve (serial and parallel results overlapped)

Figure 4.5 through Figure 4.8 indicate that the results from both the serial and parallel codes were similar.

5. Smoothed Particle Hydrodynamics Model

5.1. Abstract

Smoothed Particle Hydrodynamics (SPH) is a new numerical tool useful for hydrodynamic simulations. Compared to traditional techniques such as the VOF method, SPH is a more convenient and robust technique for complicated simulations involving fluids. In this report, the modeled SPH is described briefly, and its advantages are noted through a comparison with the VOF model. The working principles of SPH are discussed, and the implementation of this technique in the python code is discussed in detail. The step-by-step flow of the program is discussed, and results are plotted.

5.2. Theory

The primary advantage of SPH over other computation techniques is that it is a mesh-free Lagrangian method. In the Lagrangian description, the position and physical properties of particles are described in terms of the material or referential coordinates and time. The SPH method works by dividing the fluid into a set of discrete elements, referred to as a particle. These particles have a spatial distance (known as the "smoothing length" and typically represented in equations by h) over which their properties are "smoothed" by a kernel function. This means that the physical quantity of any particle can be obtained by summing the relevant properties of all the particles that lie within the range of the kernel [19].

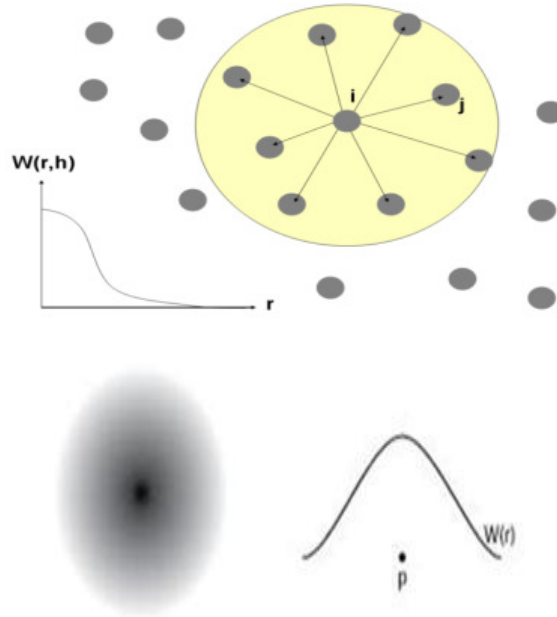


Figure 5.1 Pictorial representation of the kernel function and smoothing length

The contributions of each particle to a property are weighted according to their distance from the particle of interest and their density [20]. Mathematically, this is governed by the kernel function (symbol W). Commonly used kernel functions include the Gaussian function and the cubic spline. The latter function is exactly zero for particles further away than two smoothing lengths (unlike the Gaussian, for which there is a small contribution at any finite distance). The latter function has the advantage of saving computational effort by not including the relatively minor contributions from distant particles.

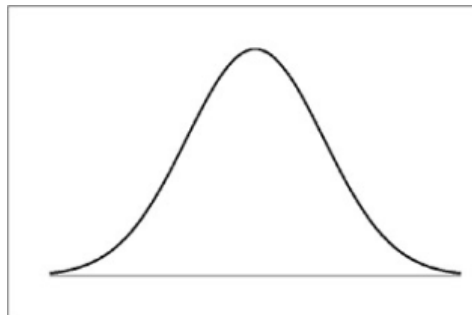


Figure 5.2 Gaussian curve

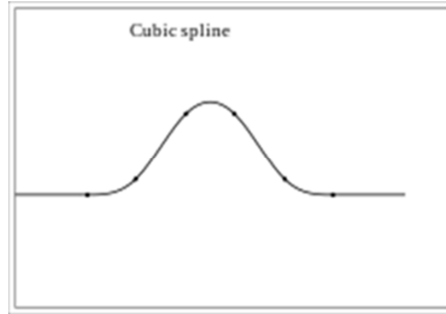


Figure 5.3 Cubic spline curve

To utilize the full power of SPH, the smoothing length can be varied over time. For example, the current simulation has two smoothing length values, one for relatively short length ranges, which computes forces such as compression, friction, etc., and one for long ranges, which computes forces caused by surface tension, etc. In the current simulation, only the fluid particles are considered as SPH particles for computational efficiency [21].

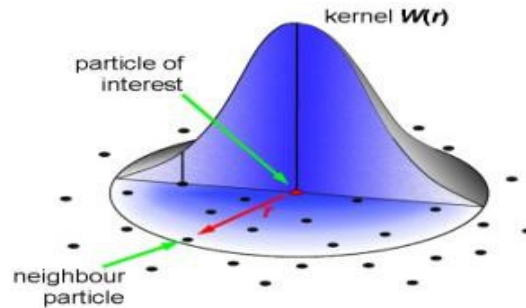


Figure 5.4 3D representation of the kernel function

5.3. Comparison with VOF Technique

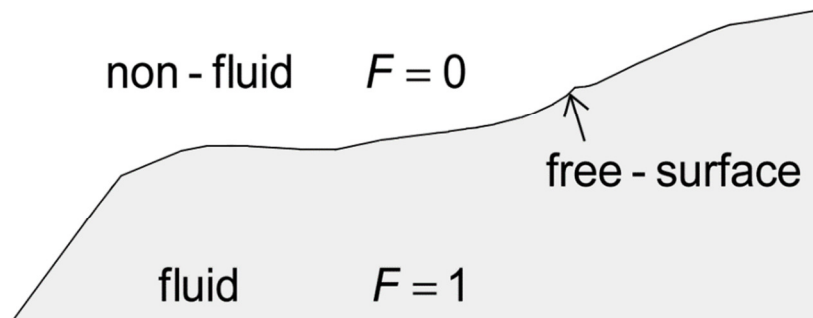
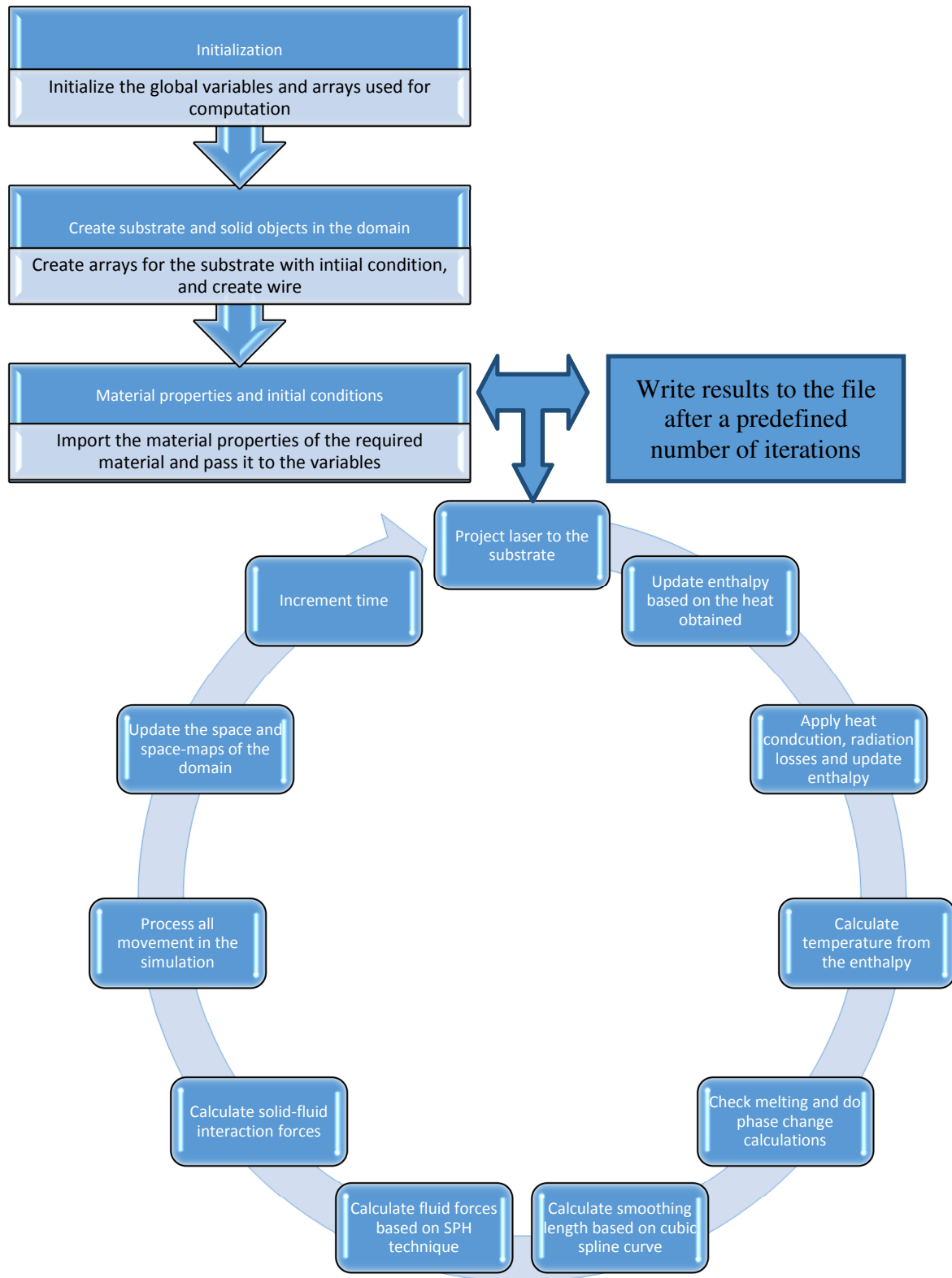


Figure 5.5 Non-fluid and fluid interface in VOF technique

The Volume of Fluid (VOF) technique uses fluid fractions to determine the fluid cells and solid cells. This technique primarily uses the Eulerian approach (fixed-grid method). The main disadvantage of the Eulerian approach is that it is difficult to conserve mass, as the cells have no mass of their own. However, in the SPH technique, each cell possesses its own mass, which is

conserved throughout the system. In the VOF technique, the motion of the fluid is computed from the momentum equations, including the Navier-Stokes equation, and many conditions to maintain continuity. The SPH technique eliminates all of these complicated equations, replacing them with much simpler force and velocity calculations [22]. Calculating the advection and solving the Pressure-Poisson equation take most of the computation time and make real-time processing unachievable. Separate solvers must be implemented to solve the inverse matrix calculation for the pressure matrix. In the VOF technique, the transport phenomenon by advection is implicit, requiring nested loops in three dimensions and taking most of the computation time. The VOF technique is very difficult to parallelize, as processors of the machine will be waiting for values from the other processors to finish computing. The SPH model is highly parallelizable because the fluid is considered as particles with their own physical properties. The primary advantage of the SPH model is that most of the calculation can be done explicitly. Hence, array operations, which are faster, can be used instead of nested loops.

5.4. Program Flow



6. SPH Model Implementation

6.1. Initialization

The global variables are set to their initial conditions in the beginning of the code. The dimension of the domain is specified with a desired resolution from which the grid size is calculated in three dimensions. The time step at which the iteration is to be calculated is specified and declared as a global variable, which adds to the total simulation time in each cycle. The arrays used are “ctypes”, which have the efficiency of C arrays and can be used in Python to do calculations while reducing memory usage.

The initial position of the laser in the domain, the velocity and power of the laser, and the type of distribution of power are specified as part of the initialization. Two types of laser power distributions exist in the current code: “top hat” and “Gaussian” beam. Figure 6.1 shows the distribution of each laser beam.

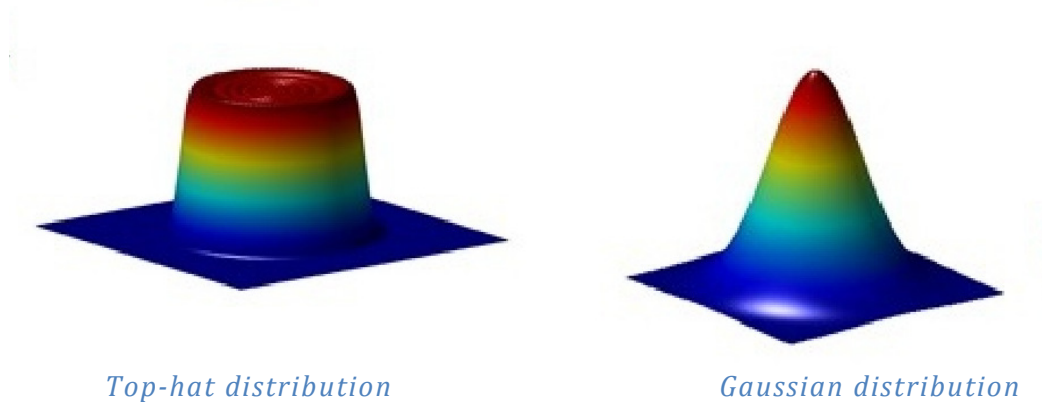
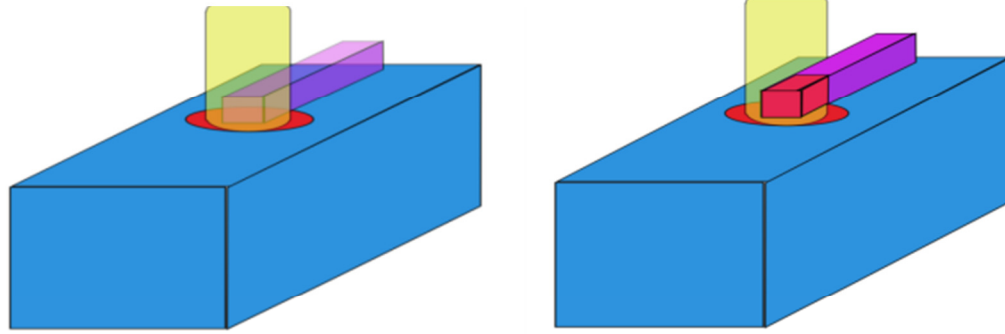


Figure 6.1 Two types of laser beam distribution

A laser map that has the indices of each column of the laser beam in the domain is created, with the power in that column according to the profile. This yields a more realistic “ray traced laser.” With the ray traced laser, the solid objects hit by the laser as it moves downward to the substrate are taken into account. This projected laser will cast a shadow of the solid that obstructs the rays in the substrate, which is more realistic than applying laser power onto the substrate alone. This approach is better explained in Figure 6.2, which shows the laser projected onto a substrate with a solid in between, with and without ray tracing.



Without ray-tracing

With ray-tracing

Figure 6.2 Laser projection on substrate scheme

6.2. Creating Solids and Applying Material Properties

The material properties are stored in a dictionary format for each material. This will allow more materials to be added into the file without changing the original code. The material used in the current code is Ti6Al4V and its properties. The next step is to create the solids used in the simulation. First, a substrate having the desired dimensions is created and placed in the domain with a user-defined offset. The program has functions that create cylinders, cuboids, spheres, frustums, discs, and other shapes. This shows that a solid of any shape can be added to the simulation. The substrate is declared as a fixed, solid object so that it will not be moved according to forces such as gravity. The material properties are applied to the solid, and the substrate is placed under ambient temperature. A temperature-enthalpy lookup table is created as a part of the initialization and used in the temperature calculation. The mass of the object is calculated based on the mass of each cell, which is calculated from the solid density and volume.

Wire is created in the same way substrate is created, as explained previously. The additional input values needed to create the wire include the diameter and length of the wire, which should not exceed the size of the domain. The next input value for the wire is its angle with respect to the X-Z plane and the X-Y plane. The velocity of the wire is a user-defined value, and the gravity of the wire is restricted to prevent the wire from falling on the substrate due to its own weight.

6.3. Iterative Calculations

The iterative calculation done at each time step is divided into 10 different steps.

6.3.1. Laser Projection

As explained previously, a ray traced laser is projected to the domain in the Z-axis. The heat from the laser is added to the enthalpy array at the intersection positions. The intersection position is obtained by tracing each ray down its column to find the first solid cell in its path.

6.3.2. Heat Conduction

The conduction calculation begins with the creation of a conductivity matrix. The conductivity value is given as a material property based on the temperature. The conductivity matrix is calculated through the interpolation of the range of values of “K” with the temperature. The next step is to create a gradient matrix based on the differences in temperature in three different axes. The heat due to conduction is then updated on the enthalpy matrix.

6.3.3. Radiation Losses

Radiation losses are subtracted from the skin cells of the solids because radiation is a surface phenomenon. To find skin cells, scipy-ndimage-morphology libraries are used, which include functions such as binary erosion and binary dilation for array operations. The enthalpy array is updated after radiation losses. Both the conduction and radiation loss function are performed in parallel, as the calculation of one does not depend on the other. This increases the speed and efficiency.

6.3.4. Temperature Calculation

The temperature is calculated from the enthalpy array, which was modified by the laser power, conduction, and radiation. The temperature array is computed by interpolating the enthalpy values with the temperature in the previously calculated temperature-enthalpy lookup table. Using the lookup table makes the computation much faster and avoids values exceeding a reasonable limit with larger time steps.

6.3.5. Phase-Change Calculation

The phase-change calculation is divided into three parts: checking melting, solidification, and creating voxels.

a) Checking melting

The melting process begins with checking the temperature array and finding the indices of cells exceeding the melting temperature of that material. The indices are mapped with a temporary array to form new fluid cells. The function that creates new fluid cells creates a list of fluid

positions, fluid indices, fluid velocities, and fluid forces. The fluid velocities are inherited from the solid cells, and forces are declared as zero when created because they will obtain their value in the next step.

b) Solidification

The liquid cells can solidify in the simulation due to conduction, radiation, and movement of the laser. The fluid cells are mapped with the temperature array to check for cells with temperatures less than the solidus temperature of the material. These cells are deleted from the fluid lists and added back to the solid cells.

c) Creating voxels

The final step in a phase change is to create the arrays required for fluid computation based on the results given by melting and solidification. The values computed by this function are used later to create SPH particles and fluid movement. Arrays such as fluid space are created and the fluid positions determine the location of the cells. This will indirectly help the movement of the fluid because the fluid position is the variable that will be updated in the move function, which is explained later.

6.3.6. Updating Smoothing Length

The smoothing length is calculated here from a kernel function, which is cubic spline in the current model because of computational efficiency. This step in the calculation can be considerably slower as more fluid cells are added into the simulation. Hence, parallel computing requirements are high in this step. For efficient parallelization, a list consisting of reference numbers of fluid particles and their positions is created. This list will have multiple lists of fluid particles, considering two particles at a time. A cubic spline worker function calculates the smoothing length for two interacting particles. The list is passed to a multiprocessing pool that conducts the above operation in parallel, saving computation time and using resources efficiently. The final output of this function is a list of lists, with each list having the position of the two interacting particles, the direction of interaction, smoothing length 1 for a short range of forces, and smoothing length 2 for a higher range of forces.

6.3.7. Calculating Fluid Forces

In this step, the SPH model is applied to the fluid particles. The fluid forces, which were declared as zero in the phase change step, are changed to gravity forces in this step. The list created in the previous step is used in this function. Each pair of particles is taken one at a time to find forces such as the compression force, friction force, and force due to surface tension. Smoothing length 1 is used for compression and friction forces, and smoothing length 2 is used for the surface

tension force. Material properties such as stiffness, viscosity, and surface tension are taken into account in finding these forces. The forces are added to one fluid particle and subtracted from the other based on the direction of the force.

6.3.8. Solid-Fluid Interaction Calculation

In this step, the interaction forces between the solid and the fluid are computed. The first step in this calculation is to find the neighboring cells of each fluid particle in three dimensions and check if they are solid cells. The smoothing lengths are calculated for the interacting pairs in the same way they were calculated in the previous steps. The reaction forces and friction forces are computed using the two smoothing lengths, respectively, and added in the direction of action. The forces added in the fluids are subtracted from the solid body.

6.3.9. Movement

The movement function can be divided into four different motion calculations:

a) Moving solids

In this step, each solid body is moved with its predefined velocity. In the current simulation, the substrate is stationary, and the wire moves with a velocity in the angle in which it was created in the domain. Movement due to gravity forces is computed in this step, but because the gravity is restricted for the wire and the substrate is fixed, the force of gravity has no influence on this solid. However, the gravity force becomes a critical factor in fluid and simulating powder problems.

b) Collision

The next step in the movement calculation is to check for collision. Each solid has a parameter named “target” that determines whether the solid is to be considered for collision calculation. This condition is checked in the beginning and, if true, is passed to a function that checks for collision by determining if the space arrays of two solids overlap; any overlapping indices are returned for further calculations. In the current simulation, if two solids collide (i.e.; the wire and the substrate) then the wire projection is incorrect or the wire is moving so fast that it hits the bottom of the melt pool, which in the real world is considered a failure. The code breaks at this point, giving an error message that there has been a collision. However, further calculations are written into the code for powder simulation, which ideally involves collision. In such cases, if a particle does collide with a solid, the moving solid is backed up by half a time step, and the velocity is recalculated based on the coefficient of restitution of the material and averaging the mass. This calculation is used for a more realistic solid-to-solid collision, which causes movements such as bouncing and others.

c) Fluid movement

The third step is to process the motion of the fluid particles in the simulation. The fluid velocities are updated with the forces calculated with SPH smoothing. The fluid positions and indices are updated from the velocities. The movement part will be updated automatically in the *create voxel function* based on the updated positions.

d) Laser movement

Finally, the position of the laser beam is updated based on the user-defined speed of the laser and the time step.

6.3.10. Increment Time and Save Data

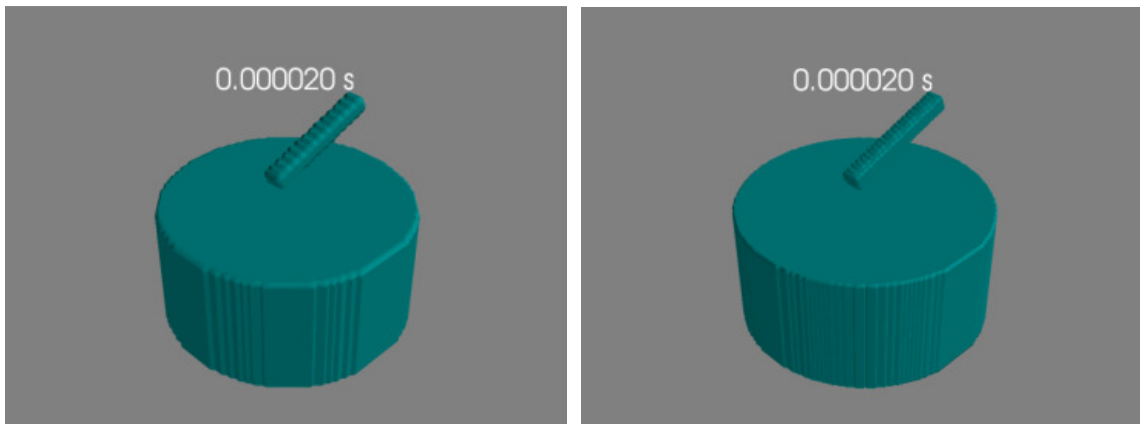
The final step in the iteration is to increment the simulation time by one time step and to repeat all of the above steps until the simulation time reaches the user-defined time. The results, including the simulation time, temperature, and phase arrays are saved into a data file at a predefined number of iterations. These data files are used to create the images that are assembled to form the simulation movie.

6.4. Results

Results from the simulation are plotted using visualization software such as Mayavi and Matplot. Tests are conducted for different input parameters, and the results are plotted.

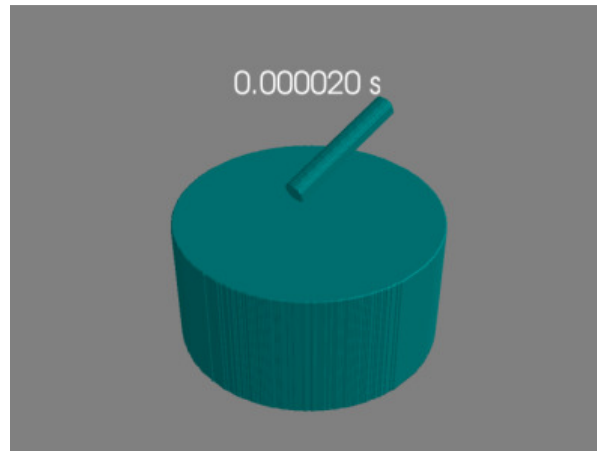
1) Resolution

Results are plotted with varying resolution values by keeping all other parameters constant. The results appear in Figure 6.3.



a) Resolution - 0.0001

b) Resolution – 0.00006



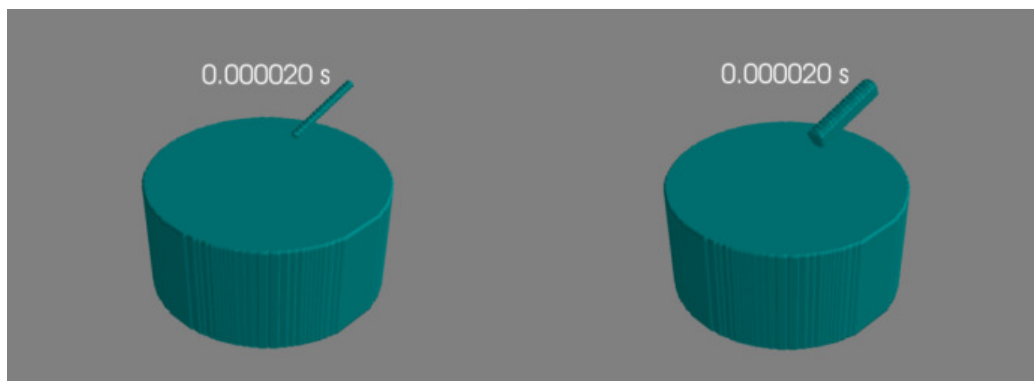
c) Resolution – 0.00003

Figure 6.3 Result under various resolutions

As shown in Figure 8.3, the lower the resolution, the more cells and the finer the mesh. However, lower resolution increases the computation time.

2) Wire Diameter

Results are plotted with varying wire diameters, as shown in Figure 8.4. The domain size is 1cm*1cm*1cm, with a resolution of 0.00006



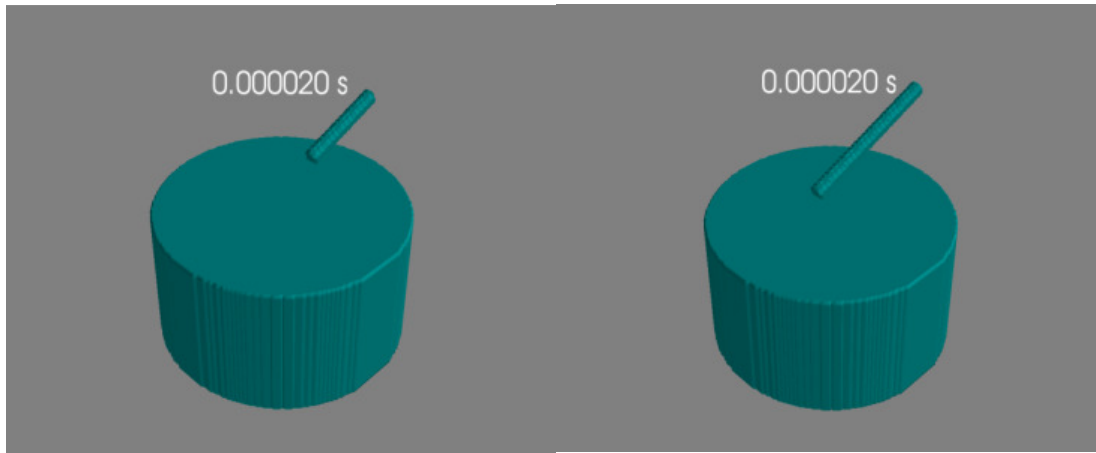
a) *Diameter – 1mm*

b) *Diameter – 3mm*

Figure 6.4 Result using various wire diameters

3) Wire Length

Images of varying wire lengths are shown in Figure 8.5. The domain size and resolution are the same as in the previous result.



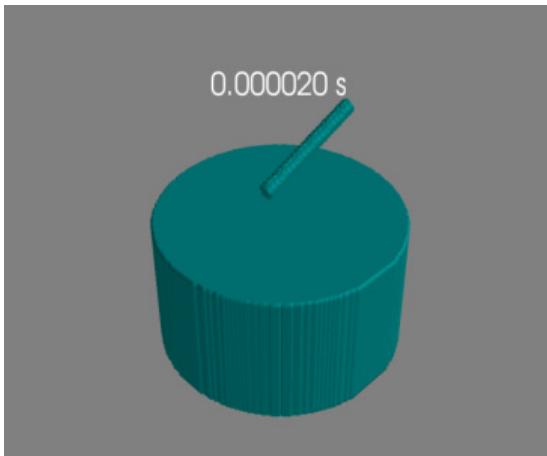
a) Length – 3mm

b) Length – 5mm

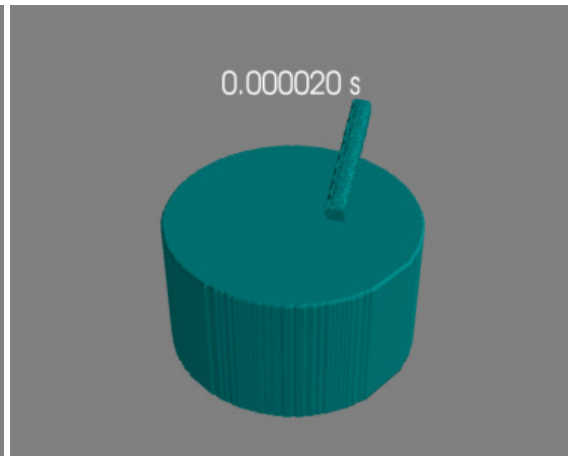
Figure 6.5 Result using various wire lengths

4) Wire Angles

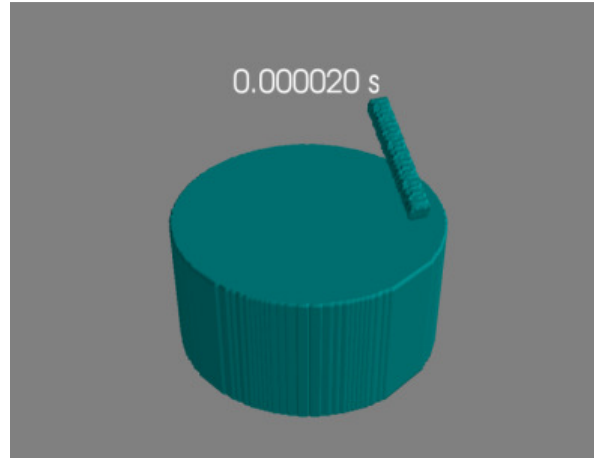
The wire angle can be varied in the X-Z plane and the X-Y plane. Results are plotted with different values of X-Z and X-Y angles in degrees. As shown in Figure 8.6, the wire can be rotated about a plane in a specified angle. There is separate input options for the X-Z plane and the X-Y plane angle of rotation.



a) X-Z – 70, X-Y – 0



b) X-Z – 70, X-Y - 30

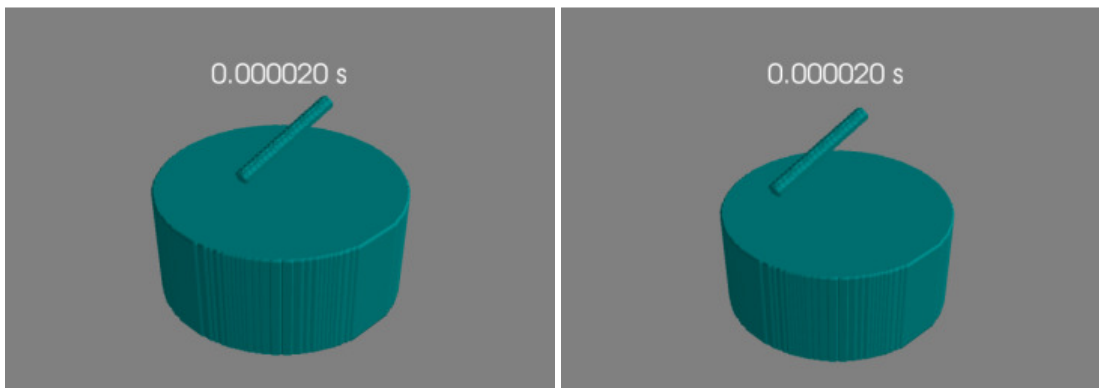


c) $X-Z - 70, X-Y - 60$

Figure 6.6 Result using various wire angles

5) Wire Offset

The offset is the dimension in the domain at which the wire is placed after it is created with the desired length, diameter, and angles. Results are plotted with different offset values. The offset from the domain at which the wire has to be placed can be specified. As shown in Figure 8.7 the offsets specified makes the wire appear in different location when the simulation starts. The figure is shows a 10mm, 10mm, 10mm size domain.



a) *Offset – 3mm, 5mm, 6mm*

b) *Offset – 5mm, 6mm, 8mm*

Figure 6.7 Result using various wire offsets

6.4.1. Temperature Plots Using Matplot

The temperature array is plotted using Matplot, as shown in 8.8.

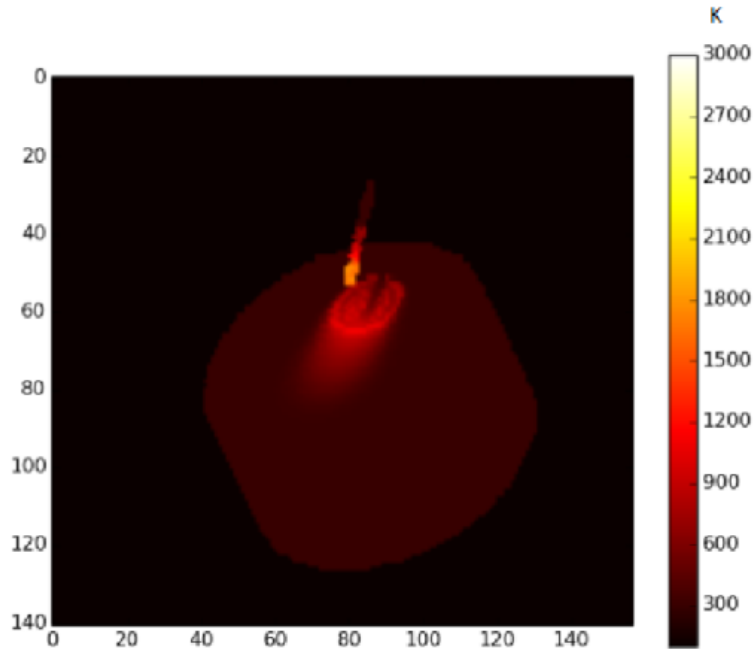


Figure 6.8 Temperature(K) plot using Matplot

In the figure, the X and Y axes represent the number of cells in the domain, and the color bar shows the temperature range and the color. The laser started from the center of the substrate and reached halfway to the end of the wire. The figure clearly shows the shadow of the wire falling on the substrate due to ray tracing. The wire is hotter than the substrate due to having less cross-sectional area.

6.4.2. Phase Plots Using Mayavi

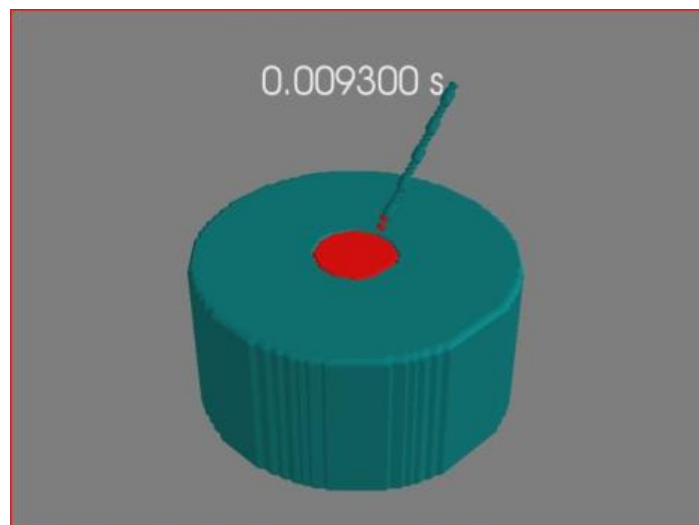


Figure 6.9 Phase plots showing melting

Figure 6.9 shows the phase plots with the melt pool formed. The title is the time of the simulation at which the image is plotted, 0.009300(sec). As shown in the figure, the tip of the wire is starting to melt and drip off from the wire to the melt pool.

6.5. Conclusion

Smoothed particle hydrodynamics has been shown to be one of the most efficient ways to numerically simulate problems involving multiphase flow and phase changes. Its computational efficiency and simple architecture makes it more robust and flexible than other simulations. The current simulation is a partial SPH model that considers fluid as SPH particles. A full SPH model would allow for more realistic calculations, such as the bending of the wire and other parameters. The technique could be integrated with CAD software in the future to easily create the solids and depositing parts of complicated geometries.

7. Numerical Analysis of Thermal Stress and Deformation in Multilayer Laser Metal Deposition Processes

7.1. Introduction

Highly localized heating and cooling during the Direct Metal Deposition (DMD) process produces nonuniform thermal expansion and contraction, resulting in a complicated distribution of residual stresses in the heat affected zone and unexpected distortion across the entire structure. The residual stresses may promote fractures and fatigue and induce unpredictable buckling during the service of deposited parts. The distortion is often detrimental to the dimensional accuracy of the structure; therefore, it is vital to predict the behavior of materials after the DMD process and optimize the design/manufacturing parameters to control the residual stresses and distortion. The focus of this research was to investigate both the thermal and mechanical behavior of the DMD process of Stainless Steel 304. Based on the finite element analysis package ABAQUS, a 3D, sequentially coupled, thermo-mechanical model was developed to simulate the transient temperature field, residual stress, and final deformation. A laser displacement sensor was used to record the deflection of the substrate caused by thermal stresses during the deposition process. By comparing the experimental results with the simulation results, the numerical model was validated.

7.2. Thermal Analysis

The numerical modeling consisted of two main steps. A transient thermal analysis first was carried out to generate the temperature history of the entire work piece, which then was used as input in the subsequent mechanical analysis.

7.2.1. Initial and Boundary Conditions, and Energy Distribution

The initial condition applied to the model was the ambient temperature, which was set as room temperature, 298.15 K. The boundary conditions, including thermal convection and radiation, were considered. A circular laser beam is shot onto the substrate vertically with a constant and uniform power density. Thus, the heat source term Q was considered a constant and uniformly distributed surface heat flux, defined as follows:

$$Q = \frac{\alpha P}{\pi r^2} \quad 7-1$$

where α is the absorption coefficient, P is the power of the continuous laser, and r is the radius of the laser beam. α was set as 0.4 according to numerous experimental results, and r was set as 1.25 mm.

7.2.2. Powder Addition

During modeling, the continuous powder addition process was divided into many small time steps. In each time step, using the “Model Change,” a set of elements was added onto the substrate to form rectangular deposits along the centerline of the substrate (Figure 7.1). The width of the deposits was assumed to be the same as the diameter of the laser beam, and the thickness of the cladding was calculated from the laser travel speed and powder feed rate with an efficiency of 0.3. The geometry of the deposits was updated at the end of each step to simulate the corresponding boundary conditions.

7.2.3. FEA Model

As shown in Figure 7.1, a finite element model for a 1-pass, 3-layer DMD process was built. Two cases were simulated with different process parameters, including laser power, laser travel speed, and powder feed rate, as shown in Table 7.1. These parameters were chosen according to the criterion that the final geometry of the deposits and the total energy absorbed by the specimen be the same in both cases.

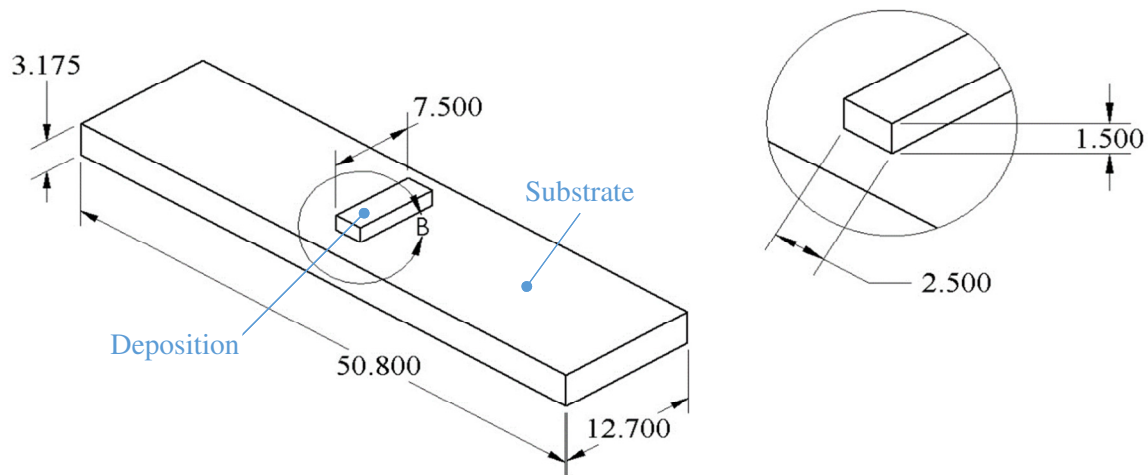


Figure 7.1 Dimensions of DMD specimen. The unit is millimeter.

Table 7.1 DMD process parameters

Case number	Laser power (W)	Laser travel speed (<i>mm/min</i>)	Powder feed rate (<i>g/min</i>)
1	607	250	6.3
2	910	375	9.4

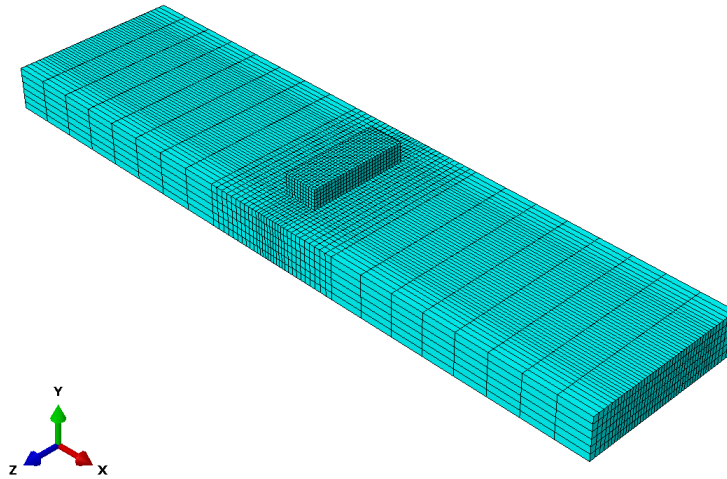


Figure 7.2 Meshing scheme

7.2.4. Numerical Temperature Field

Figure 7.7.3 shows the temperature field of the melt pool and the surrounding areas at different times in Case 1. The peak temperature during the process was 2500 K, while the simultaneous lowest temperature was close to room temperature. Considering the large temperature differences and small geometrical dimensions, very large temperature gradients would exist in the DMD process.

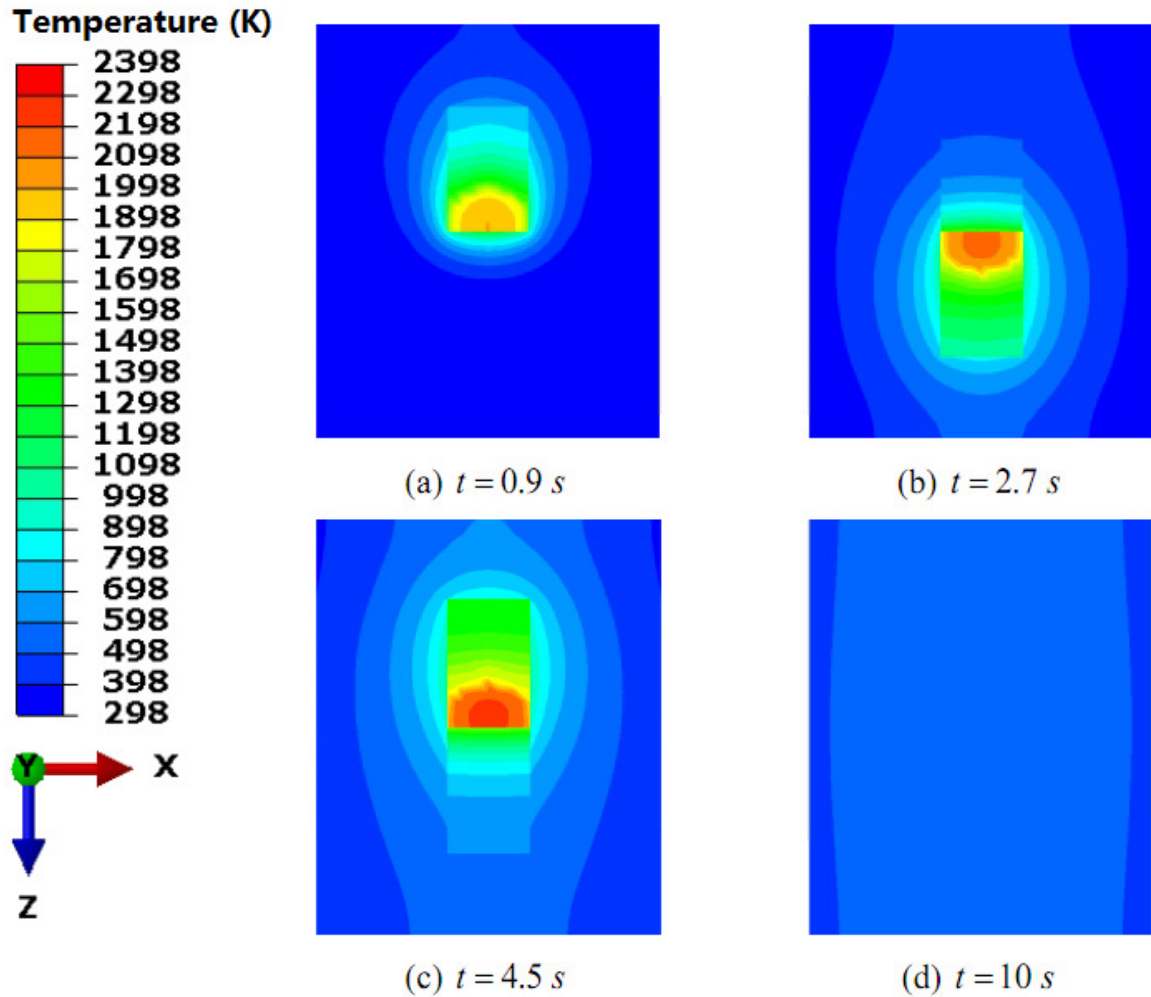


Figure 7.7.4 Contour plots of temperature field at different times (Case 1)

Figure 7.5 shows the temperature of the nodes in the x (length) and y (height) directions in Case 1 at $t = 2.7 \text{ s}$. The x-direction nodes were selected on the top surface of the substrate, while the y-direction nodes were selected along the height of the deposits. The top surface of the substrate had a maximum temperature of 1110 K right below the center of the laser beam, and the temperature decreased gradually along the x direction. In the y direction, the deposits had a maximum temperature of 2248 K on the top surface, and the temperature decreased rapidly to 1110 K. The slopes of the temperature curves clearly represent the thermal gradients in the x and y directions. In the x direction, the temperature gradient had a maximum value of 450 K/mm; in the y direction, the maximum temperature gradient occurred near the top surface of the deposits and was as large as 1400 K/mm before decreasing along the negative y direction. These steep thermal gradients would induce large compressive strains within the deposits and substrates.

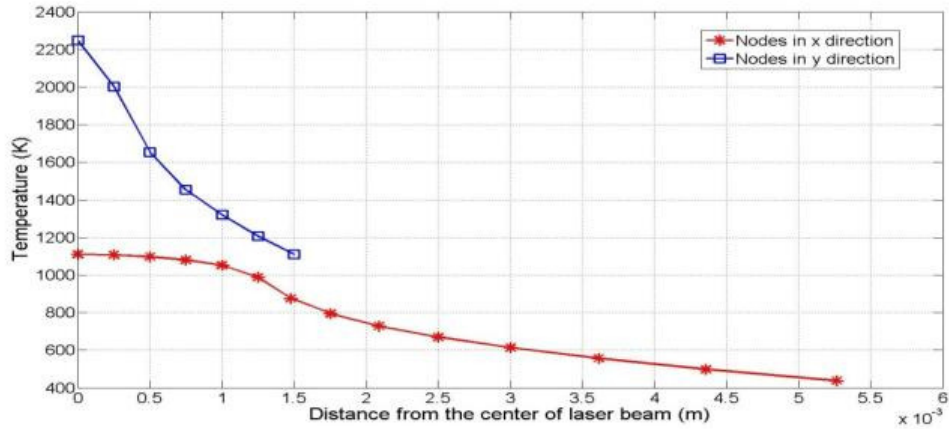


Figure 7.5 Temperature of nodes in x and y direction in Case 1 at t = 2.7 s

7.3. Residual Stress

The residual stress distribution within the final deposits appears in

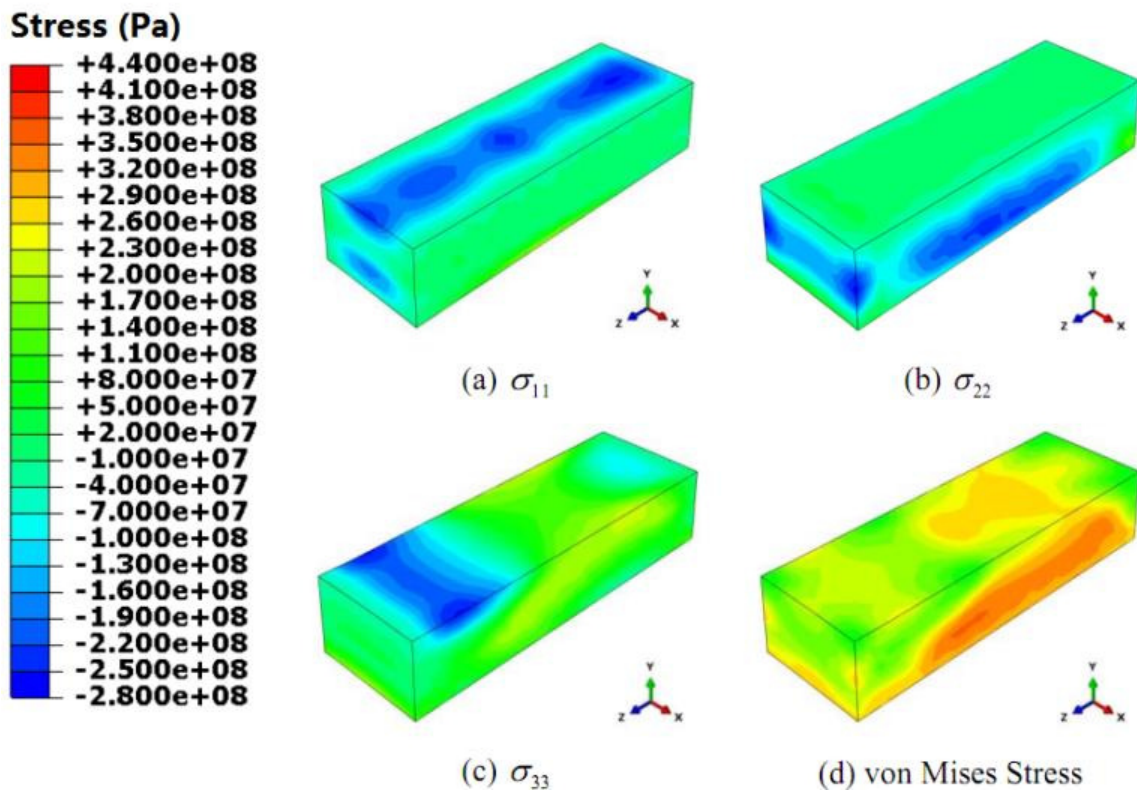
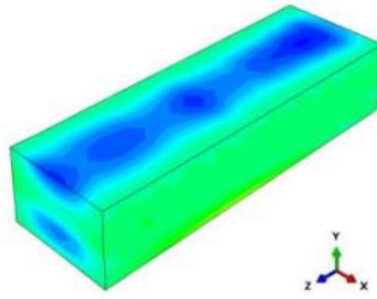
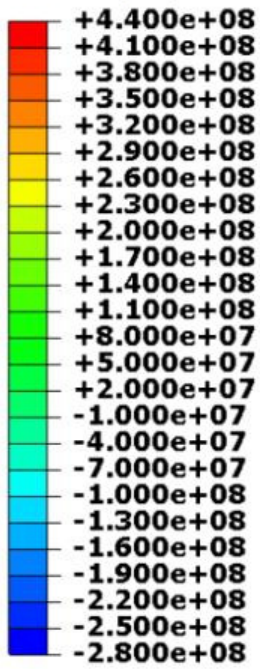
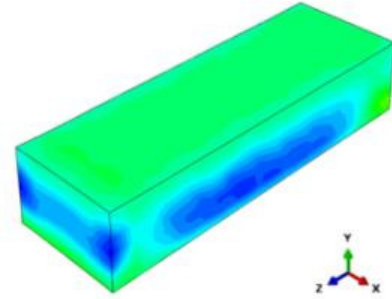


Figure 7.6 (one-quarter of the deposits are hidden to show the internal residual stress). Normal stresses σ_{11} , σ_{22} , σ_{33} along three spatial directions appear in

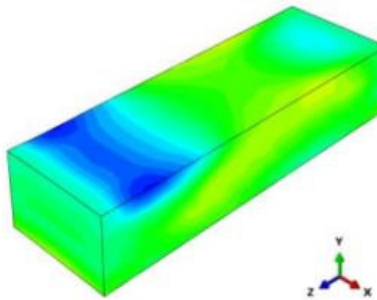
Stress (Pa)



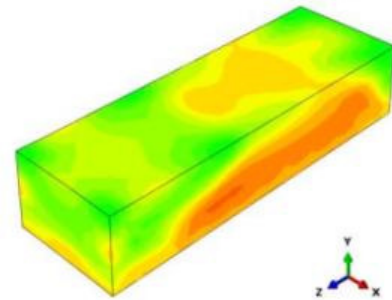
(a) σ_{11}



(b) σ_{22}



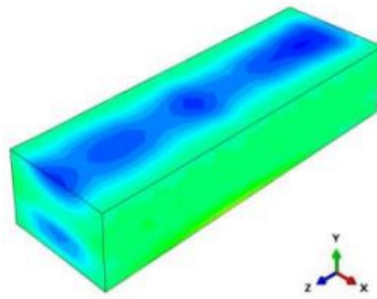
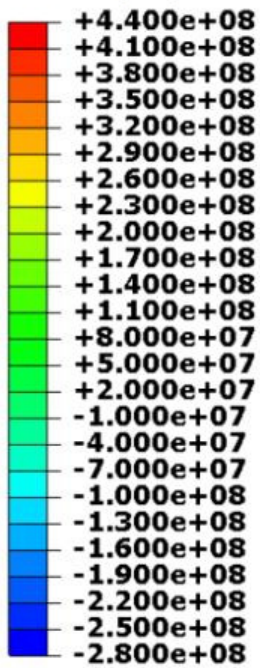
(c) σ_{33}



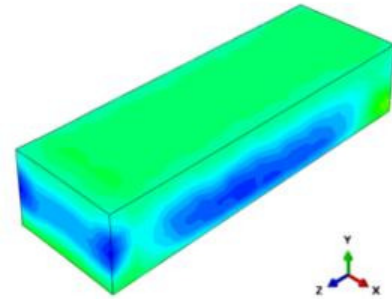
(d) von Mises Stress

Figure 7.6(a) through

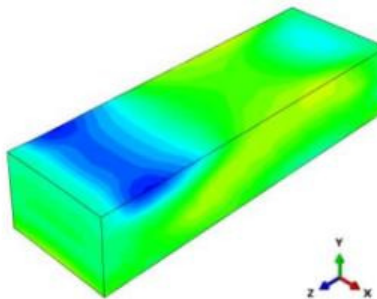
Stress (Pa)



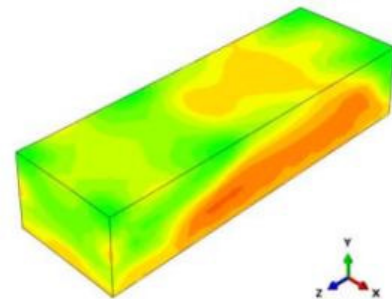
(a) σ_{11}



(b) σ_{22}



(c) σ_{33}



(d) von Mises Stress

Figure 7.6(c), respectively, and the von Mises stress is shown in

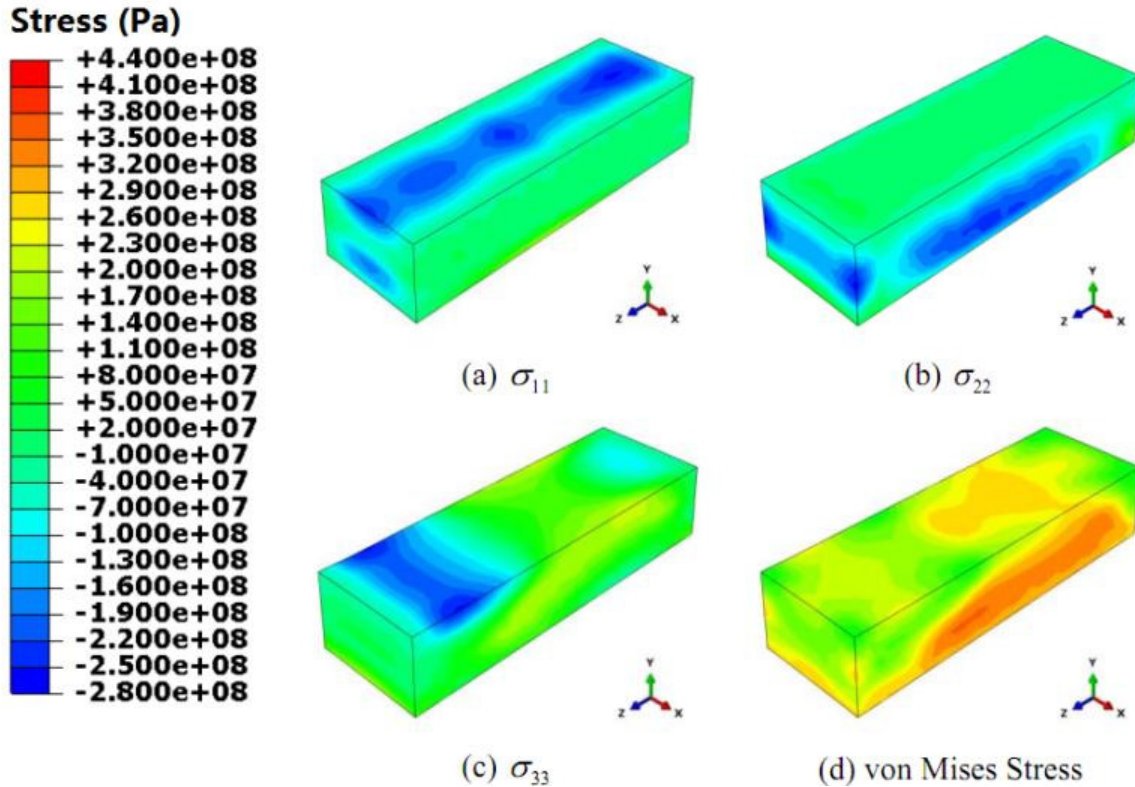


Figure 7.6(d). The figures show that compressive residual stress existed in the top free surface of the deposits, which was caused by the steep temperature gradient. As Figure 7.5 indicates, the temperature gradient in the x and y directions reached as high as 450 K/mm and 1400 K/mm, respectively. The expansion of the hotter top layer was inhibited by underlying material, thus introducing compressive stress in the top surface. Residual stresses in the lower part of the deposits were mostly tensile stresses due to the cool-down phase of the molten layers. After the deposition was finished and the laser was turned off, the remelted lower part of the deposits began to shrink, and this shrinkage was restricted by the underlying material, thus inducing tensile stresses.

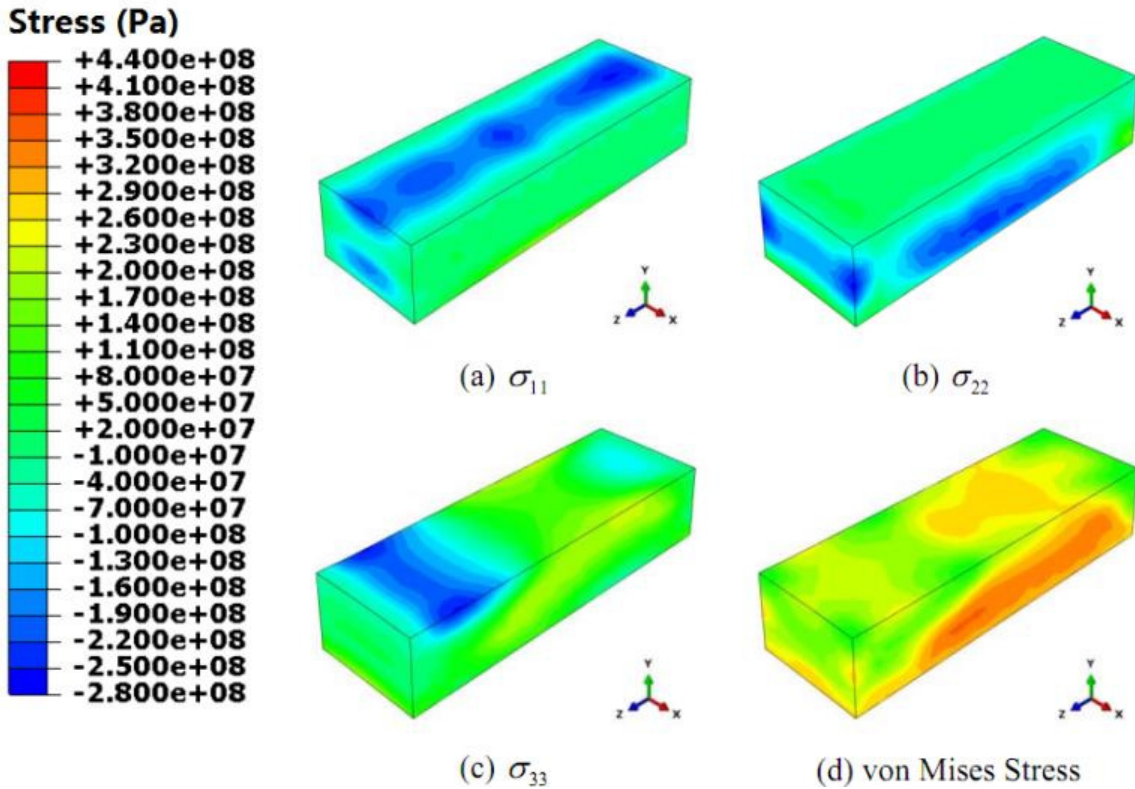
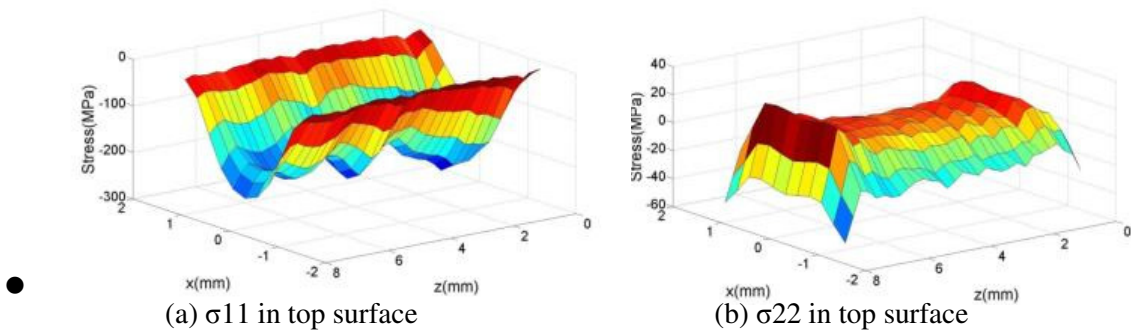
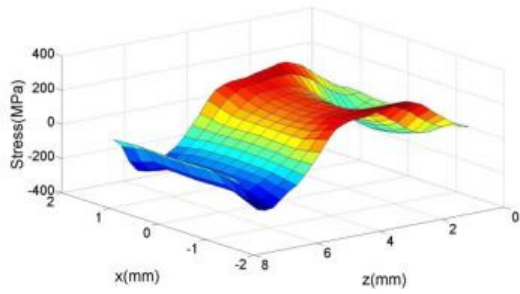


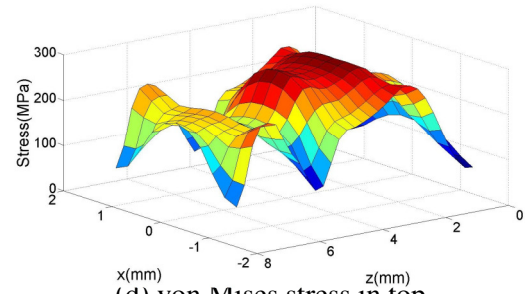
Figure 7.6 Contour plots of residual stress field within deposits

The distribution and magnitude of the residual stresses in the top surface of the deposits appear in Figure 7.7. In the x direction, the middle part of the top surface was compressed with a stress magnitude of approximately 200 MPa, while the two edges along the z direction were slightly tensioned. In the y direction, the residual stresses almost vanished. For the normal stresses along the z direction, tensile stresses with magnitudes of approximately 100 MPa existed near the center, and compressive stresses ranging from 0 to 200 MPa existed near both ends.





(c) σ_{33} in top surface



(d) von Mises stress in top surface

surface

Figure 7.7 Residual stress in top surface of deposits

7.4. Deformation

During the DMD process, the substrate will continuously experience expansion and shrinkage, ultimately maintaining a deformed shape. In this research, deflection in the y direction was the main deformation under consideration and was observed in both the experiments and simulations.

7.4.1. Experimental Setup

As shown in Figure 7.8, in the experiment, the substrate was clamped at the left end to prevent rigid body motion. A Keyence's LK-G5000 series laser displacement sensor with the accuracy of 0.25 micro shown in Figure 7.9, was placed directly below the right end of the substrate to record the displacement of the free end in the y direction with a frequency of 25 Hz during the process. The experimental results appear in Figure 7.10.

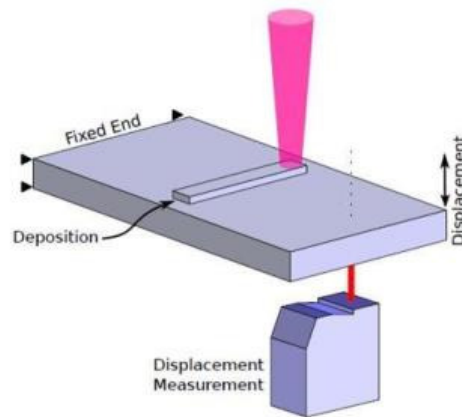
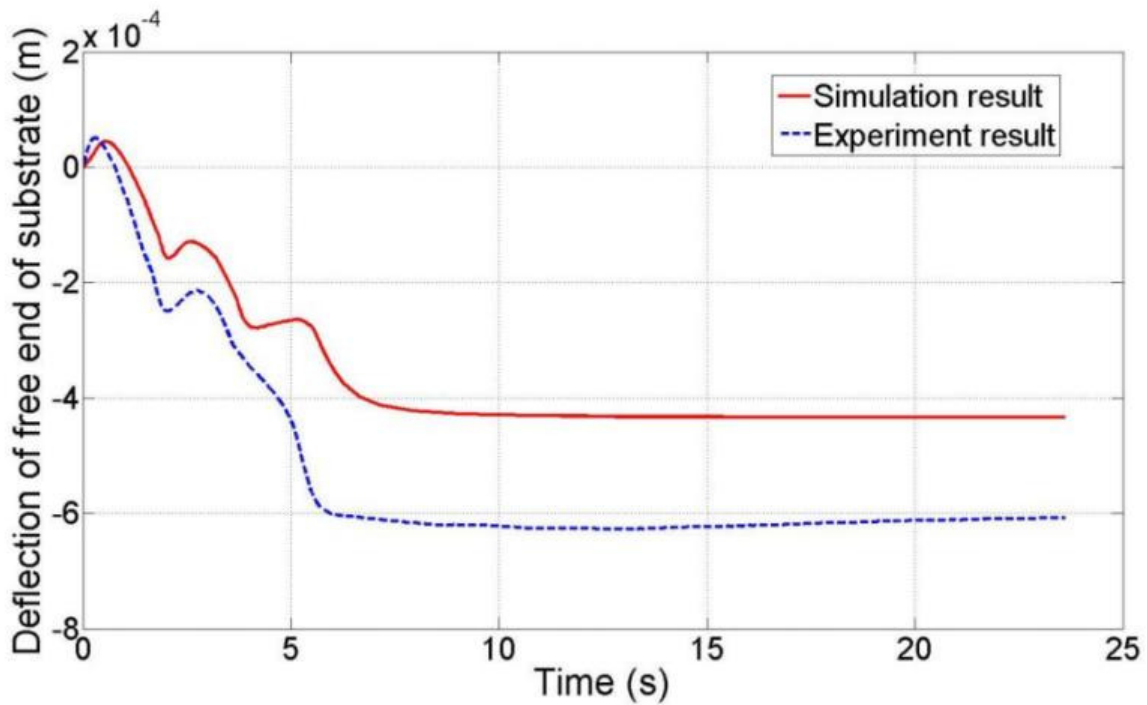


Figure 7.8 Experimental setup for measuring displacement during deposition

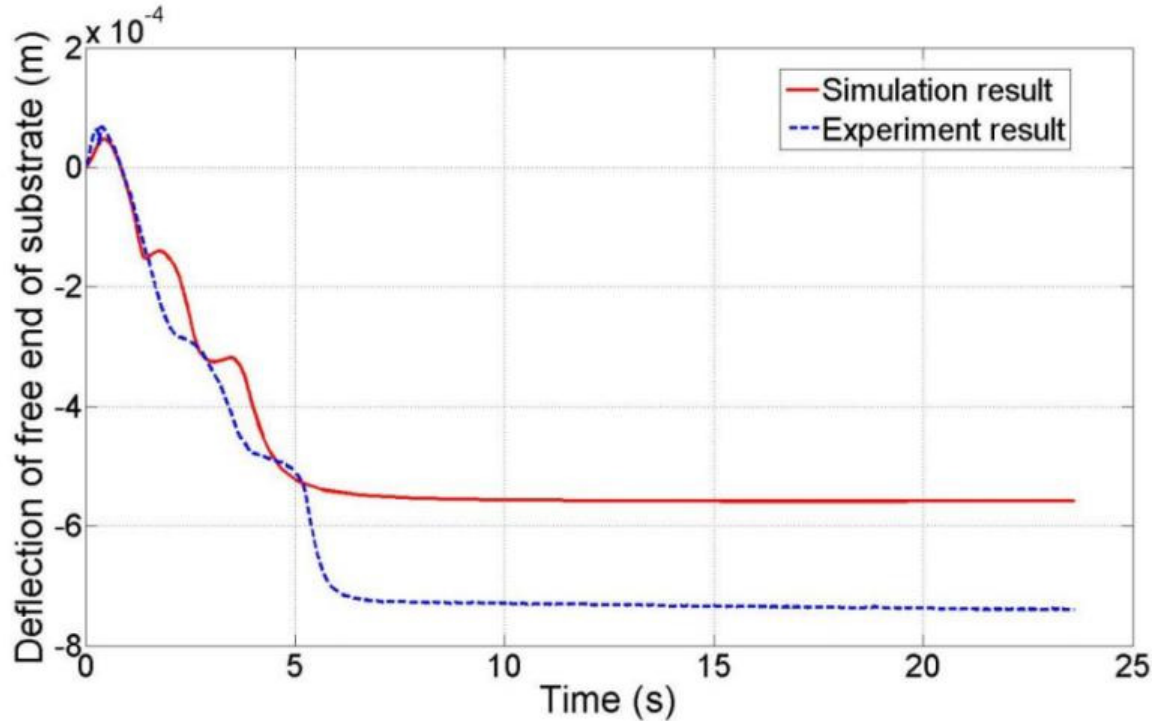


Figure 7.9 Laser displacement sensor

Figure 7.10 shows the comparison of the deflection of the substrate between the experimental and simulation results for both cases. These plots indicate that the trend of the deflection calculated from the simulation matched very well with the experimental results. For each deposition layer, the substrate first bent down due to thermal expansion on the top surface and then bent up due to thermal shrinkage during the cooling process. After completely cooling down, the substrate maintained the deformed shape.



(a) Deflection in Case 1



(b) Deflection in Case 2
Figure 7.10 Simulation and experimental results of deflection of substrate

The differences in the final deflection value between the simulation and the experiment were 28.5% and 24.6% for Case 1 and 2, respectively. Several possible reasons could exist for these differences. First, errors existed in experiment setup. In the simulation, the laser beam traveled exactly along the centerline of the substrate. However, this could not be accomplished perfectly in the experiments. These offsets would affect the deflection to a large extent because the deflection is sensitive to the position of the heated zone and measuring point. Secondly, the laser displacement sensor does not track the displacement of one particular node. Rather, it works by sensing the signal reflected by the obstacle, so the positions it monitors are always changing as the substrate continues to deform. The simplifications and assumptions considered in both the thermal and mechanical analysis are also important factors contributing to the differences.

7.5. Conclusion

A sequentially coupled, thermo-mechanical, finite element model was developed and validated experimentally. The results showed the temperature distribution, residual stress, and deformation within the formed deposits and substrates. Finite element modeling can be used to effectively predict the resulting mechanical behavior of materials after Laser Aided Direct Metal Deposition processes. More efforts are needed to explore more complicated situations in industry and to optimize design/manufacturing parameters to control the residual stress and distortion.

8. Solidification Microstructure

8.1. Cellular Automaton (CA) - Finite Element (FE) Model Introduction

A predictive model based on a Cellular Automaton (CA) - Finite Element (FE) method [23] was developed to simulate microstructure evolution during metal solidification for a laser-based additive manufacturing process. The macroscopic FE calculation was designed to update the temperature field and simulate a high cooling rate. In the microscopic CA model, heterogeneous nucleation sites, preferential growth orientation, and dendritic grain growth kinetics were simulated. The CA model was able to show the entrapment of neighboring cells and the relationship between undercooling and the grain growth rate. The model predicted the dendritic grain size and morphological evolution during the solidification phase of the deposition process. The model parameters for the simulations were based on stainless steel 316(SS316) and Ti6Al4V. Figure 10.1 illustrates the design of the entire CA-FE model.

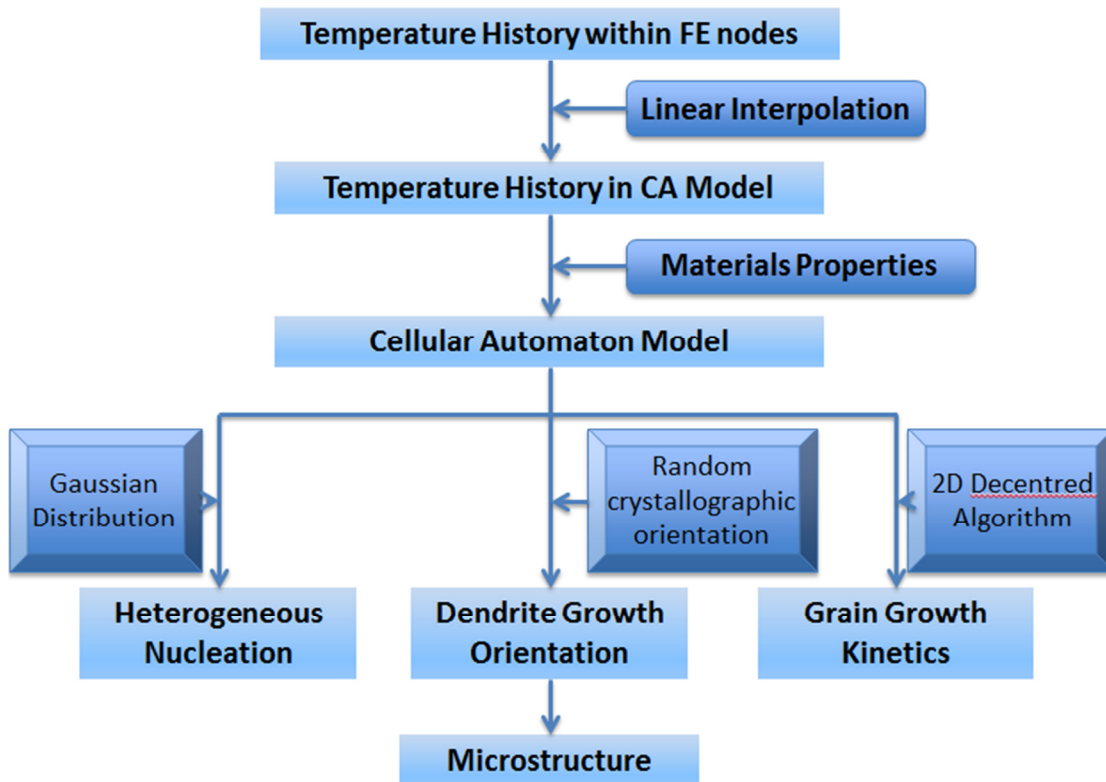


Figure 8.1 Flow chart of CA-FE model

Heterogeneous nucleation occurs nearly instantaneously at a characteristic undercooling. The locations and crystallographic orientation of the new nuclei are randomly chosen at the surface or in the liquid. The continuous nucleation distribution $dn/d\Delta T'$, which characterizes the relationship between undercooling and the grain density, is described by a Gaussian distribution both at the solid-liquid interface and in the bulk liquid (Eq. (8-1)). The parameters of these two distributions, including the maximum nucleation density n_{max} , the mean undercooling ΔT_N , and the standard deviation of the grain density distribution ΔT_σ , can be obtained from experiments and grain size measurements. [24]

$$n(\Delta T) = \int_0^{\Delta T} \frac{dn}{d\Delta T'} d\Delta T' = \int_0^{\Delta T} \frac{n_{max}}{\Delta T_\sigma \sqrt{2\pi}} \exp\left[-\frac{1}{2}\left(\frac{\Delta T' - \Delta T_N}{\Delta T_\sigma}\right)^2\right] d\Delta T' \quad (8-1)$$

Undercooling is the most important factor in the columnar and dendrite growth rate and grain size. The total undercooling of the dendritic tip consists of three parts, solute undercooling, thermal undercooling, and curvature undercooling. For most metallic alloys, the kinetic undercooling for atom attachment is small, so it is neglected [25]. The total undercooling can be calculated as follows:

$$\Delta T = mC_0[1 - A(P_c)] + \theta_t I(P_t) + \frac{2\Gamma}{R} \quad (8-2)$$

where m is the liquidus slope; Γ is the Gibbs-Thomson coefficient; C_0 is the solute concentration in the liquid far from the solid-liquid interface; P_t and P_c are the thermal and solutal Peclet numbers, respectively; k is the solute partition coefficient at the solid-liquid interface; $A(P_c)$ equals $[1 - (1 - k)I(P_c)]^{-1}$; θ_t is the unit thermal undercooling ($= \Delta h_f/c$); and R is the radius of the dendritic tip.

For the laser deposition process, the rapid solidification condition corresponds to a high Peclet number at which the dendritic tip radius is given by (Eq. (8-3)):

$$R = \left[\frac{\Gamma}{\sigma^*(mG_c^* - G^*)} \right]^{1/2} \quad (8-3)$$

where σ^* , the marginal stability constant, approximately equals $1/4\pi^2$ [26], and G^* and G_c^* are the effective temperature gradient and concentration gradient, respectively.

8.2. Thermal History and Grain Morphology Model Result During Laser Remelting Process

In this part of the experiment, no material was added on the substrate. The thermal history and grain morphology model in the molten pool domain during the laser remelting process appear in Figure 8.2 and Figure 8.3. Because the CA model requires a much finer grid than the FE temperature model, interpolation is necessary to obtain finer temperature information. The CA model domain corresponds to the black rectangle in Figure 8.2

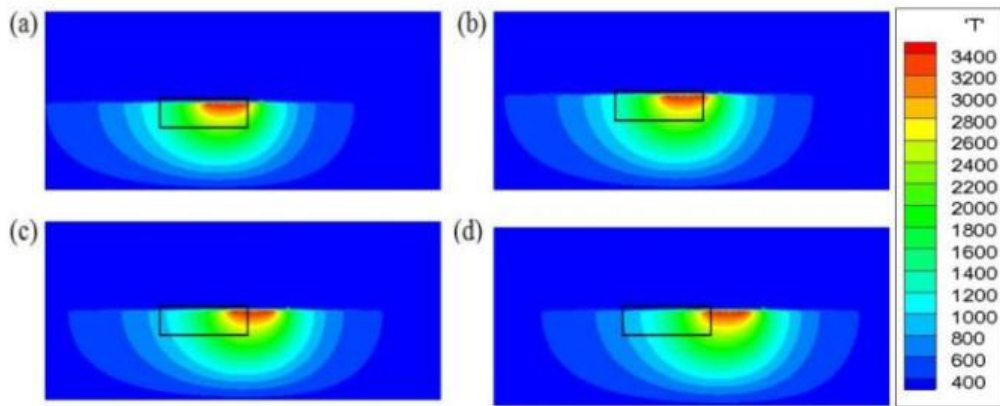


Figure 8.2 Macroscopic FE simulated temperature field for laser remelting process on SS316. Temperatures are in K and shown at a) $t=105\text{ms}$, b) $t=120\text{ms}$, c) $t=135\text{ms}$, and d) $t=150\text{ms}$. The black rectangle indicates the section of thermal results used for the CA microscopic model. The rectangle is $200\ \mu\text{m}$ wide and $70\ \mu\text{m}$ high.

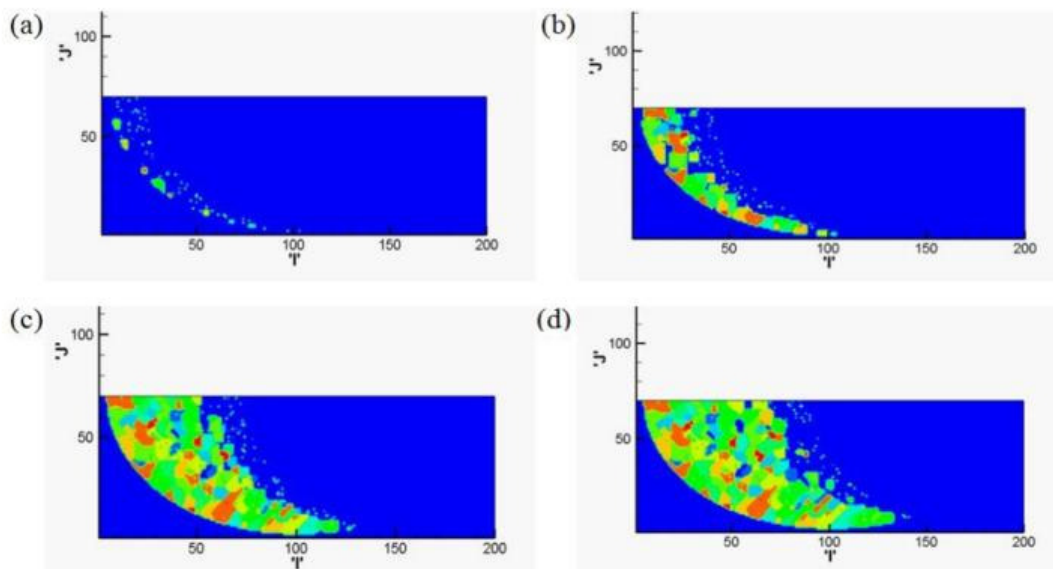


Figure 8.3 Microscopic CA simulation evolution of SS316 microstructure during solidification. Microstructure evolution is shown at a) $t=105\text{ms}$, b) $t=120\text{ms}$, c) $t=135\text{ms}$, and d) $t=150\text{ms}$. The 'I' and 'J' axes are the number of $2\ \mu\text{m}$ grid in the microscopic model, depicting the grain lengths in two dimensions. Color indicates individual grains.

Figure 8.3 indicates that equiaxed grains dominated the molten pool and shows the evolution of the solidification microstructure during the laser deposition process of SS316. The grid size for the macroscopic model was $10\mu\text{m}$, and the macro time step was 10^{-4}s . The grid size for the microscopic model was $2\mu\text{m}$, and the micro time step was $2 \times 10^{-5}\text{s}$. As Figure 8.3 illustrates, the grains initially nucleated at the interface between the solid and liquid because the heat transfer at the interface occurred much faster than in the liquid. The different colors represent different crystallographic orientations of grains. Also, during grain growth, the grains always maintained their original orientations, which agreed with the physical mechanism.

8.3. Solidification Grain Morphology Modeling Under Laser Deposition.

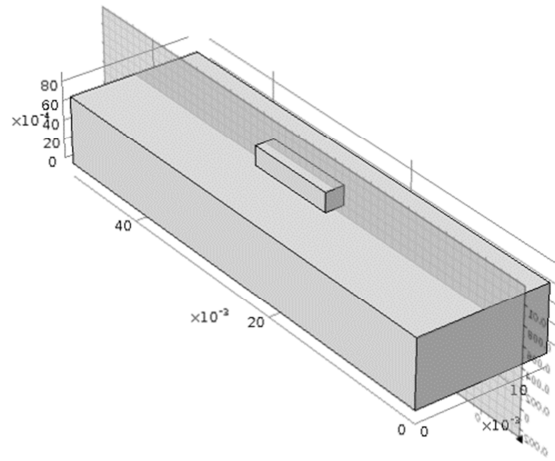
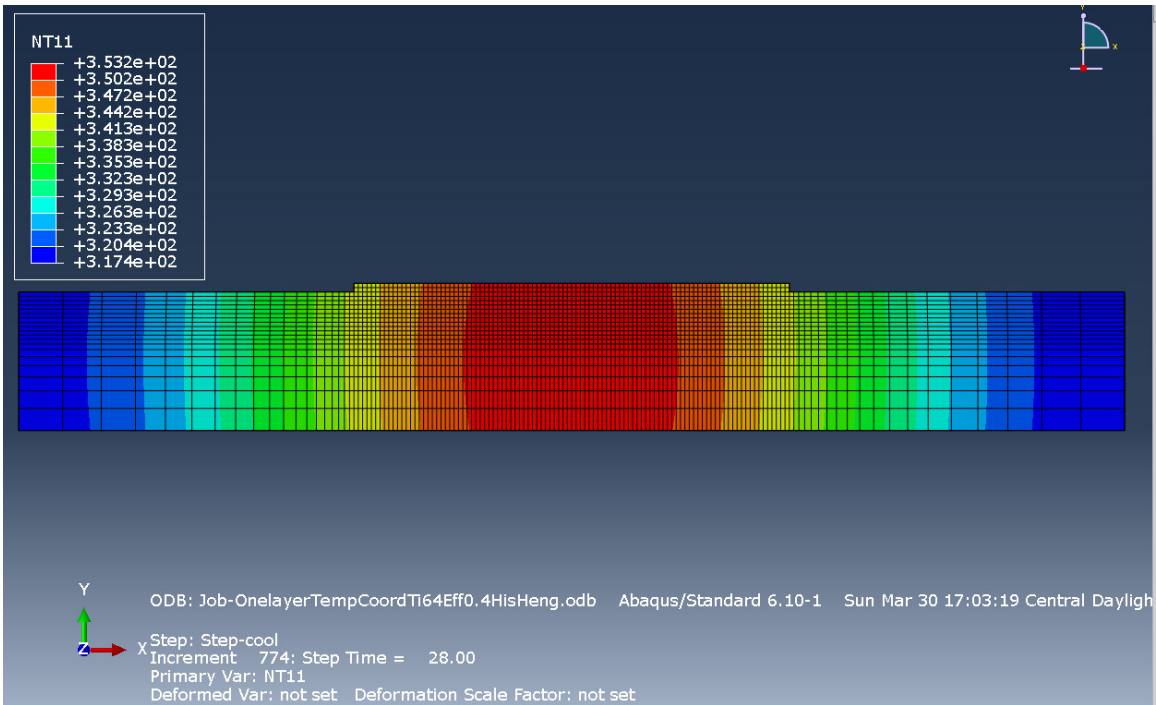
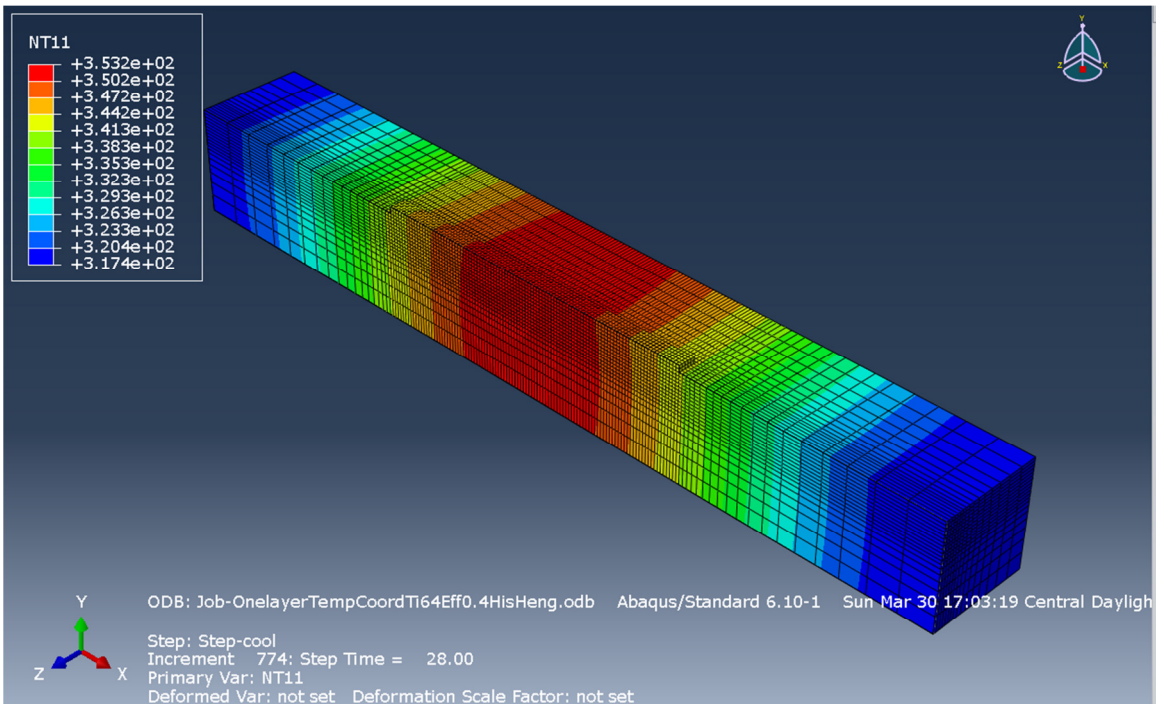


Figure 8.4 Sample and cutting position scheme



(a) Front view



(b) Iso view

Figure 8.5 Simulated temperature distribution during single-layer laser deposition process

Figure 8.4 indicates the position of the deposition area on the substrate and the observation cross section. ABAQUS was used to simulate the temperature field of the substrate and deposited

material, including the deposition materials added on the substrate when the laser moved forward. A Fortran subroutine was written to simulate the moving laser's heat source. The laser deposition of single layer Ti6Al4V was conducted with the power of 750W, scanning speed of 600mm/min and powder delivery of 12g/min. The deposited material was added by activating elements in the deposition domain in a stepwise manner. The deposition temperature field and grain morphology were simulated first only in one layer. Figure 8.5 indicates the temperature field of the substrate and deposited material.

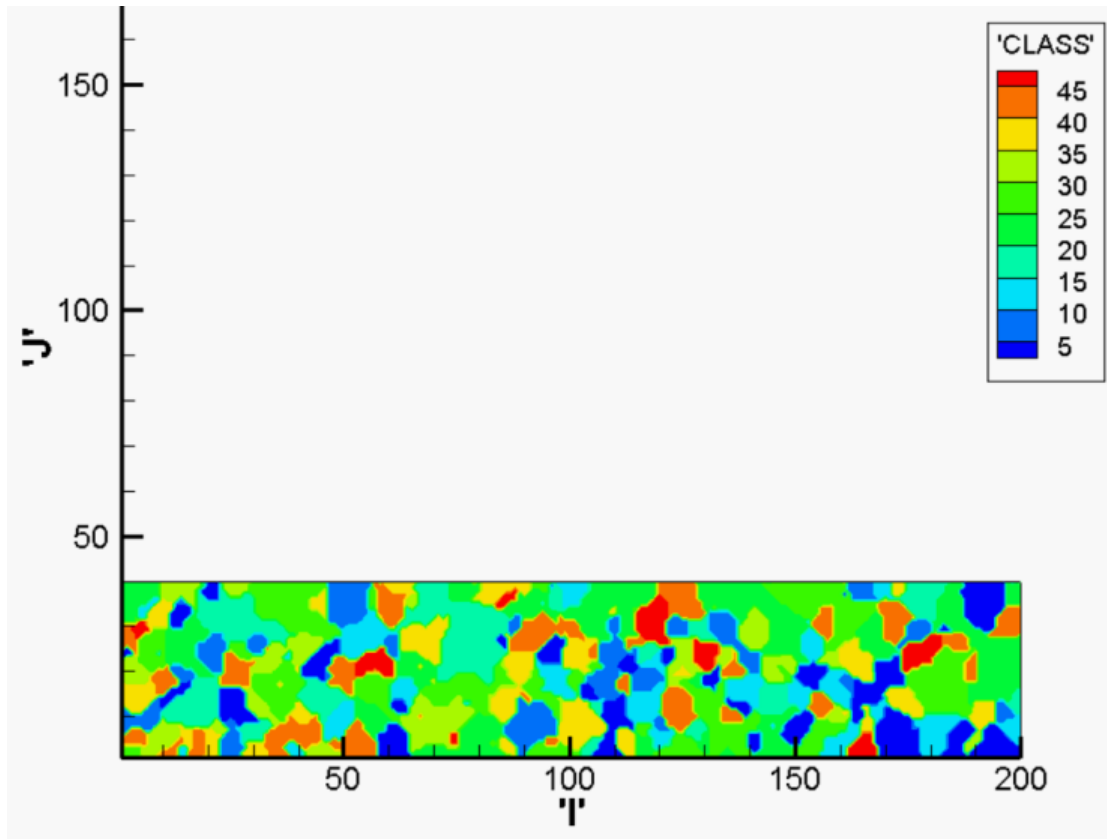
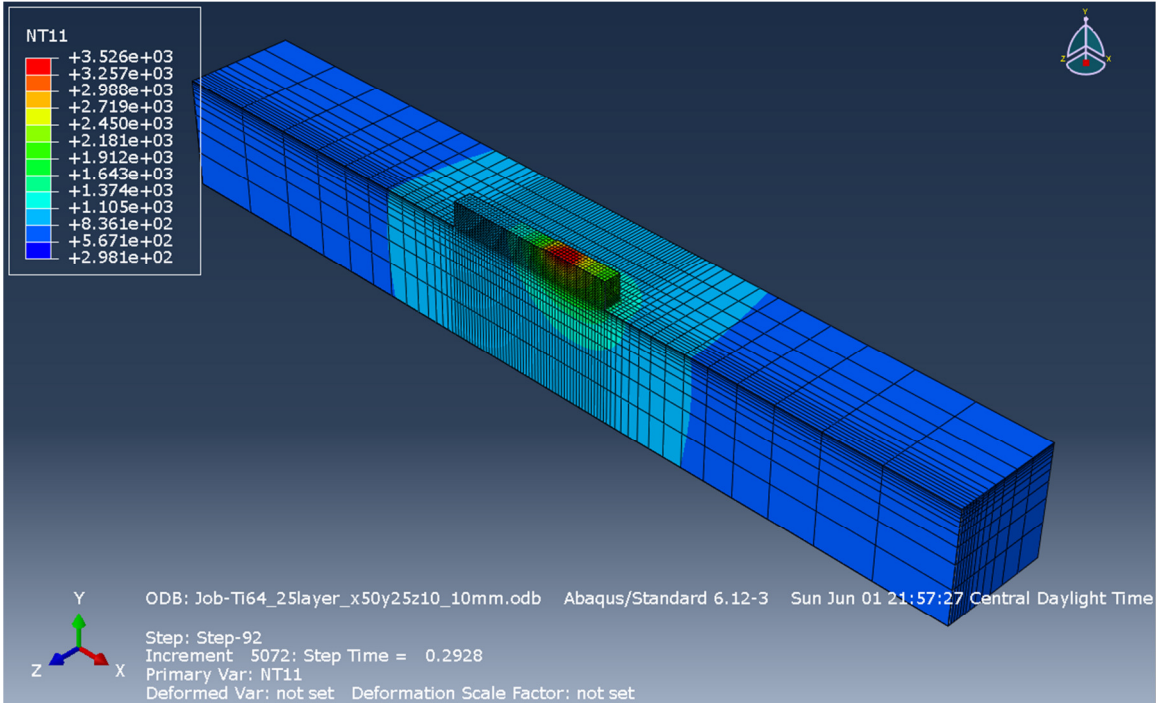


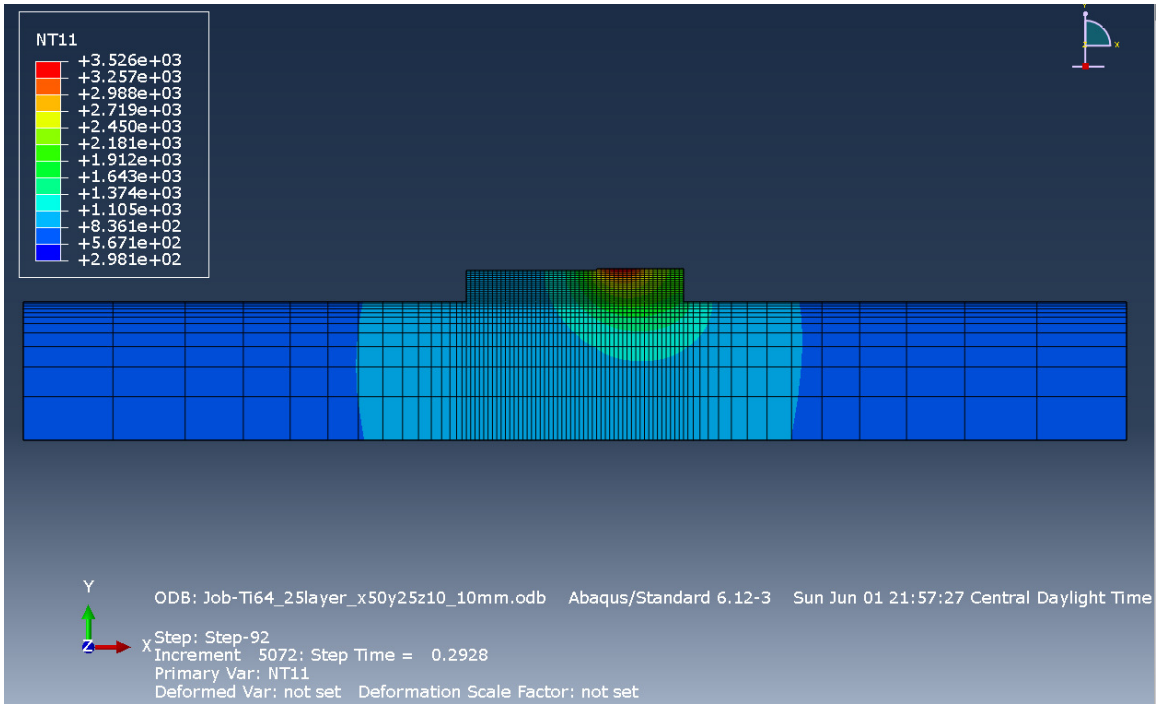
Figure 8.6 Grain morphology simulation of single-layer deposition of Ti6Al4V. In the legend, 'CLASS' represents orientations of different grains.

Figure 8.6 indicates that grain morphology simulation of single-layer deposition of Ti6Al4V. The domain size in the CA model was $2\text{mm} \times 0.4\text{mm}$, and the simulation time was 100ms. The 'I' and 'J' axes indicate the numbers of CA cells along the horizontal and vertical directions. The original temperature nodes obtained from ABAQUS were linearly interpolated because the element size in ABAQUS was $200\mu\text{m}$. The size of each cell was $10\mu\text{m}$ in the CA model. Different colors indicate individual grains. The grain nucleation sites and growth rate were controlled by the temperature history obtained from the FEA model. For one-layer laser

deposition microstructure simulation, the grains were almost equiaxed. The grain size varied from $30\mu\text{m}$ to $150\mu\text{m}$. There are no columnar grains for one-layer laser deposition.



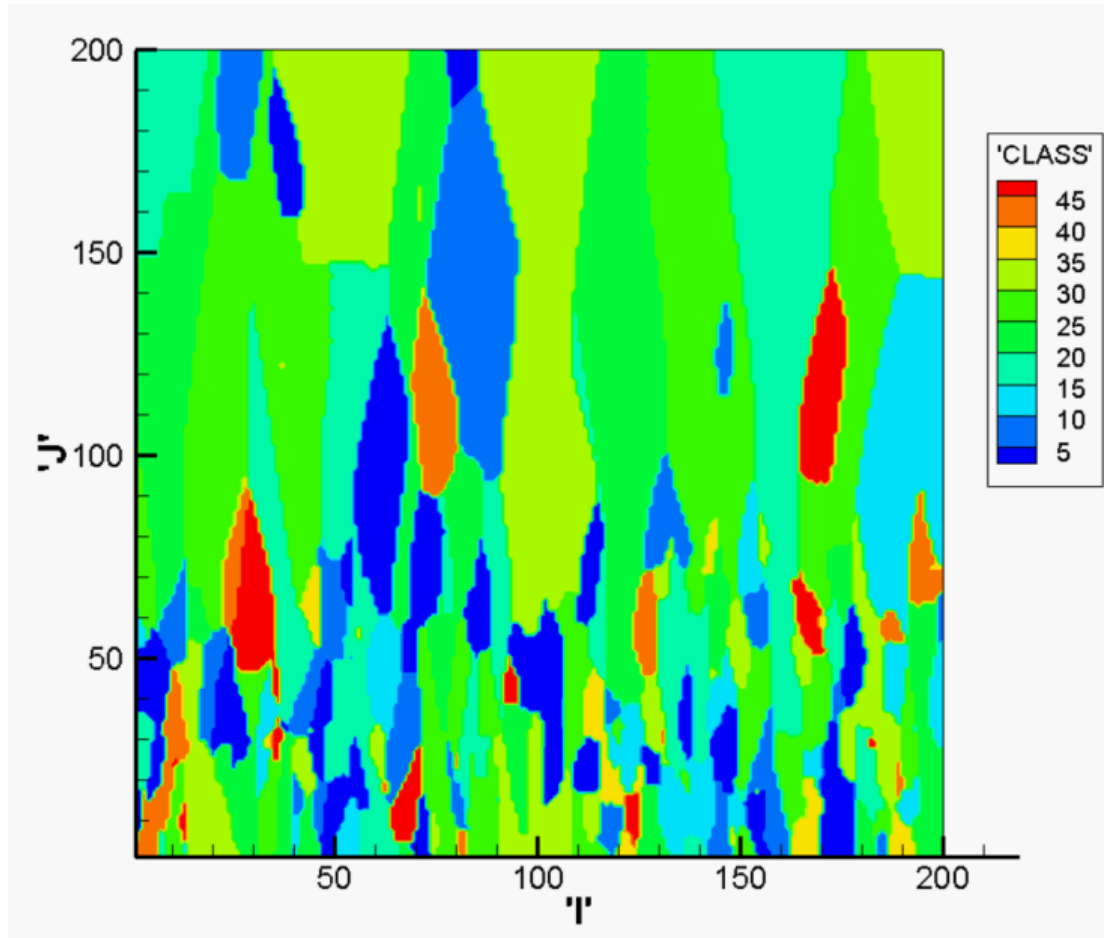
(a) Iso view



(b) Front view

Figure 8.7 Thermal history for 25-layer Ti6Al4V laser deposition

Figure 8.7 depicts the temperature field of the substrate and deposited material. ABAQUS was used to simulate the temperature field of the substrate and deposited material, including the 25-layer deposition materials added on the substrate when the laser moved forward and backward. The laser deposition of single layer Ti6Al4V was conducted with the power of 750W, scanning speed of 200mm/min and powder delivery of 2g/min.



8.8 Grain morphology modeling of 25-layer Ti6Al4V laser deposition

Figure 8.8 shows multiple layers of the Ti6Al4V grain morphology under the laser deposition process. When more layers were deposited, columnar grains began to dominate, while equiaxed grains began disappearing and became the minority. The orientations of the columnar grains were almost perpendicular to the laser motion's direction because the grains grew along thermal gradient direction. The domain size in the CA model was 2mm × 2mm. Based on this simulation result, the width of the columnar grains varied from 100μm to 600μm.

8.4. Comparison with experimental results in the related literature

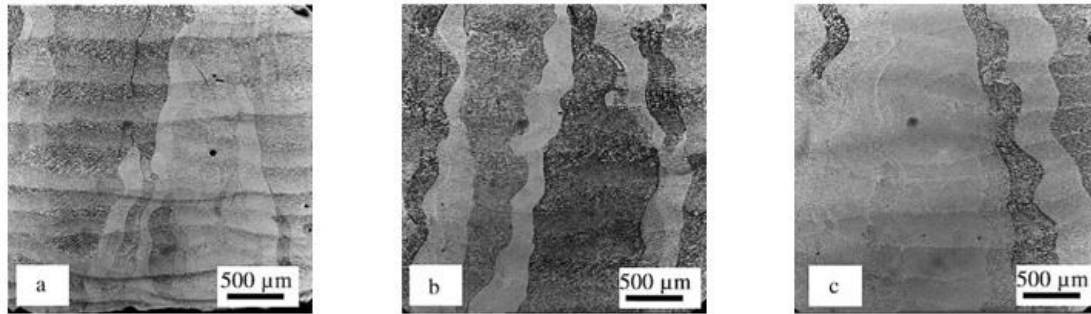


Figure 8.9 Optical morphologies of DLF samples obtained: (a–c) at the bottom, center, and top locations

Wu et al. [27] conducted a laser deposition experiment with a 1750-W CO₂ laser, showing the grain morphology results from using a range of laser powers, from 180 to 516W, and at a given scan speed of 300 mm/min, powder feed rate of 12 mm/min, and Z-increment of 0.3 mm. As shown in Figure 8.9, samples were fabricated at 264 W with a scan speed of 300 mm/min and powder feed rate of 12 g/min. The deposition height of each figure was 2.5mm. The total height of the deposition zone was 20mm. At the bottom, center, and top, the width of the columnar grains varied from 0.2 to 1 mm, 0.3 to 1.5 mm, and 0.2 to 4 mm, respectively. In the model, the columnar grain width varied from 100μm to 600μm within a 2mm × 2mm domain. In the literature, the columnar grain width varies from 200μm to 1mm within a 2.5mm × 2.5mm domain. The current grain morphology modeling result is in the same order of magnitude as optical morphologies.

8.5. Summary

During the solidification process, the grain nucleation and growth are intensely controlled by the cooling rate of substrate and deposited zone. The thermal history can be simulated by the finite element method, which integrates with the cellular automaton method to predict the grain morphology. Grain morphology simulation of single-layer deposition of Ti6Al4V indicates that equiaxed grains dominate in the deposited zone and no columnar grains can be found. Grain morphology modeling of 25-layer Ti6Al4V laser deposition indicates that while more layers were deposited, columnar grains began to dominate and equiaxed grains began disappearing and became the minority. The orientations of the columnar grains were almost perpendicular to the laser motion's direction. Compared to the similar studies in the literature, the multiple grain morphology modeling result is in the same order of magnitude as optical morphologies in the experiment.

In future work, the thermodynamic properties and parameters of compositions and phases, which can be obtained from a commercial database such as JmatPro, can be included to control grain nucleation and growth. This will improve the accuracy of the grain morphology simulation result.

9. Microstructure Observation and Simulation of Ti6Al4V Single-Wall Deposition

9.1. Introduction

The nature of α/β transformation in Ti alloys and the complex thermal history in the laser deposition process causes some special morphology and microstructure features to appear in the deposits.

Different Ti alloy microstructures are characterized by the size, shape, and distribution of two phases, α (hcp, below β -transus) and β (bcc). β transforms into various products in the α/β region. The microstructures appearing in LMD include colony α , plate-like α , grain boundary α , Widmanstätten α , and martensite α' . The latter is produced upon rapid cooling (>16.7 K/s [28], >410 K/s [29]) above the martensite start temperature and can transform into a very fine lamellar α/β microstructure between 700-850 °C. An intermediate cooling rate produces Widmanstätten α , while a comparatively slow cooling rate results in colony α . The labels Widmanstätten α , basketweave α , and acicular are often used to refer to the same structure.

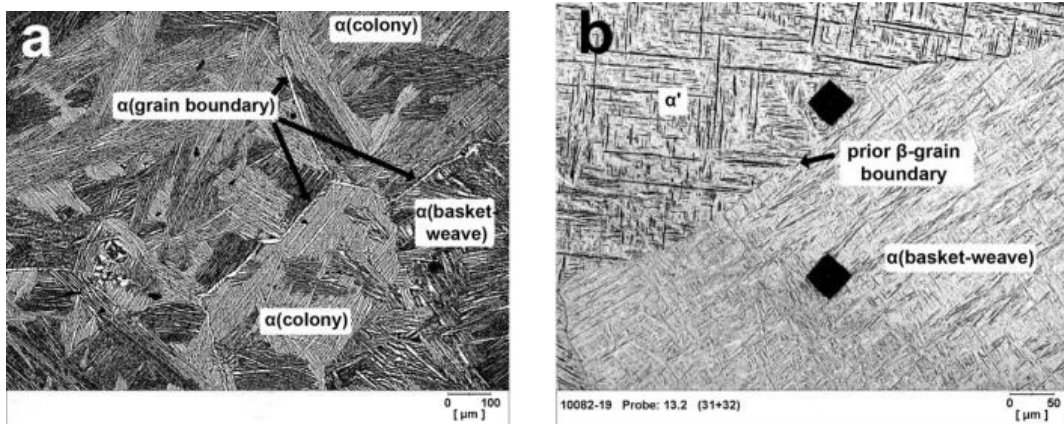


Figure 9.1 Various typical microstructures appearing in Ti alloy laser deposits [30].(a) shows colony, grain boundary and basketweave α ; (b) shows basketweave α , martensite α' and prior β -grain boundary

An obvious transformation trend exists from colony α and basketweave α to martensite α' as the cooling rate increases at β -transus. However, the critical transition rate is not clear. The relationship between the α -lath thickness, the size of colony α , the microstructure percentage, and the cooling rate and other temperature information is the key to predicting the microstructure in laser deposits.

9.2. Experiment

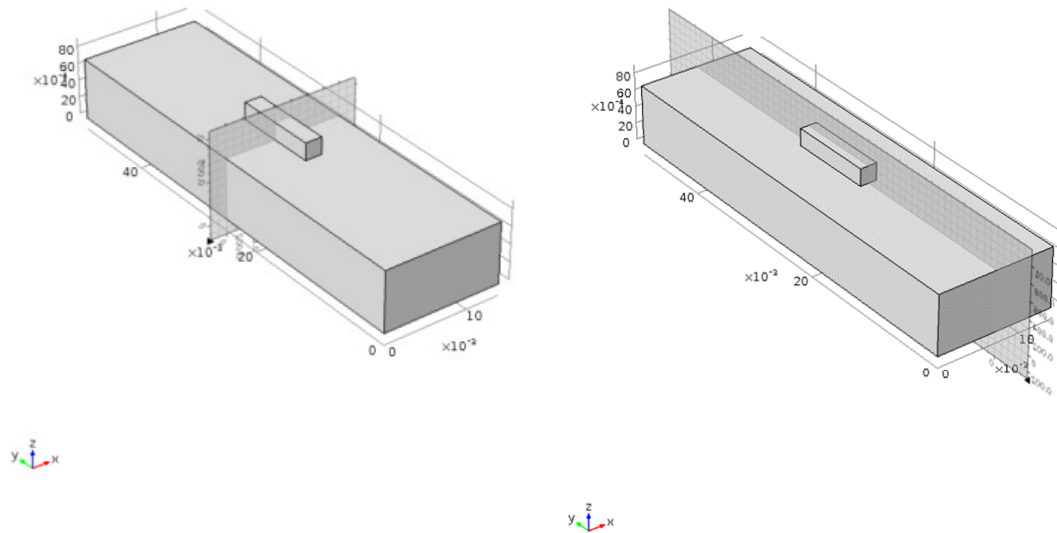
To study the evolution of the microstructure during the laser metal deposition process, a deposition experiment was conducted using a diode laser (Nuvonyx ISL-1000M, 808nm) with a maximum power of 1 kW. The laser radiation energy density was evenly distributed on a circle with a 2 mm diameter. The laser beam head, powder feeder nozzle, and substrate were fixed on a CNC machine to create the deposition path.

Thin walls were built according to the parameters listed in Table 9.1. The powder and substrate were both Ti6Al4V. The height of the deposit was 2 and 4.8 mm.

Table 9.1: Experimental parameters

Number of layers	Layer thickness (μm)	Laser power (W)	Scan speed (mm/min)	Scan length (mm)
25, 60	70-80	750	200	10

The deposits were cut through the middle cross section perpendicular to the direction in which the laser moved, and through the central cross section parallel with laser's direction, by wire electrical discharge machining (wire EDM), as shown in Figure 9.2. The specimens were mounted, ground, polished, and etched according to standard metallography methods. An optical microscope was used to observe the morphology.



(a) First cross section perpendicular to the laser's direction

(b) Second cross section parallel with laser's direction

Figure 9.2: Cross section position for optical microscope microstructure observation. (a) First cross section perpendicular to the laser moving direction; (b) Second cross section parallel with laser moving direction.

9.3. Simulation

The finite element analysis (FEA) thermal simulation was accomplished using Abaqus 6.13. The model parameters were the same as in the experimental setup, as shown in Table 9.1. The laser radiation was modeled as a moving heat flux condition via a user subroutine, and new material was added into the deposit via an activation/deactivation mechanism in Abaqus.

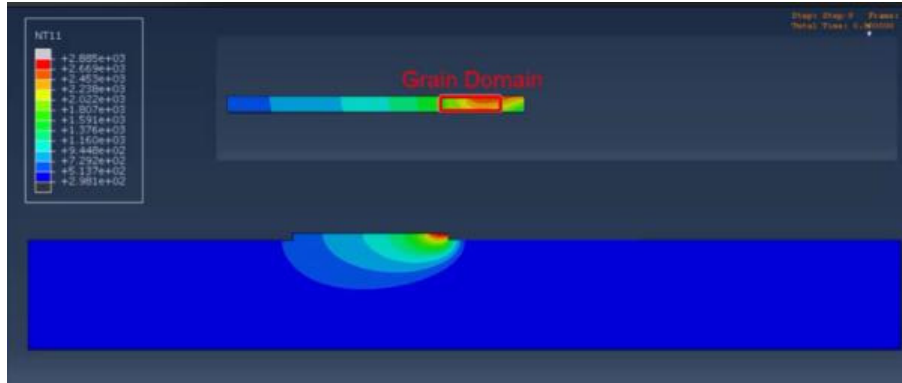
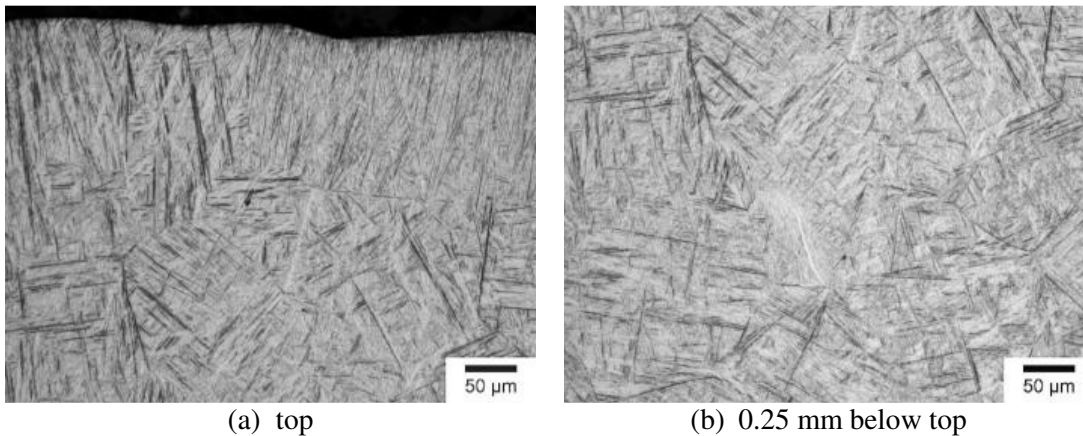


Figure 9.3: Simulated temperature distribution during 25 layers Ti6Al4V alloy deposition at the first layer.

Because of computer powder and time limitations, only 25 layers of the sample were simulated. Figure 9.3 shows the temperature distribution result during the deposition of the first layer.

9.4. Result and Analysis

The microstructure observations of 25 layers at several distances from the top surface along the central vertical line of the deposit appear in Figure 9.4. Clearly, all of the microstructures were typical α' martensite. Long, orthogonally oriented martensitic plates are clear in these regions. At the bottom, some indication of basketweave α appears on the right side of the image. However, the major characteristic of the microstructure is long α' plates.



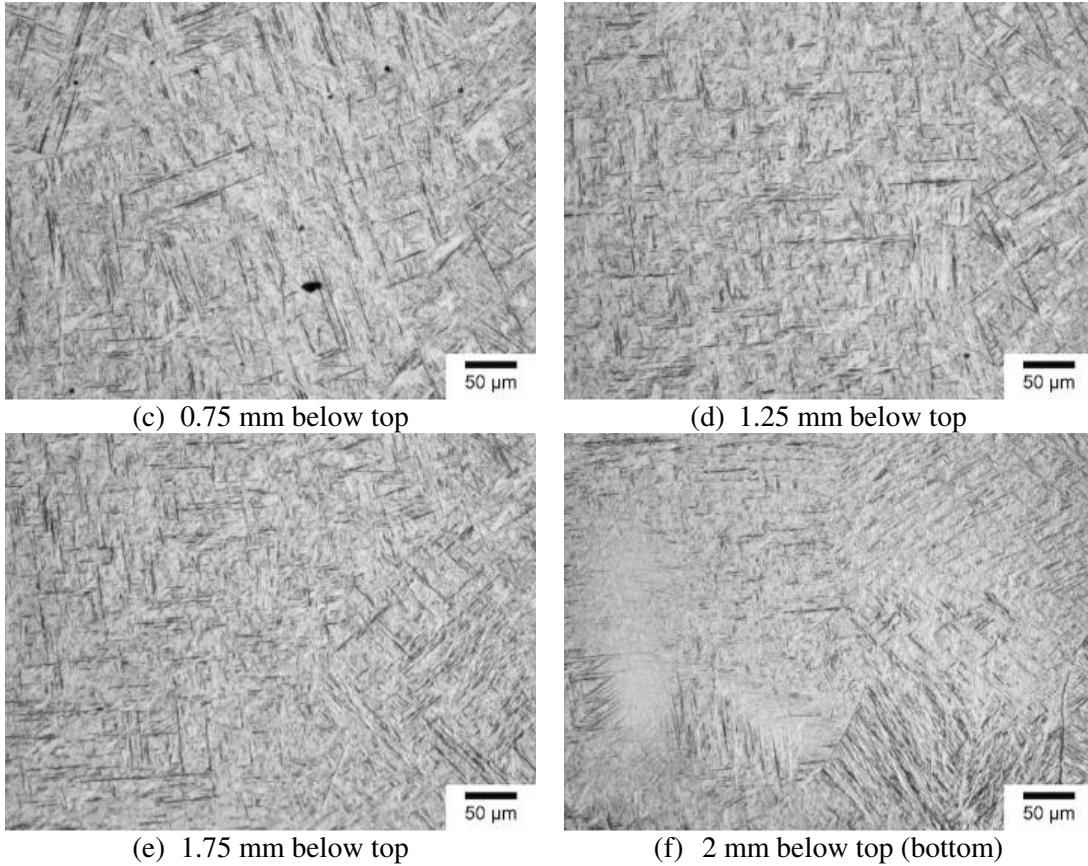


Figure 9.4: Microstructures at different locations of the central vertical line from the top to the bottom of the 25-layer deposit. (a) top; (b) 0.25 mm below top; (c) 0.75 mm below top; (d) 1.25 mm below top; (e) 1.75 mm below top; (f) 2 mm below top (bottom)

The microstructure results of the 60-layer sample appear in Figure 9.5. At the top of the middle cross section, the α' martensite formed inside the prior β grain. At 3 mm from the surface, orthogonal acicular morphology still existed. However, compared with the martensite in the top area, the acicular lath was thicker, and long plates broke into smaller ones. The morphology changed at 4.2 mm from the surface (Figure 9.5c). Two areas having different microstructures can be discerned. Area A was still α' martensite, while Area B consisted of basketweave α laths, and no α' orthogonal grid feature appeared. At the bottom of the deposit, the morphology was typical basketweave α .

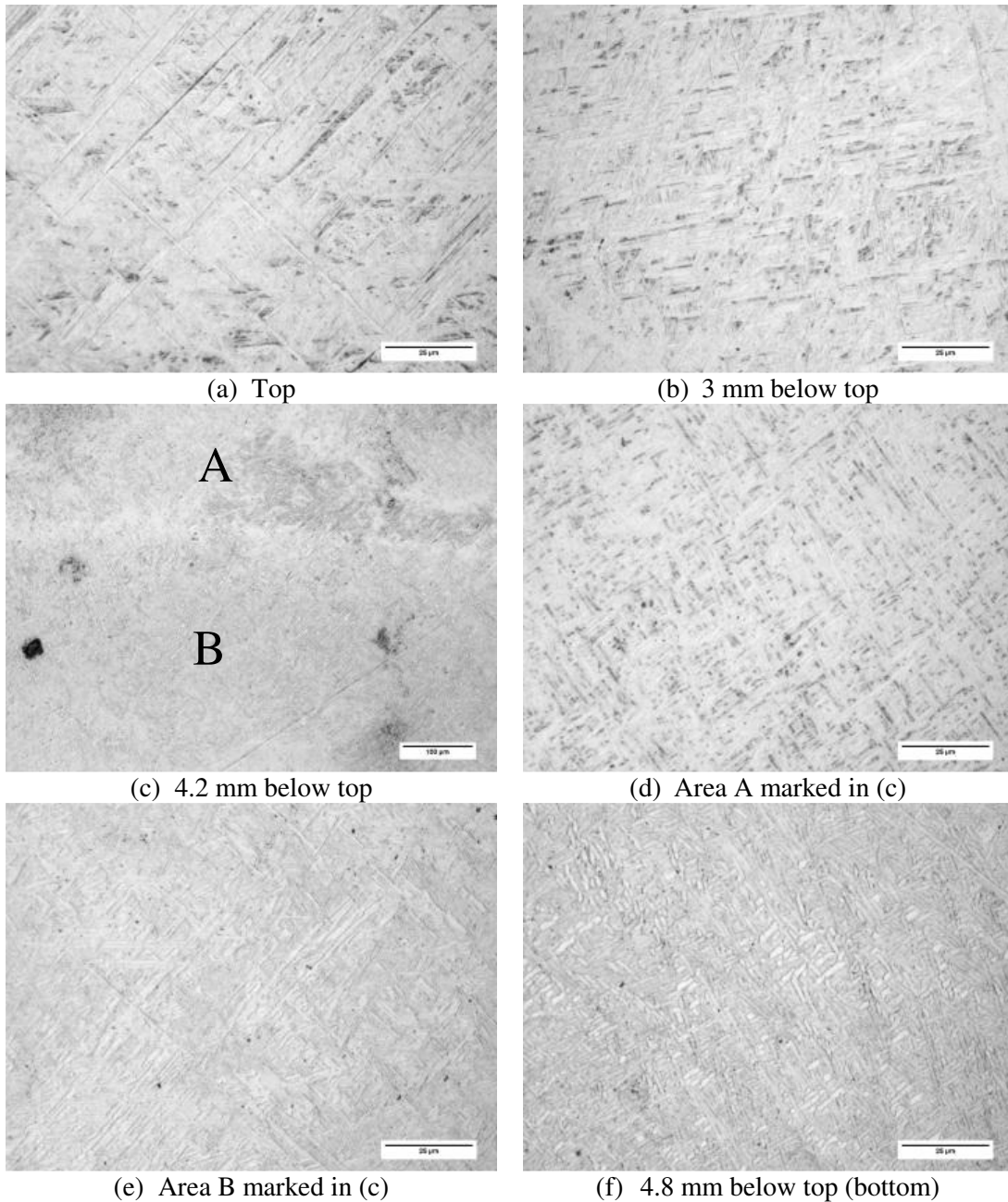


Figure 9.5: Microstructures at different locations of the central vertical line from the top surface of the 60-layer deposit. (a) top; (b) 3 mm below top; (c) 4.2 mm below top; (d) area A marked in (c); (e) area B marked in (c); (f) 4.8 mm below top (bottom)

The simulated temperature history of the top and bottom locations in the 25-layer deposit appears in Figure 9.6. The cooling rates at the β transus temperature of Ti6Al4V (1243 K [31]) are also indicated in the figure. The temperature of the top region during the last scan approximately reached the boiling point. The bottom region also heated to above the β transus during every laser layer scan. Therefore, the α/β microstructure at the bottom region formed during the last laser scan.

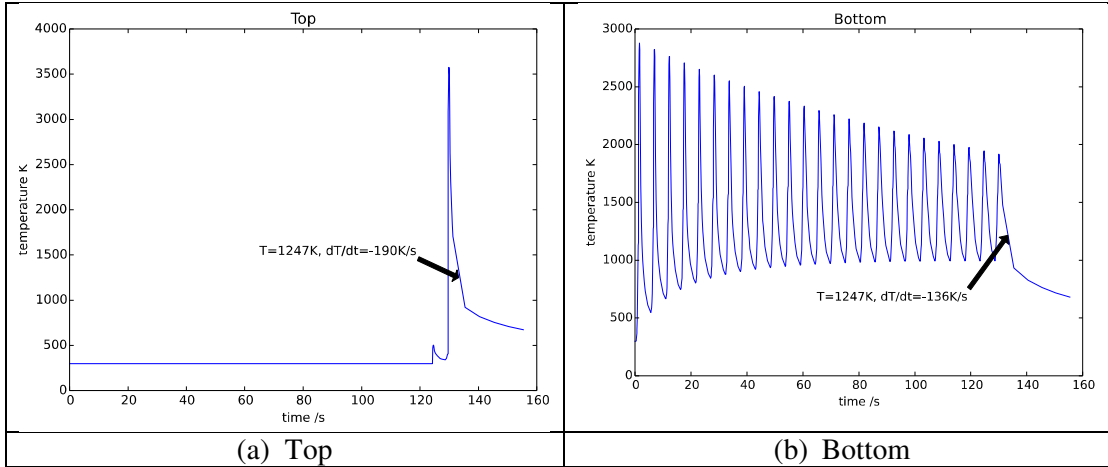


Figure 9.6: Temperature history at top and bottom locations of 25 layers simulated deposition result. Cooling rate β -transus point (1243K) is indicated.

The cooling rate from the β phase region to the α region determines the formed α morphology [32]. Some studies have concluded that cooling rates greater than 18 or 20 K/s lead to the development of α' martensite [33] [34]. For the 25-layer sample, the cooling rate distribution along the central vertical line appears in Figure 9.7. Every position in the center may experience several reheating and cooling processes and the cooling rate mentioned here refers to the last time that determines the formed microstructure. Cooling rate increases from the bottom to top region. This is due to although the cooling rate at bottom region at the first time maybe very large, when cooling from T_{β} at the last time temperature is much more evenly distributed due to thermal diffusion. The cooling rate results and 20 K/s criteria verify that α' martensite dominated the microstructure of the 25-layer sample, as depicted in Figure 9.4.

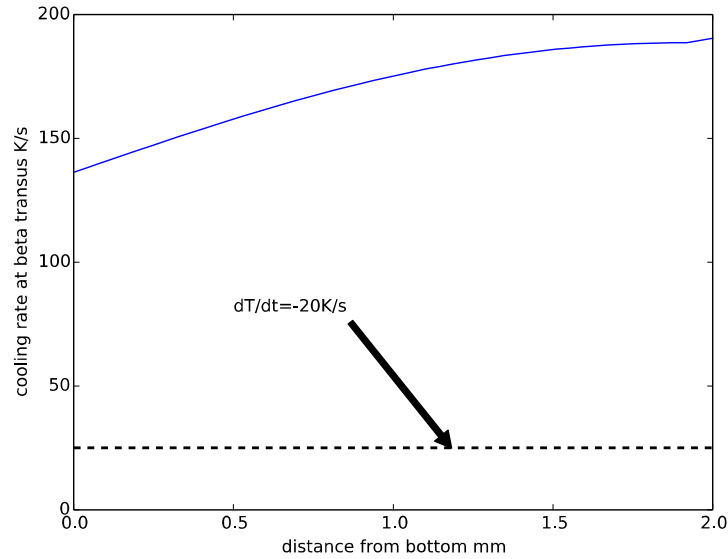


Figure 9.7: Cooling rate at 1243 K distribution along the central vertical line of 25 layers simulated deposition result.

9.5. Conclusion

The nature of the α/β transformation in Ti alloys and the complex thermal history from the laser deposition process cause some special morphology and microstructure features to appear in the deposits. The microstructures of 25- and 60-layer samples exhibited different distributions. The former featured α' martensite, whereas the latter transitioned from α' martensite to basketweave α . While the cooling rate of the 25-layer deposit at 1243 K conformed to results published in the literature, the transition cooling rate could be determined only if the temperature simulation of the 60-layer sample was available.

Further experiments and simulations on larger deposits need to be conducted to reveal different microstructures of Ti6Al4V in the laser metal deposition process.

10. Incorporation of Infrared Camera to Monitor Laser Metal Deposition Process

10.1. Introduction

A FLIR A615 camera, an industrial automation infrared (IR) camera with sensitivity in the range of 7.5-13 microns, was used to perform the following studies. The capabilities of the camera are listed in Table 10.1.

Table 10.1 Specifications of the IR camera

Feature	Specification
<i>Spatial resolution</i>	0.69 mrad
<i>Focal length</i>	25.4 mm
<i>F-number</i>	1
<i>Imaging frequency</i>	12.5 Hz to 200 Hz
<i>Image resolution</i>	640x480, windowing at high freq.
<i>Temperature measured</i>	3 ranges, -50 C to 2000 C (e=1)
<i>Detector</i>	Uncooled bolometer
<i>Detector time constant</i>	8 ms (typical)
<i>Spectrum sensitive to</i>	7.5 to 13 microns

Initial efforts focused on realizing the setup requirements and possible calibration steps to use the IR camera as a process monitoring tool. Later, the camera was used to see the temperature trends during deposition and the size of the mushy zone while using the LAMP lab's feedback. System and acquired data were processed to identify the melt pool or the mushy zone and solidus regions in the deposit.

10.2. Setup and Calibration

An IR camera measures the radiative power of a hot body. This power is later converted into a temperature using lookup tables; hence, meeting the established parameters is crucial for acquiring accurate temperature readings. The laser metal deposition process is very dynamic, and several possibilities can result in significant and irregular changes in the input parameters required for the temperature conversion. The most pertinent of these parameters is emissivity; for accurate measurement, the spectral and thermal dependencies of the emissivity must be identified and accounted for. For the initial set of experiments, the thermal and spectral dependencies were assumed to be negligible.

The camera performs only gray body measurements, meaning the acquired data can be processed with a single emissivity (unless a pixel-by-pixel emissivity map is provided). The associated literature states that the emissivity of metal oxide is higher than the respective metal, and emissive properties are favored by higher temperatures. Therefore, to rationalize the assumption of emissivity's temperature independence, the acquisition was performed in an open atmosphere that resulted in significant surface oxidation (considering the oxide's emissivity at room temperature was approximately 0.9).

10.3. Experimentation and Results

The deposition of stainless steel 316 was monitored using the IR camera. The energy management system was tested and monitored to determine its effect. The emissivity was set to 0.95, as arrived at by averaging the emissivity values of the oxides of constituent elements. A capture rate of 200 fps was set for thermal history acquisition, and other parameters, such as the atmospheric temperature, humidity, atmospheric reflective temperature, and atmospheric transmission, were set as measured.

10.3.1. Energy Management System

The energy management system (EMS) manages the amount of energy according to a certain set signature, i.e., it is set to monitor the radiation and maintain the energy below a set point by

modulating the laser power. The experiment was performed for three different set points, and the power logs in Figure 10.1 and Figure 10.2 illustrate the effect of each set point.

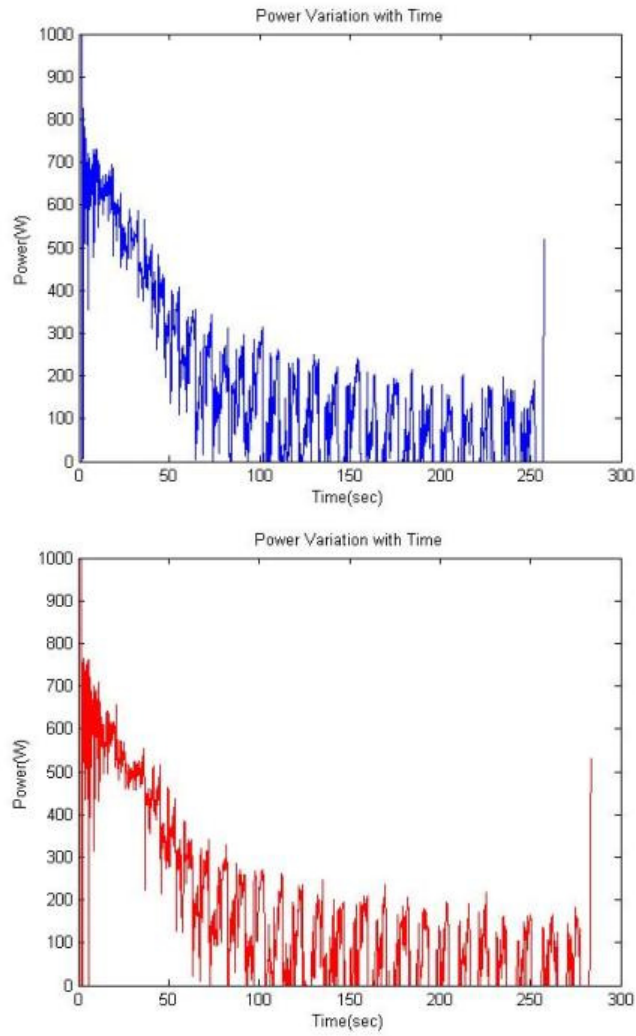


Figure 10.1 Power logs for set points 1 and 2

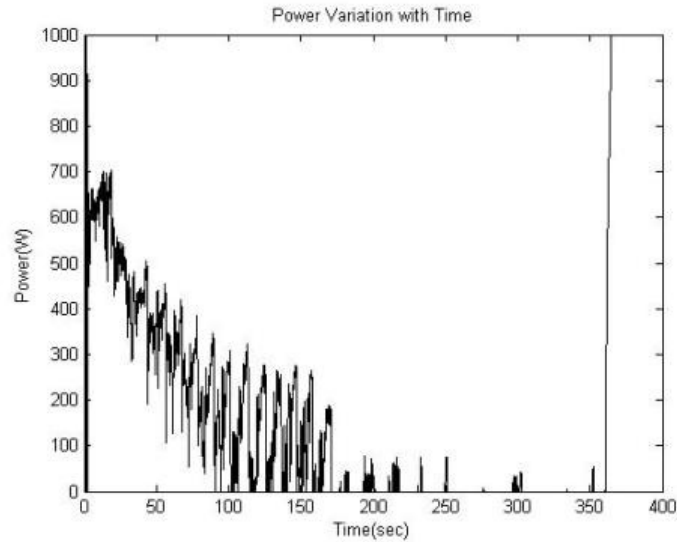


Figure 10.2 Power log for set point 3

The cutoff increased in value from set point 1 through 3, i.e., the allowance for the amount of energy contained in the deposit at a particular instance increased. The power modulation tended to undergo an exponential decay of sorts as the deposition progressed.

10.3.2. High-Temperature Region

The minimum cutoff temperature for this region was set as the solidus temperature of SS 304. The assumptions imposed during parameter selection create an unknown amount of error in the temperature readings acquired. Nonetheless, this experiment was instrumental in identifying the size trends of this high-temperature region during deposition.

10.3.3. Deposition Visualization

Using the iron color palette, a false color image was used to visualize the temperature data. The region above the minimum cutoff temperature also was visualized through the deposition.

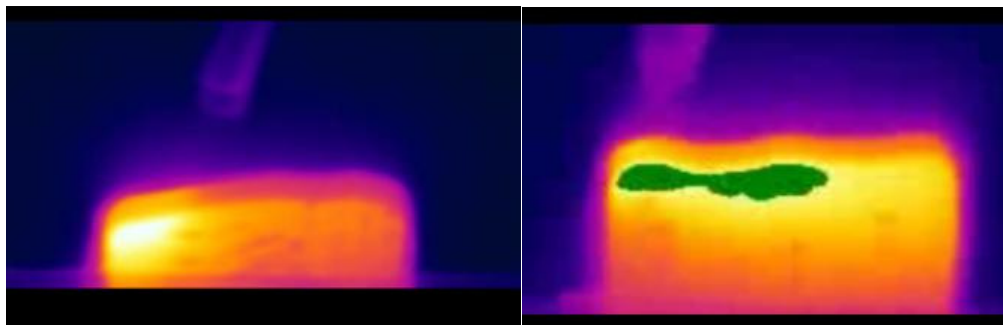


Figure 10.3 False color images used to visualize the deposition and highlight the high-temperature region at an instance during deposition

For each of the noted set points, the average powder feed rate was changed, and the size trends of the high-temperature region were plotted as the deposition progressed. Figure 10.4 illustrates these trends.

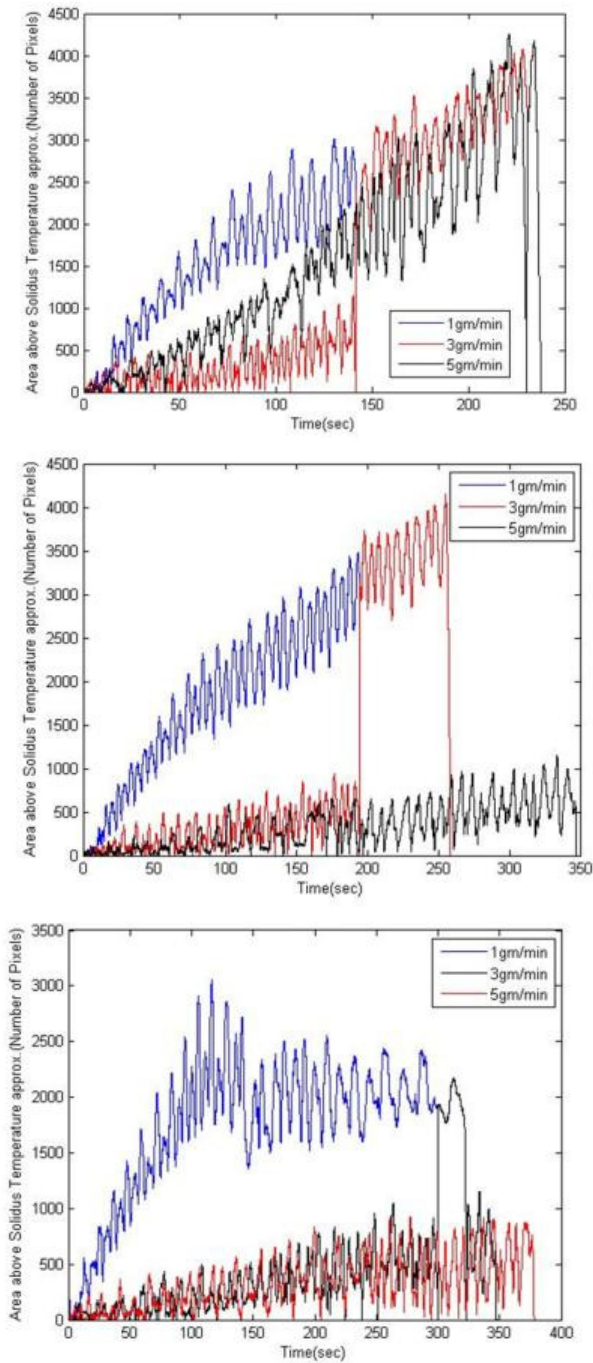


Figure 10.4 Size trends of the high-temperature region through deposition for variable powder feed rates and set points

The optimum solution for ensuring homogeneity throughout the deposition process would be one that saturates the size of the high-temperature region. The current experiment, through trial and error, was able to successfully realize such saturation, thereby identifying the possible optimum setup for homogenous deposition. Though not a smooth saturation, the size of the high-temperature region stabilized around a certain range for a set of parameters.

10.4. Image Processing

The associated literature [35] states that a drop in emissivity occurs when a metal undergoes phase transformation, i.e., when solid is melted into liquid, the emissivity decreases. As the IR camera reads the radiative power, it senses a decrease in the temperature when such a transformation occurs (as the temperature is analyzed using a single emissivity value). The band radiance pertinent to the camera is listed in Table 10.2.

Table 10.2 Band radiance pertinent to the camera

SS 316		
Temperature	Emissivity[36]	Band radiance (7.5 to 13 micron)
Liquidus, 1400 C	0.3	4745 W/sq.m/sr
Solidus, 1377 C (oxidized)	0.9	1582 W/sq.m/sr

This proves that the melt pool appears colder than it actually is. Exploiting this phenomenon, edge detection techniques were chosen to identify the melt pool or the mushy zone in the thermographs. The change in emissivity is illustrated in Figure 10.5.

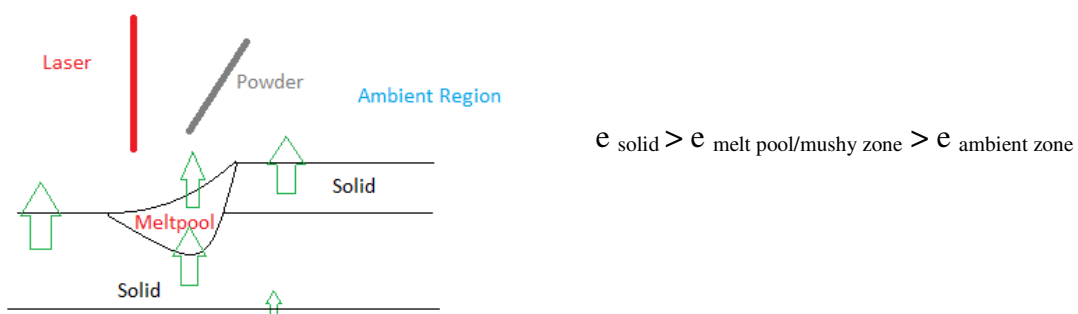


Figure 10.5 Boundaries and emissivity change trend during deposition

10.4.1. Laplace Edge Detection

The Laplace edge detection technique was chosen to identify the transitions in the deposit.

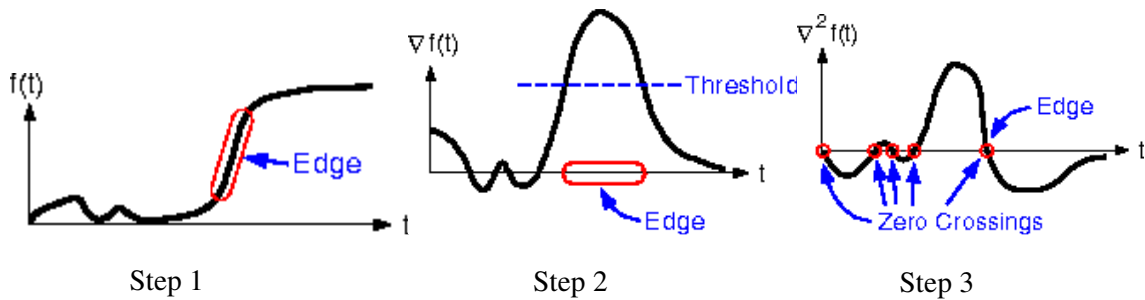


Figure 10.6 Steps in Laplace edge detection [37]

The Laplace edge detection technique targets the change in intensity of the signal and identifies the point of transition using the zero crossing points from the second-degree derivative of the signal. The points of interest or the edges are identified using a threshold variance as the decision criterion in step 3 (from Figure 10.6) [38].

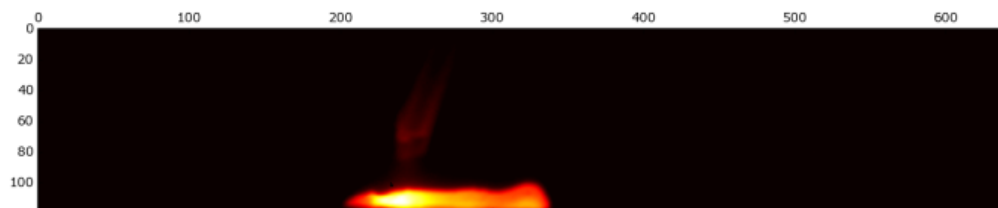
10.4.2. Methodology

Steps involved in image processing:

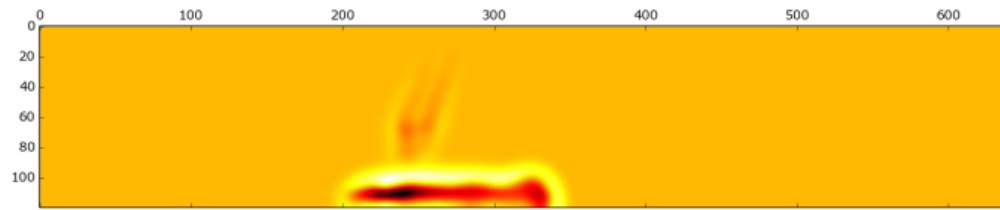
- 1) Moving median
- 2) Gaussian blur
- 3) Laplacian transform
- 4) Find zero crossings
- 5) Clarify image
- 6) Detect edges
- 7) Identify and process region around melt pool
- 8) Mark melt pool and solidus region

These steps were followed to remove noise, smooth, identify edges, clarify the image, and mark the region of interest.

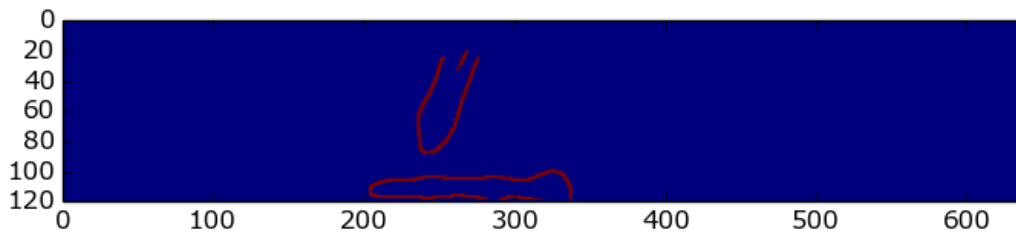
The outcomes of implementing these steps appear in Figure 10.7.



(a) Moving median



(b) Laplacian of Gaussian



(c) Edges found

Figure 10.7 Initial image processing steps

The edges found, as shown in Figure 10.7, do not include the melt pool because the variation from solid to liquid was insignificant compared to the variation from the deposit to ambience. In order to identify the melt pool, a more local search had to be performed within the deposit. After further image clarification and edge detection, the final outcome was arrived at, as depicted in Figure 10.8.

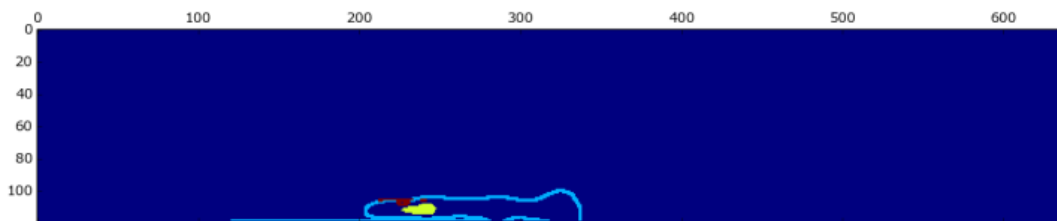


Figure 10.8 Deposit (sky blue), solidus region (yellow), and mushy zone (red)

10.5. Conclusions

An infrared camera was incorporated as a process monitoring tool to identify the solidus and mushy zones during deposition. The images were successfully processed to identify these regions.

10.6. Future work

The relationship between the temperatures in the regions of interest needs to be established, and further emphasis must be placed on decoding the constituents of the mushy zone. These explorative efforts need to be employed during deposition to identify various phenomena during solidification.

11. Related Works

11.1. Related Publications:

1. Fan, Zhiqiang and Frank Liou, "Numerical Modeling of the Additive Manufacturing (AM) Processes of Titanium Alloy," *Titanium Alloys - Towards Achieving Enhanced Properties for Diversified Applications*, ISBN 978-953-51-0354-7, Chapter 1, pp. 1-28, Editor: A.K.M. Nurul Amin, InTech, March, 2012.
2. Amogh Shenoy and Frank Liou, "Microwire Feeder for Laser Applications," *Biomedical Engineering Research (BER)*, DOI:10.5963/BER0202006, pp.96-107, 2013.
3. Chen, Xueyang, and Frank Liou, and J. W. Newkirk, "Numerical Simulation of Dilution in Laser Metal Deposition by Powder Injection," 41st Annual North American Manufacturing Research Conference (NAMRC 41), June 10-14, 2013, Madison, WI, paper number NAMRC41-1623.
4. Heng Liu, Todd E. Sparks, Frank Liou, David M. Dietrich, "Numerical Analysis of Thermal Stress and Deflection in Multi-Layer Laser Metal Deposition Processes," *Proceedings of the 24th Solid Freeform Fabrication Symposium*, Austin, Texas, August 12-14, 2013.
5. Jingwei Zhang, Frank Liou, William Seufzer, Joseph Newkirk, Zhiqiang Fan, Todd E. Sparks, Heng Liu, "Probabilistic Simulation of Solidification Microstructure Evolution During Laser-Based Metal Deposition," *Proceedings of the 24th Solid Freeform Fabrication Symposium*, Austin, Texas, August 12-14, 2013.
6. Sreekar Karnati, Todd E. Sparks, Frank Liou, Niroop Matta, "Vision-based Process Monitoring for Laser Metal Deposition Processes," *Proceedings of the 24th Solid Freeform Fabrication Symposium*, Austin, Texas, August 12-14, 2013.
7. Sujitkumar Dongare, Todd E. Sparks, Joseph Newkirk and Frank Liou, "A Mechanical Testing Methodology for Additive Manufacturing Processes," *Proceedings of the 25th Solid Freeform Fabrication Symposium*, Austin, Texas, August 4-6, 2014.
8. Sreekar Karnati, Todd E Sparks, Frank Liou, "Thermo-graphic investigation of laser metal deposition," *25th Solid Freeform Fabrication Symposium*, Austin, Texas, August 4-6, 2014.

11.2. Related Presentations:

- Liou, F, "What are the key measurement science barriers that prevent innovation in metal-based AM?" Workshop on Measurement and Standards for Metals-based Additive Manufacturing December 4-5, 2012 at National Institute of Standards and Technology, Gaithersburg Campus, Gaithersburg, MD.
- Joseph Newkirk; Frank Liou; Karen Taminger; William Seufzer; Zhiqiang Fan; Harihar Sistla; Sreekar Karnati, "Modeling and Experimental Study of Advanced Materials for Aerospace," *Materials Science & Technology 2013*, October 27-31, 2013: Montreal, QC.

- Liou, F., "Advanced Additive Materials Modeling and Simulation - Multiscale and Multiphysics Modeling of Metal Deposition Processes," Additive Aerospace Summit 2013, Los Angeles, CA, October 16 - 18, 2013.
- Liou, F., Fan, Z., Newkirk, J., Seufzer, W. and Taminger, K., "Modeling and its Applications to Metal Additive Manufacturing Processes," AeroMat 2013, Bellevue, WA, April 1 - 4, 2013.
- Liou, Frank, Joseph Newkirk, William Seufzer and Karen Taminger, "Multi-scale Modeling and Simulation of Directed Energy Deposition Processes," "AeroMat 2014 in Orlando, FL on June 16-19, 2014.

11.3. To be Published/Presented:

- Jingwei Zhang, Frank Liou, Joseph Newkirk, William Seufzer, Karen Taminger, "Solidification Microstructure Modeling During Laser-Based Metal Deposition".
- Yunlu Zhang, Frank Liou, Joseph Newkirk, William Seufzer, Karen Taminger, "Solid State Transformation of Microstructure Modeling During Laser-Based Metal Deposition".
- Kannan Suresh, Shankar Reddy Pakkuru, Frank Liou, Joe Newkirk, William Seufzer, Karen Taminger, "Accelerated Computing for 3D Modeling of Direct Metal Deposition Processes".
- Liou, F., "Process Modeling and Qualification of Metal Additive Manufacturing," Additive Aerospace Summit 2014, Los Angeles, CA, November 3-6, 2014.

11.4. Related Theses and Dissertations:

- Fan, Zhiqiang, Numerical modeling of heat transfer and fluid flow in laser metal deposition by powder injection, Ph.D. dissertation, Missouri University of Science and Technology, 2013.
- Rodney Clayton, The use of elemental powder mixes in laser-based additive manufacturing, MS thesis, Missouri University of Science and Technology, 2013.
- Chen, Xueyang, Modelling of directed energy deposition processes, MS thesis, Missouri University of Science and Technology, 2014.
- Liu, Heng, Numerical analysis of thermal stress and deformation in multi-layer laser metal deposition process, MS thesis, Missouri University of Science and Technology, 2014.
- Sreekar Karnati, Thermo-graphic investigation of laser metal deposition (tentative), MS thesis, Missouri University of Science and Technology, 2014 (expected).

11.5. News Articles:

<http://www.sciencedaily.com/releases/2013/09/130917153717.htm>
http://3dprintinginsider.com/researchers-looking-to-make-3d-materials-stronger_b9891
<http://www.designfax.net/cms/dfx/opens/article-view-dfx.php?nid=4&bid=280&et=mechanical&pn=01>
<http://news.mst.edu/2013/12/13-important-research-stories-from-2013/>

12. References

-
- ^[1]D. Gueyffier, J. Li, A. Nadim, R. Scardovelli and S. Zaleski (1999), Volume of Fluid interface tracking with smoothed surface stress methods for three-dimensional flows. *Journal of Computational Physics*, Vol. 152, No. 2, (July 1999), pp. 423-456, ISSN 0021-9991.
- ^[2]R. Scardovelli and S. Zaleski (2000), Analytical relations connecting linear interfaces and volume fractions in rectangular grids, *Journal of Computational Physics*, Vol. 164, No. 1, (October 2000), pp. 228-237, ISSN 0021-9991.
- ^[3]R. Scardovelli and S. Zaleski (2003), Interface reconstruction with least-square fit and split Eulerian-Lagrangian advection. *International Journal for Numerical Methods in Fluids*, Vol. 41, No. 3, (January 2003), pp. 251-274, ISSN 0271-2091.
- ^[4]C.W. Hirt and B.D. Nichols (1981), Volume-of-fluid (VOF) for the dynamics of free boundaries. *Journal of Computational Physics*, Vol. 39, No. 1, (January 1981), pp. 201-225, ISSN 0021-9991.
- ^[5]A.J. Chorin (1980), Flame advection and propagation algorithms. *Journal of Computational Physics*, Vol. 35, No. 1, (March 1980), pp. 1-11, ISSN 0021-9991.
- ^[6]R. Debar (1974), *Fundamentals of the KRAKEN Code*, Technical Report UCIR-760, Lawrence Livermore National Laboratory, 1974.
- ^[7]W.F. Noh and P.R. Woodward (1976), SLIC (simple line interface calculation). *Lecture Notes in Physics*, Vol. 59, pp. 330-340, ISSN 0075-8450.
- ^[8]R. Scardovelli and S. Zaleski (1999), Direct numerical simulation of free-surface and interfacial flow. *Annual Review of Fluid Mechanics*, Vol. 31, (January 1999), pp. 567-603, ISSN 0066-4189.
- ^[9]J.U. Brackbill, D.B. Kothe and C. Zemach (1992), A continuum method for modeling surface tension. *Journal of Computational Physics*, Vol. 100, No. 2, (June 1992), pp. 335-354, ISSN 0021-9991.
- ^[10]E. Shirani, N. Ashgriz and J. Mostaghimi (2005), Interface pressure calculation based on conservation of momentum for front capturing methods. *Journal of Computational Physics*, Vol. 203, No. 1, (February 2005), pp. 154-175, ISSN 0021-9991.
- ^[11]J. Lin (2000), Laser attenuation of the focused powder streams in coaxial laser cladding. *Journal of Laser Applications*, Vol. 12, No. 1, (February 2000), pp. 28-33.
- ^[12]B. van Leer (1979), Towards the ultimate conservative difference scheme, V. A second order sequel to Godunov's method, *J. Com. Phys.*, Vol. 32, (1979), pp. 101-136.
- ^[13]A.J. Chorin (1968), Numerical solution of the Navier-Stokes equations. *Mathematics of Computation*, Vol. 22, No. 104, (October 1968), pp. 745-762, ISSN 0025-5718.
- ^[14]D. S. Kershaw (1978), The incomplete Cholesky-conjugate gradient method for iterative solution of systems of linear equations. *J Comp Phys* (1978), Vol. 26, pp. 43-65.
- ^[15]D. A. Knoll, D. B. Kothe and B. Lally (1999), A new nonlinear solution method for phase change problems, *Numerical Heat Transfer, Part B Fundamentals*, Vol. 35, No. 4, (December 1999), pp. 436-459, ISSN 1040-7790.
- ^[16]G.S. Collins and H.J. Melosh (August 2002), SALES 2: A multi-material extension to the SALE hydrocode with improved equation of state and constitutive model.

-
- [17] <http://www.mcs.anl.gov/research/projects/mpi/>
- [18] W. Seufzer (2012) "Slicing the Cladding3D code for use with MPI," *An internal document for information sharing*. For more information contact author at bill.seufzer@nasa.gov.
- [19] Solenthaler (2009). Predictive-Corrective Incompressible SPH.
- [20] Akinci (2012). "Versatile Rigid-Fluid Coupling for Incompressible SPH <http://www.nadir.tk/research>". ACM TOG, SIGGRAPH proceedings
- [21] <http://www-2.unipv.it/compmech/seminars/manenti-pres.pdf>
- [22] Bodin (2011). "Constraint Fluids. <http://www.physics.umu.se/english/research/statistical-physics-and-networks/complex-mechanical-systems/fluids-and-solids/>". IEEE Transactions on Visualization and Computer Graphics
- [23] Ch.-A.Gandin and M. Rappaz (1994), A coupled finite element-cellular automaton model for the prediction of dendritic grain structures in solidification. *Acta metall.mater.*, Vol. 42, No. 7, pp. 2233–2246.
- [24] W. Oldfield (1996), A quantitative approach to casting solidification: Freezing of cast iron. *Trans.Am. Soc. Metals*, Vol. 59, p. 945.
- [25] W. Kurz and D.J. Fisher (1992), Fundamentals of solidification. *Trans Tech Publication*, ch. Appendix 7 and 8, pp. 226–246.
- [26] W. Kurz and D.J. Fisher (1992), Fundamentals of solidification. *Trans Tech Publication*, ch. Appendix 9, pp. 247–260.
- [27] X. Wu, J. Liang, J. Mei, C. Mitchell, P.S. Goodwin and W. Voice (2004), Microstructures of laser-deposited Ti–6Al–4V," *Mater. Des.*, Vol. 25, No. 2, pp. 137–144.
- [28] G. Lütjering and J.J.C. Williams (2007), Titanium, Springer.
- [29] J. Da Costa Teixeira, B. Appolaire, E. Aeby-Gautier, S. Denis, and L. Hélicher, (2008), Modeling of the phase transformations in near- β titanium alloys during the cooling after forging. *Comput. Mater. Sci.*, Vol. 42, No. 2, pp. 266–280.
- [30] E. Brandl, A. Schoberth, and C. Leyens (2012), Morphology, microstructure, and hardness of titanium (Ti6Al4V) blocks deposited by wire-feed additive layer manufacturing (ALM). *Mater. Sci. Eng. A*, Vol. 532, No. 0, pp. 295–307.
- [31] R. Dąbrowski (2011), The kinetics of phase transformations during continuous cooling of the Ti6Al4V alloy from the single-phase β range. *Journal of Achievements in Materials and Manufacturing Engineering*, Vol 59, Issue 1, July 2013.
- [32] L. Qian, J. Mei, J. Liang, and X. Wu (2005), Influence of position and laser power on thermal history and microstructure of direct laser fabricated Ti–6Al–4V samples. *Mater. Sci. Technol.*, Vol. 21, No. 5, pp. 597–605.
- [33] T. Ahmed and H.M. Rack (1998), Phase transformations during cooling in $\alpha+\beta$ titanium alloys. *Mater. Sci. Eng. A*, 243(1–2), pp. 206–211.
- [34] J. Sieniawski, W. Ziaja, K. Kubiak and M. Motyka (2013), "Microstructure and mechanical properties of high strength two-phase titanium alloys.
- [35] Data from <http://www.raytek.com/Raytek/enr0/IREducation/EmissivityTableMetals.htm>;

<http://www.monarchserver.com/TableofEmissivity.pdf>;
http://www.sciene.com/pdfs/428_InfraredThermometerEmissivitytablesrev.pdf; as
extracted on 9/20/2014
^[36][http://wwweng.lbl.gov/~dw/projects/DW4229_LHC_detector_analysis/calculations/e
missivity2.pdf](http://wwweng.lbl.gov/~dw/projects/DW4229_LHC_detector_analysis/calculations/emissivity2.pdf)
^[37]<http://www.owl.net.rice.edu/~elec539/Projects97/morphjrks/laplacian.html>
^[38]As extracted from
<http://www.owl.net.rice.edu/~elec539/Projects97/morphjrks/laplacian.html>; on 9/20/14

REPORT DOCUMENTATION PAGE

*Form Approved
OMB No. 0704-0188*

The public reporting burden for this collection of information is estimated to average 1 hour per response, including the time for reviewing instructions, searching existing data sources, gathering and maintaining the data needed, and completing and reviewing the collection of information. Send comments regarding this burden estimate or any other aspect of this collection of information, including suggestions for reducing this burden, to Department of Defense, Washington Headquarters Services, Directorate for Information Operations and Reports (0704-0188), 1215 Jefferson Davis Highway, Suite 1204, Arlington, VA 22202-4302. Respondents should be aware that notwithstanding any other provision of law, no person shall be subject to any penalty for failing to comply with a collection of information if it does not display a currently valid OMB control number.
PLEASE DO NOT RETURN YOUR FORM TO THE ABOVE ADDRESS.

1. REPORT DATE (DD-MM-YYYY) 01-02-2015		2. REPORT TYPE Contractor Report		3. DATES COVERED (From - To) June 2011 - August 2014	
4. TITLE AND SUBTITLE Multiscale and Multiphysics Modeling of Additive Manufacturing of Advanced Materials				5a. CONTRACT NUMBER	
				5b. GRANT NUMBER	
				5c. PROGRAM ELEMENT NUMBER	
6. AUTHOR(S) Liou, Frank; Newkirk; Fan, Zhiqiang; Sparks, Todd; Chen, Xueyang; Fletcher, Kenneth; Zhang, Jingwei; Zhang, Yunlu; Kumar, Kannan Suresh; Karnati, Sreekar				5d. PROJECT NUMBER	
				5e. TASK NUMBER NNX11AI73A	
				5f. WORK UNIT NUMBER 081876.02.07.50.01.01	
7. PERFORMING ORGANIZATION NAME(S) AND ADDRESS(ES) NASA Langley Research Center Hampton, Virginia 23681				8. PERFORMING ORGANIZATION REPORT NUMBER	
9. SPONSORING/MONITORING AGENCY NAME(S) AND ADDRESS(ES) National Aeronautics and Space Administration Washington, DC 20546-0001				10. SPONSOR/MONITOR'S ACRONYM(S) NASA	
				11. SPONSOR/MONITOR'S REPORT NUMBER(S) NASA/CR-2015-218691	
12. DISTRIBUTION/AVAILABILITY STATEMENT Unclassified - Unlimited Subject Category 26 Availability: NASA STI Program (757) 864-9658					
13. SUPPLEMENTARY NOTES Final Report Langley Technical Monitor: William J. Seufzer					
14. ABSTRACT The objective of this proposed project is to research and develop a prediction tool for advanced additive manufacturing (AAM) processes for advanced materials and develop experimental methods to provide fundamental properties and establish validation data. Aircraft structures and engines demand materials that are stronger, useable at much higher temperatures, provide less acoustic transmission, and enable more aeroelastic tailoring than those currently used. Significant improvements in properties can only be achieved by processing the materials under nonequilibrium conditions, such as AAM processes. AAM processes encompass a class of processes that use a focused heat source to create a melt pool on a substrate. Examples include Electron Beam Freeform Fabrication and Direct Metal Deposition. These types of additive processes enable fabrication of parts directly from CAD drawings. To achieve the desired material properties and geometries of the final structure, assessing the impact of process parameters and predicting optimized conditions with numerical modeling as an effective prediction tool is necessary. The targets for the processing are multiple and at different spatial scales, and the physical phenomena associated occur in multiphysics and multiscale.					
15. SUBJECT TERMS Additive; Electron beams; Heat sources; Manufacturing; Physical factors; Sound transmission					
16. SECURITY CLASSIFICATION OF:			17. LIMITATION OF ABSTRACT	18. NUMBER OF PAGES	19a. NAME OF RESPONSIBLE PERSON
a. REPORT	b. ABSTRACT	c. THIS PAGE			STI Help Desk (email: help@sti.nasa.gov)
U	U	U	UU	85	19b. TELEPHONE NUMBER (Include area code) (757) 864-9658